Analysis and Evaluation of Electromagnetic Losses in Induction Machines and their Impact on Motor Design and Performance

A

Thesis Submitted

in Partial Fulfilment of the Requirements

for the Degree of

DOCTOR OF PHILOSOPHY

By

Rajendra Kumar

Department of Electronics and Electrical Engineering

Indian Institute of Technology Guwahati

Guwahati - 781039, INDIA.

October, 2021

To

My supervisor

Prof. Praveen Kumar

for his guidance and inspiration

&

To

My dear **parents** *and,* **Shri NC Suthar**,

my wife **Pooja**, *son* **Vihaan** *and, daughter* **Gaurshi**,

my siblings **Umesh** *and,* **Kuldeep** *for their love and support.*

Certificate

This is to certify that the thesis entitled "**Analysis and Evaluation of Electromagnetic Losses in Induction Machines and their Impact on Motor Design and Performance**", submitted by **Rajendra Kumar** (156102029), a research scholar in the *Department of Electronics & Electrical Engineering, Indian Institute of Technology Guwahati*, for the award of the degree of **Doctor of Philosophy**, has been carried out by him under my supervision and guidance. The thesis has fulfilled all requirements as per the regulations of the institute and in my opinion has reached the standard needed for submission. The results embodied in this thesis have not been submitted to any other University or Institute for the award of any degree or diploma.

Dated:

Guwahati.

Prof. Praveen Kumar
Dept. of Electronics and Electrical Engg.
Indian Institute of Technology Guwahati
Guwahati - 781039, Assam, India.

Acknowledgements

I would here like to take the opportunity to extend my thankfulness to all whose cooperation led me to this achievement.

Foremost, I want to express my sincere gratitude to my research supervisor Prof. Praveen Kumar. His generosity, encouragement and, meticulous attention to detail throughout all these years have been an enormous source of inspiration for me. He possessesmy deepest gratitude for hisunwavering support and patience. I sincerely appreciate the time and effort heput into studying each document I submitted and providing the prolific suggestions.

Furthermore, I would like to extend my gratitude towards my doctoral committee members Prof. Rohit Sinha, Prof. Sisir Kumar Nayak and Dr. Ravindranath Adda, for sparing their precious time to assess the progress of my work and their valuable remarks.

I am also grateful to the faculty members and the office staff of the Department of Electronics and Electrical Engineering, IIT Guwahati, for their readiness to extend their helping hands following the culture of integrity and best practices of IIT Guwahati.

I thank Mr. Dimpul and Mr. Bharali for providing the necessary lab facilities required for the research work.

My cordial thanks go to Bikash Sah for providing all his assistance and critical feedback while carrying out this work. I had immense pleasure spending great time with especially, Ankit Dalal, Rakesh Roy, Kashyap Kumar Prabhakar, Upendra Reddy, Brijesh Kumar Kushwaha, Gautam Rituraj, Umesh Kumar, Binita Nanda, Tarique Sayed and, Ankit Vishway. They were there for me at my lowest moments. Their ungrudging help and encouragement gave me immense strength.

Finally, I want to express my heartfelt gratitude to all of my family members, whose love, sacrifice, and unwavering support remained the most essential in my decision to pursue this career path.

(Rajendra Kumar)

Abstract

In this thesis, various electromagnetic losses, *viz*. core losses and stray losses of an induction machine have been studied and characterized for their fast and accurate representation in the iterative motor design process. To accomplish this, the first part of the work uses the measurement results of various medium power three-phase induction motors ranging from 1kW to 375kW output power. The factors affecting the stray losses and the magnetic circuit parameters of a motor are then investigated for all these motors to develop various empirical correlations of stray loss.

The operating slip of the motor represents its loading quotient and, the ratio of fundamental to the carrier governs the time-harmonics in the load current. Loading of the motor and harmonics present in the power supply source are also affect the loss distribution. The work attempts to formulate this by testing the induction motors at combinations of different shaft-torques and fundamental to carrier frequency ratios. Along with this, the impact of slot geometry on these magnetic losses, in support of the proposed model's capability, is demonstrated by designing the motors of the same efficiency class but different fractions of stray losses.

The comparison of various existing state-of-the-art existing loss models with the proposed model reveals that, apart from exhibiting the highest closeness to the measurement results, the proposed model is usable for the already existing motor and the design phase. Moreover, the model can determine the SL in case motors have the same output power but different geometric design, which other existing models can not.

Moreover, the work presents a straightforward approach to core loss estimation in its final part, wherein a more precise and realistic evaluation of eddy current loss is proposed. This approach considers the variation in lamination thickness and the impact of phase angles of

induction's harmonics to figure out the area of the hysteresis loop. The approach makes the core loss evaluation very fast by making the experimental requirements minimum.

Index Terms: Induction motors, Energy efficiency, Motor design, Stray losses, Eddy current loss, hysteresis loss, Inverter power supply.

Contents

List of Figures

List of Tables

Nomenclature

Abbreviations

EMDS	Electric Motor Driven Systems.
MEPS	Minimum Energy Performance Standards.
NEMA	National Electric Manufacturers Association.
IE3	International Efficiency Standard.
IEC	International Electrotechnical Commission.
SL	Stray Loss.
JEC	Japanese Electrotechnical Committee.
FEM	Finite Element Methods.
IMs	Induction Machines.
1-D	One Dimensional.
2-D	Two Dimensional.
3-D	Three Dimensional.
CL	Core Loss.
SBM	Superposition Based Methods.
NSBM	Non-Superposition Based Methods.
ECB	Eddy Current Brake.
MDS	Motor-Driven Systems.
MMF	Magnetomotive Force.
ECPS	Electrical Circuit Parameters.
AIC	Akaike Information Criterion.
BIC	Bayesian Information Criterion.

FF	Fill-Factor.
SD	Stator Dimension.
RD	Rotor Dimensions.
NL	NO Load.
NLBR	No-Load and Blocked Rotor.
THD	Total Harmonic Distortion.
SE	Steinmetz Equation.
CTTM	Classical Two-Term Model.
SBM	Superposition Based CL Models.
NSBM	Non-Superposition Based CL Models.
DWM	Domain Wall Movement.
CF	Curve-Fitting.
RT	Rotation Of H-Vector

List of Publications

Journal Publications

1. **R. Kumar**, P. Kumar, T. Kanekawa and K. Oishi, "Stray Loss Model for Induction Motors With Using Equivalent Circuit Parameters," in IEEE Transactions on Energy Conversion, vol. 35, no. 2, pp. 1036-1045, June 2020, doi: 10.1109/TEC.2020.2964616.
2. **R. Kumar** and P. Kumar, "Core Loss Estimation for an Inverter-fed Induction Motor With More Accurate Realisation of Material Non-linearity and Impact of Hysteresis Minor Loops," in IEEE Transactions on Energy Conversion, doi: 10.1109/TEC.2021.3085764.

Other submitted

1. **R. Kumar**, P. Kumar, T. Kanekawa and K. Oishi, "Eddy Currents Based Stray Loss Model For Variable Load Conditions of Medium Power Induction Motors," in IEEE Transactions on Magnetics.
2. **R. Kumar**, B. Sah, P. Kumar, "Stray loss Formulation for Inverter Driven Induction Motors for a Wide Range of Switching Frequency and Motors Loading," in IEEE Journal of Emerging and Selected Topics in Power Electronics.

Conference Publications

1. **R. Kumar** and P. Kumar, "Modelling of Stray-Load Loss for Medium Power Induction Motors," IECON 2018 - 44th Annual Conference of the IEEE Industrial Electronics Society, Washington,DC, 2018, pp. 571-576, doi: 10.1109/IECON.2018.8591650.

1

Introduction

Contents

1.1 Research background

With utilising 53% of the total electrical energy generated worldwide, electric motor driven systems (EMDS) form the largest energy consumption sector [1]. Within the EMDS sector, 77% of the net energy consumption pertains to the medium-sized motors of power rating below 375 kW [2] in which, more than 80% of motors are induction motors. Ease of construction, minimal maintenance, and low cost are the salient features of prima facie, which make IM a convenient choice in EMDS. This widespread use of IMs makes them a worthwhile candidate for energy efficiency concerns and improvement measures. With an average efficiency of 84%, total annual energy consumption and emissions estimates corresponding to these medium-sized IM are 10500 TWh and 6800 million metric tons of CO_2, respectively [2]. A recent forecast released by the UN-Environment (a global environmental authority) shows [3] that the use of energy-efficient electric motors can reduce yearly CO_2 emission by 230 million metric tons and result in an annual energy saving of 300 TWh by 2030.

With a growing emphasis on energy security and environmental safety, countries worldwide are moving towards more stringent energy standards by upgrading their minimum energy performance standards (MEPS). The USA, Japan, and the European Union have set motor MEPS levels at IE3 (the equivalent of National Electric Manufacturers Association (NEMA) premium efficiency) in 2015 and 2017, respectively [4]. In China and India, IE2 (NEMA high-efficiency) motors have been mandatory since 2011 and 2017, respectively [5]. The move towards high-efficiency motors has initiated a rigorous research and development worldwide in the field of motor design, both in academia and industry [6], [7].

The design of a high-efficiency motor requires accurate estimation of losses. Typically, there are five significant losses in a motor viz. stator copper losses, rotor copper losses, core loss, friction-windage losses, and stray losses. Among these five losses, core losses and stray losses are critical to estimate accurately, especially at the motor's design phase. These two losses share 35% to 60% of the total motor losses (depending upon the motor's power rating and efficiency class), which is significant to affect the efficiency evaluation or enhancement method. The core

and stray losses depend upon the time and space distribution of the magnetic flux density in the various motor segments. If the motor derives power from a PWM inverter, these losses get augmented and become more complex to evaluate due to higher-order harmonics.

1.2 Literature review

Efficiency always remains of prime importance in both the control and design stages of a motor. For an already installed motor, the high-efficiency operation is ensured with the optimal air gap flux-based control technique, which reduces motor losses. Similarly, at the design stage, the motor geometry is optimised for minimal losses. However, the design of a motor is an iterative process which, involves several design variants depending upon the manufacturing constraints. The qualitative analysis of all these variants requires all their losses estimates. Hence, both the control and design of a motor need a fast and accurate loss estimation method to ensure higher energy efficiency. As mentioned in the previous section, the losses critical to estimate are the stray and core losses. The work carried out by different researchers on the core losses, stray losses in an induction motor can be broadly classified into four categories, as shown in Fig. 1.1. As far as SL is concerned, the definition, measurement process, and

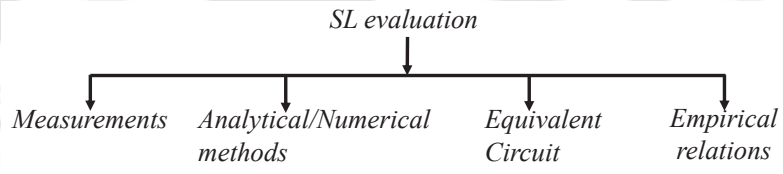

Fig. 1.1: Evaluation of the magnetic losses: *areas of research and practices.*

the recommended allowance of SL vary significantly among the various prominent standards followed worldwide. For example, according to the standard IEEE112B, stray losses are defined as ”the fraction of the overall losses in a machine not accounted for by the sum of friction and windage, stator and rotor copper loss, no-load core loss” [8]. According to the standard, a fixed proportion of the motors output power can be presumed if the SL measurement is impossible. This fixed percentage varies between 0.9 to 1.8 in four slabs depending upon the motor’s power rating [8]. Another universal standard IEC 60034-2-1 defines SL as the sum of losses caused by load current in the core and other metal elements other than stator and rotor conductors, eddy

current losses in windings in result of load current-dependent flux pulsations and extra brush losses generated by commutation [9]. Unlike the slab-wise distribution of IEEE 112B, IEC 60034-2-1 presents a linear-log empirical expression for the SL percentage. In this expression, the fraction of SL (*ie*, SL per unit output power) shows a continuous variation from 0.005 to 0.025. JEC 37, the Japanese Electrotechnical Committee's standard, deemed SL a trivial loss until the release of its upgraded version, JEC 2110, in 2017 [10]. The JEC 2110's explanation of SL is analogous to the same as the standard IEC 60034-2-1 [11].

The fact that all of these criteria do not treat the SL the same way leads some uncertainty about the motor's efficiency. Cao *etal*. *et al.* investigated 15 motors ranging from 11 kW to 150 kW and performed calorimetric tests to understand the changes in efficiency ratings while using different standards [12]. The study corroborates that varying standards result in different efficiency values of the motor.

Besides the standards, several scholars have devised model representations to determine the SL. By defining SL as an excess core loss on load, Gao *et al.* in [13] and Cheaytani *et al.* in [14] estimated SLs using 2-D and 3-D FEM models of IM, respectively. These studies computed the core loss using time-varying magnetic field harmonics and material loss coefficients (Ke, Kh) as constants in a post-process. However, it has been shown that the loss coefficients differ considerably with field density and frequency [15]. Keeping the coefficients Ke and Kh constants results in significant changes in the core loss and, consequently, the computed SL. The major limitation of FEM-based approaches is that they necessitate comprehensive data of motor's geometry and material. This restricts their adoption for the motors already in operation whose detailed geometry and material characteristics are are not available.

Several equivalent circuit-based techniques have been presented to represent the SL to circumvent the limitations of FEM-based methods. In this line, K. Yamazaki *et al.* provided an electrical equivalent circuit-based approach [16]. They included an extra resistance in the secondary of IM's T-model equivalent circuit to adjust for SL. Levi *et al.* used a resistance connected in parallel with the secondary leakage inductance to represent SL in [17]. Other circuits of this type are reported by [18–20]. M.Basic *et al.* proposed an interesting technique

for formulating the SL and core losses in [21]. However, the expression given in [21] is developed for motors that have already been installed, and its application requires at least one SL measurement value.

Several equivalent circuit-based approaches to represent the SL have been proposed to overcome the limitation of FEM based models. K. Yamazaki *et al.* presented an electrical equivalent circuit-based approach to determine SLs [16]. To take into account SL, they added an extra resistance in secondary of IM's T-model equivalent circuit. In [17], Levi *et al.* represented SL by a resistance connected in parallel with the secondary leakage inductance. Other such circuits are represented in [18–20]. In [21], M.Basic *et al.* presented an interesting approach to formulating the SL along with the core losses. The formula presented is developed for motors already installed and needs at least one value of measured SL for each motor.In recent times, Pragasen Pillay *et al.* [22] proposed a statistical analysis based SL formula. According to this formula, SL remains 1.1% of input power for a medium power IM. A similar investigation by Agamloh *et al.* claims the SL to be 1.2% of the input power the motors of 0.75 kW-150 kW at 60Hz [23]. These formulae provide the fixed values of the SL fraction $i.e, SL/P_{Out} or SL/P_{In}$ (1.1% or 1.2%).

Another important magnetic loss *i.e*, CL is relatively (in comparison to the SL) more explored in terms of empirical modelling and analytical formulations. Many time and frequency domain models are reported in the literature for evaluation of CL in the post-FEA calculations [24, 25]. These models are, in fact, the adjusted or extended versions of the two fundamental CL models *i.e.*, Steinmetz equation and, two-term (eddy current and hysteresis losses) CL model [25, 26]. The up-gradation in these two models progresses from introducing the of excess loss term [27] to variabilisation of the loss coefficients [15, 28–32] and enhancements to the Jiles-Atherton (JA) model [33, 34]. All these models have their own tradeoffs ranging from the characterization of loss coefficients [35], lack of flexibility [36], processing time [33], limited application domain, and complex realization [37]. In a baseline evolution, [38, 39] present a rapid CL estimation methods by introducing hysteresis and eddy current loss coefficients. The formula is valid, however, if the supply voltage is equal to the magnetising voltage, which is

valid only for high switching frequency and a modest load.

The recent advancements in the numerical approaches include coupled 1-D and, 2-D/3-D analysis and, the analysis with realising the complex permeability [40], [41]. The imaginary part of the permeability is computed according to the eddy-current and hysteresis losses estimated in the appearance of skin-effect. As long as an equivalent elliptical loop can substitute the quasistatic loop, the concept of complex permeability is valid. At low and medium flux densities, however, it is usually not achievable [42]. Another type of coupled techniques use the combination a hysteresis model with a skin-effect allied 1-D eddy current model [37,43,44]. In these techniques [37,43,44], the magnetic vector potential generated from the 2-D model (for each mesh) is fed into the 1-D model developed in the lamination depth. The net magnetisation (H) is calculated by revising the 2-D field residue while accounting for the 1-D model's reaction magnetisation. The combination effectively mimics the complicated dynamic properties of the loss-loops. The coupling of the 1-D and 2-D models, on the other hand, necessitates nested iterative techniques.

Similarly, theadvances in CL analytical modelling propose formulations of magnetisation components relating to theeddy current loss (with skin effect) and hysteresis loss utilising thehysteresis models and include them into the field's Maxwell diffusion equation [45]. However, when numerically solved, these methods exhibit complex implementation, long processing times, and convergence difficulties for numerical solutions. The setting of time step and geometry segmentation are the anothertwo key issues with numerical approaches. The results are highly skewed due to numerical inaccuracies caused by insufficient time-stepping. [29] outlines the computing requirements for these FEM models, which should be met in order to avoid erroneous core loss results.

The three distinct categories of all the existing CL methods can be termed as: a) Superposition based methods(SBM) b.) Non-superposition based methods(NSBM) c.) Hybrid methods. A comparison of these methods is given in Table 1.1.

Table 1.1: Comparison of methods of CL evaluation

		SBM		NSBM			Hybrid
		CC	VC	CC	VC	HLM	
Accuracy							
Low B_m, low f	P_{Eddy}	L	H	L-M	H	NA	VH
	P_{Hyss}	M	L	L-M	L	VH	VH
High B_m,High f	P_{Eddy}	L	M	L-M	M	NA	VH
	P_{Hyss}	L	L	L-M	L	VH	VH
Computation time		S	M	S	M	VH	VH
Model development		NA	M	NA	M	H-VH	VH
Flexibility		VH	H	VH	H	L-M	L-M
Application range		S	M	S-M	M	H-VH	H-VH

CC: Constant Coefficients; VC: Variable Coefficients; S: Small; L: Low; M: Medium; H: High; VH: Very High; HLM: Hysteresis Loss Models; NA: Not Applicable.

1.3 Motivation

The induction motor has been the workhorse of the industry since its inception in the early twenties. In the longevity of its industrial deployment, the IM went through several design evolvements focused on achieving the next higher level of either efficiency or power density. With the recent trend of adopting electric vehicles as means of transportation, the description of motor efficiency gets previewed in a broader range. The motor is expected to exhibit high efficiency for a wide range of operations. The design of a high-efficiency motor always requires a precise evaluation of all the losses incurred in the motor. Two of the uniformly distributed losses in an IM are stray losses and core losses. As briefly mentioned in the previous section, the challenges with these losses include assumptions based on complex formulations of stray losses, the impact of field penetration in lamination, errors in hysteresis losses due to hysteresis minor loops, and exact magnetic field losses field characterisation. These challenges motivate the researcher to find new solutions for determining these losses less time-consuming and more precise. In line with this, the work presented in this report aims to the accurate formulations of the stray and core losses in an IM and incorporate these formulations in motor design methodology.

1.4 Aim of the thesis

The design and construction decisions significantly influence the losses in an electric motor. With growing emphasis on motor efficiency, series of advancements have been observed in the machine design process to reduce the motor's losses. The improvements in material technologies have promoted the use of high-grade electric steel, superior insulating materials. Brazing operation for rotor joints and vacuum pressure impregnations are recent improvements in virtue of enhancements in the manufacturing process. Similarly, the use of smaller air-gap, lesser stack length and, increment in slot fill factor are the major shifts in design strategies. The advancements in manufacturing technologies and finite element analysis have made it convenient to shift towards the advanced slot geometries from the traditional slot geometries. However, the main requirement to design a motor with higher efficiency or operate an exiting motor in an energy-efficient region requires accurate loss estimates.

Hence, the aim of the thesis is outlined as follows:

- Study and analyse the various magnetic losses in an IM and their impact on motor performance.
- Modeling of stray load losses in a medium power three-phase induction motor.
- Accurate estimation of the core losses with FEA based proposed method.
- Design of a high-efficiency IM with applying the proposed loss formulations.

To meet the objectives mentioned above, it remained imperative to design and prototype the various versions of high-efficiency IMs. Also, the measurements of SL and CL for various power supply parameters required the development of a standard test-bench.

1.5 Contribution of the thesis

Considering the objectives mentioned in the previous section, the work presented in this thesis incorporates following principal contributions:

- The work introduces an empirical model of SL, which can be used to estimate the SL in an IM at both the stages *i.e*, during the design of the motor as well as for the IMs already in operation.

- Illustrates the IM design for the reduction of SL adhering to the rule-bases developed with the proposed model.
- Analysis and formulation of the impact of variations in switching frequency, fundamental frequency and load-torque on SL.
- Proposes a CL estimation method for the inverter-fed IM. The method takes into account the accurate realisation of material non-linearity and the impact of hysteresis minor loops.

An experimental setup of drivetrain configuration is developed in the laboratory to validate the work mentioned above. The control strategies for drivetrains are implemented on the dSPACE-1103 platform. Moreover, Moreover, using an eddy current brake (ECB), an hardware emulation model is developed to assess the drive-cycles performance of the drivetrain configuration.

1.6 Organization of the thesis

The renaming thesis chapters are organized as follows:

- **Chapter 2:** This chapter describes the origins and phenomenon involved in various magnetic losses in induction machines. All these magnetic losses are directly linked to the space and time distribution of magnetic flux density. Hence, this chapter details the impact of various structural parameters on motor's flux distribution.
- **Chapter 3:** The chapter details the formulation of stray losses for a grid-connected three-phase induction motor. A large pool of motors' SL measurement values is used to correlate the origins of the SL and the factor affecting ECPs of an IM. Based upon the results of the correlation, an ECP based SL model is proposed. The primary advantage of the model lies in the fact that it can be used both at the design stage as well as for the motors already in operation whose geometry and material details are not known. The impact of loading of the motor is incorporated.
- **Chapter 4:** This chapter discusses design methodology to increase the motors efficiency in line with the proposed SL model. The impact of shapes of stator and rotor slots on SL and, motor performance is detailed. For this, at first, the initial geometry parameters

of the motor are determined. Thereafter, re-shaping and tuning of the slot shapes are explained as the next steps.

Chapter 5: This chapter discusses the impact of inverter power supply on IMs SL values at different load conditions. The three main parameters (switching frequency, fundamental frequency and, shaft torque) describing the state of the motor's operation are selected and, the SL values are measured for the variations in these parameters. The variation is formulated with an empirical relation.

Chapter 6: The proposal of a CL evaluation method is described in this chapter. The impact of variation of lamination thickness on eddy currents losses and, phase differences between the various harmonics of B on hysteresis loss is briefly illustrated. A correct realistic, fast and accurate method is deduced and, its application is demonstrated for total 8 numbers of different IMs.

Chapter 7 This chapter concludes the work of this report with the research outcomes. The chapter also narrates the future scope of the study along which the presented work can be extended.

2

Magnetic Losses in Induction Machines

Contents

2.1 Introduction

Design and operation of energy-efficient motor-driven systems (MDS) require accurate estimates of all the losses incurred in the motor. As a general trend of losses' proportion in an induction motor, the stator copper loss contributes the most, followed by the rotor copper loss, core loss, stray loss. Mechanical loss shares the least. The estimate of these losses provides the information of the motors overall efficiency and the temperature rise, which remarkably influences the types and sizes of insulation and cooling system. Among all the losses in an induction motor, the copper and mechanical losses present a relatively uniform distribution within their geometric space of occurrence. The magnetic losses (stray loss and core loss) show a very high degree of variation within the motor's geometry. This makes the estimation of magnetic losses more complex than the other losses that can be calculated accurately with their lumped parameter-based physics models.

The electromagnetic losses in an induction motor are originated from the distribution of magnetic flux density in time and space. Hence, their sources are categorised as: a.) fundamental flux density b.) space harmonics of flux density c.) time harmonics of flux density. These space and time harmonics of the magnetic flux density are directly linked to the harmonics in magnetomotive force, variation in the permeance of the magnetic flux-path and the magnetic saturation. The present chapter describes the phenomenon involved with the magnetic losses in brief. Also, the chapter attempts to find and formulate the primary variables with which the stray loss in an induction motor can be represented.

2.2 Magnetic field distribution in polyphase induction machine

These space and time harmonics of $B(t)$ are traced to the variation of magnetomotive force MMF. This section describes the space and harmonics in an inverter fed IM and their correlation with SL.

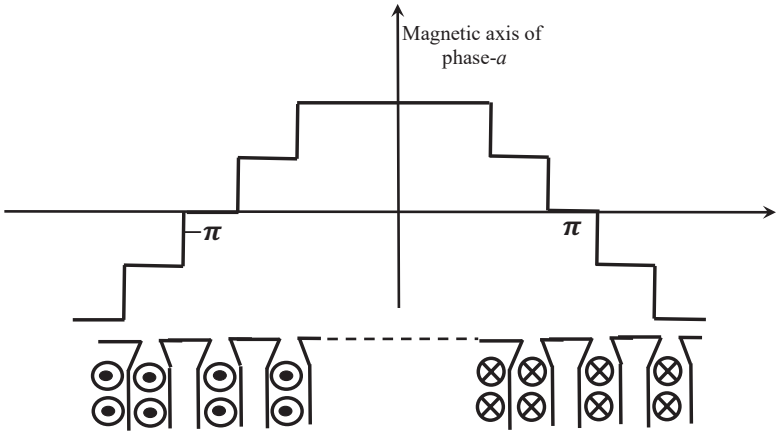

Fig. 2.1: Distribution of the phase MMF- a-phase

2.2.1 Space harmonics in MMF with sinusoidal excitation

Fig.2.1 shows the the distribution of the magnetomotive force (MMF) generated by a distributed winding of one-phase in a three-phase machine [46]. Fourier decomposition of this MMF is given as [47]:

$$F_A(\theta, t) = \frac{2}{\pi} N_S\, i(t) \sum_{\nu=1}^{n} \frac{K_W(\nu)}{\nu} \sin(\nu p\theta) \tag{2.1}$$

where,

$$i(t) = I_m \sin(\omega t) \tag{2.2}$$

where, N_S and, p are, respectively, per phase number of turns in stator winding and, pole-pairs. $K_W(\nu)$ is the winding factor of the ν-th space harmonic. It is expressed in terms of slots per pole per phase (q), coil-pitch (y) and, pole-pitch (τ) as [48]

$$K_W(\nu) = \left(\frac{\sin\frac{\nu\pi}{6}}{q\sin\frac{\nu\pi}{6q}}\right)\left(\sin\frac{\nu\pi y}{2\tau}\right) \tag{2.3}$$

For a three-phase machine drawing a balanced set of currents, the net MMF is given as the sum of MMFs of all the three phases, which are 120 shifted in space and it is:

$$F_S(\theta, t) = F_A(\theta, t) + F_B(\theta, t) + F_C(\theta, t) \tag{2.4}$$

Using (2.1)-(2.4), the net MMF is given as:

$$F_S(\theta,t) = \frac{3}{2}\left[\begin{array}{l} A_1 cos(\omega t - \theta) - \frac{A_5}{5} cos(\omega t + 5\theta) + \\ \frac{A_7}{7} cos(\omega t - 7\theta) ..... \end{array}\right] \tag{2.5}$$

where,

$$A_v = \frac{2}{\pi} N_S I_m . K_W(v) \tag{2.6}$$

Expression (2.5) represents multiple travelling waves rotating in different directions. All these MMF harmonic waves travel with a speed less than the synchronous speed *i.e.*, the speed of the fundamental MMF-wave.The MMF waves corresponding to space harmonic numbers $v = 6k-1$ rotate in the reverse direction of the MMF wave of fundamental whereas, the MMF waves with harmonic number $6k+1$ rotate in the direction of fundamental MMF wave. The space harmonics of order higher than 7 are negligible [49] and hence are neglected.

2.2.2 Space and time harmonics in MMF with inverter fed excitation

For an inverter-fed IM, the motor currents are expressed as:

$$i_a(t) = \sum_{n=1}^{h} I_m(n) \sin(n\omega t + \phi(n)) \tag{2.7}$$

$$i_b(t) = \sum_{n=1}^{h} I_m(n) \sin(n\omega t + \phi(n) - \frac{2\pi}{3}) \tag{2.8}$$

$$i_c(t) = \sum_{n=1}^{h} I_m(n) \sin(n\omega t + \phi(n) + \frac{2\pi}{3}) \tag{2.9}$$

Evaluation of (2.1)-(2.4) for the MMF in relation to the current expressions (2.7)-(2.9), gives:

$$F_S(\theta,t) = F_1(\theta,t) + F_5(\theta,t) + F_7(\theta,t) + ... \tag{2.10}$$

where,

$$F_1(\theta,t) = \sum_{v=1}^{n} A_v cos(v\omega t - p\theta) \tag{2.11}$$

$$F_5(\theta,t) = \sum_{v=1}^{n} A_v cos(v\omega t + 5p\theta) \tag{2.12}$$

$$F_7(\theta,t)=\sum_{v=1}^{n}A_v cos(v\omega t-7p\theta) \tag{2.13}$$

From expressions (2.11)-(2.13), it is seen that the harmonics in current superimpose various high-frequency waves to the MMF waves corresponding to the fundamental frequency. All these rotating MMF waves produce additional SL.

2.2.3 Space distribution of the airgap flux density

Expressions (2.5) and (2.10) give the MMF distribution for winding excitation with sinusoidal and distorted currents, respectively. The average value of the reluctance offered by the airgap is obtained from its effective length neglecting the permeance harmonics due to the slots. The effective length of the airgap is the mean of actual physical airgap (g) which gets enlarged due to the fringing at slot-ends and, it is determined by multiplying the g with Carter's gap expansion coefficient (K_C). With this, the airgap flux density (B_g), for the stator MMF $F_S(\theta,t)$ is

$$B_g(\theta,t)=\frac{\mu_0 F_S(\theta,t)}{gK_C}=\mu_0 F_S(\theta,t)\lambda_g \tag{2.14}$$

where, λ_g is the average value of the airgap permeance $\lambda(\theta,\theta_r)$. The variation in $\lambda(\theta,\theta_r)$ along air-gap periphery due to stator (N_S) and rotor slots (N_R) is given by introducing periodic inverse air-gap function as:

$$\frac{1}{\lambda(\theta,\theta_r)}=g(\theta,\theta_r)=\frac{1}{f_S(\theta)}+\frac{1}{f_R(\theta-\theta_r)}-g \tag{2.15}$$

$$f_S(\theta)=a_0+\sum_{n=1}^{\infty}a_n\cos(nN_s\theta) \tag{2.16}$$

$$f_R(\theta-\theta_r)=b_0+\sum_{n=1}^{\infty}b_n\cos(nN_R(\theta-\theta_r)) \tag{2.17}$$

The magnitudes of these slot permeance harmonics are:

$$\begin{aligned} a_n&=\tfrac{4\beta}{\pi n.g}\left(0.5+\tfrac{X^2}{0.78-2X^2}\right)\sin(1.6\pi X)\,;\\ b_n&=\tfrac{4\beta}{\pi n.g}\left(0.5+\tfrac{Y^2}{0.78-2Y^2}\right)\sin(1.6\pi Y)\end{aligned} \tag{2.18}$$

where,

$$X=\left(\frac{n.B_{S0}}{t}\right)_{Stator},\ Y=\left(\frac{n.B_{S01}}{t}\right)_{Rotor}\ \text{and,}\beta=f(B_{SO}/g).$$

t denotes the tooth width. a_0 and b_0 are the inverse of average effective air-gap length i.e., $1/(gK_C)$. Higher magnitudes of a_n and b_n lead to increased SL components linked with the space distribution of air-gap flux density (*i.e.*, no-load surface core losses and tooth flux pulsation core losses). With the closed rotor slots, $b_{n>1} = 0$.

Apart from the slot openings, the factor which affects the variation of airgap flux density in a symmetrical induction machine is the magnetic saturation of the iron core. The overall saturation in a machine is attributed to the two components of the net flux *viz*. leakage flux and the main (magnetising) flux. The impact of saturation is deemed as a reduction in the magnetic permeability. Hence, the saturation caused by the leakage flux (which occurs in the slots) is modeled mathematically with an increased slot opening. Since the magnetic field distribution in space is close to the sinusoidal, the variation in slot opening is also represented by a sinusoid with a mean value equal to the physical slot opening. The per-unit variation in the slot-opening (κ) can, therefore, be represented as

$$\kappa = 1 - \gamma \cos(2\theta - \omega t) \tag{2.19}$$

The variation expressed by 2.19 ultimately affects the magnitudes of the slot permeance harmonics of 2.18. The impact of saturation caused by the main field is included just with introducing a staurion factor (K_S).

$$\lambda_g(\theta, \theta_r) = \lambda_g \left(\frac{1}{1 + K_{S1}} + \frac{\sin(2\theta - \omega t - \varphi_m + \varphi_1)}{1 + K_{S2}} \right) \tag{2.20}$$

The airgap flux density variation with taking into account all the variations of the magnetic permeance (2.15-2.20) is hence expressed as

$$B_S(\theta, t) = \frac{\mu_0 F_S(\theta, t)}{gK_C} = \mu_0 F_S(\theta, t) \lambda_g(\theta, \theta_r) \tag{2.21}$$

2.2.4 Magnetic flux densities in the ferromagnetic structures

The expression for airgap flux density (2.21) constitutes multiple harmonics of different time frequencies and spatial distributions. A typical space harmonic of this distribution with

order v, time-frequency ω_i and, magnitude B_{gmv,ω_i} is expressed is

$$B_{gv,\omega_i} = B_{gmv,\omega_i} cos(\omega_i t - vp\theta) \tag{2.22}$$

For a linear iron core, the governing equations for the 2-dimensional field distribution (in x and y direction only) are

$$\nabla \times B_{gv,\omega_i} = 0,$$

$$\nabla . B_{gv,\omega_i} = 0,$$

which leads to

$$\nabla^2 B_{gv,\omega_i x} = 0, \nabla^2 B_{gv,\omega_i y} = 0 \tag{2.23}$$

The flux density component decreases along the direction-y *i.e.*, towards the zero value of magnetic potential, so

$$B_{gv,\omega_i y} = f(y) cos(\omega_i t - vp\theta) \tag{2.24}$$

also, with

$$\frac{\partial B_{gv,\omega_i x}}{\partial x} + \frac{\partial B_{gv,\omega_i y}}{\partial y} = 0 \tag{2.25}$$

the variation is given as

$$B_{gv,\omega_i x} = \left(\frac{\frac{\partial f(y)}{\partial y}}{\frac{v}{R}} \right) \sin(\omega_i t - vp\theta) \tag{2.26}$$

where,

$$f(y) = B_{gmv,\omega_i} e^{\frac{vy}{R}} \tag{2.27}$$

The expression (2.27) shows an exponential decay of the flux density along the depth of the motor (towards the shaft, in negative y-direction) from the airgap. Same trend is achieved towards the depth of stator yoke.

2.3 Magnetic losses in induction machine

2.3.1 Core loss

Based upon the phenomenon involved, the core loss is considered a sum of two distinct losses: eddy current loss and hysteresis loss. The loss generated by the induced small circulating currents (as shown in Fig.2.2) in the iron core results termed as eddy current loss which is given

by

$$P_{Eddy} = \int \sigma J_{eddy}^2 dV \tag{2.28}$$

where, V, J_{eddy}, σ denote the volume, eddy current density and electrical conductivity of the core, respectively.

Another component of the core loss, *i.e*, hysteresis loss is the result of work done by the magnetising force against the internal friction of the magnetic domains. The hysteresis nature of the iron core results a hysteresis loop when subjected to a cyclic variation. The area of the loop in the $B-H$ plane (as shown in Fig.2.3) gives the measure of energy loss in one cycle and, the power loss corresponding to it is given by

$$P_{Hyss} = fV \int H.dB \tag{2.29}$$

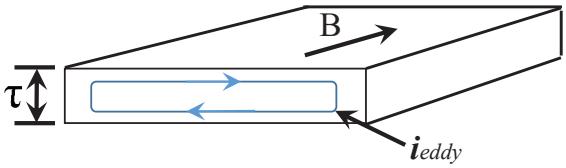

Fig. 2.2: Eddy current path in a ferromagnetic slab

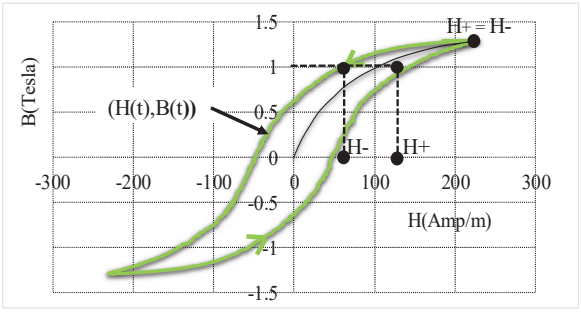

Fig. 2.3: Hysteresis loop

Both these two components of the core loss depend upon the magnitude and, the rate of change of flux density. Chapter 6 comprehensively discusses the core loss evaluation for an induction machine.

2.3.2 Stray loss: primary variables for the representation of stray loss

Various components of SL are, in fact,the additional eddy current losses (P_{Eddy}) in response to the space and time harmonics. The expression for P_{Eddy} for a sinusoidal excitation of flux-density magnitude B_m and, frequency f is given as:

$$P_{Eddy} = k_e \omega^2 B_m^2 \tag{2.30}$$

SL is the portion of the net P_{Eddy} in a machine, generated by the space and time harmonics. These harmonics are generated from air-gap flux variation due to the slots, magnetic saturation and, leakage flux [8-11]. Net P_{Eddy} produced by all the harmonics is:

$$P_{Eddy} = k_e B_{m1}^2 \omega_1^2 + \sum_{v=2}^{n} k_e B_{mv}^2 \omega_v^2 \tag{2.31}$$

where, B_{mv} and ω_v are the flux density magnitude and frequency of the v-th space harmonic,respectively. Denoting $k_e B_{m1}^2 \omega_1^2$ as P_{Eddy1} *i.e.*, eddy current loss corresponding to the fundamental air-gap flux density (B_1) and fundamental frequency (ω_1),

$$P_{Eddy} = P_{Eddy_1} \left(1 + \sum_{v=2}^{n} \left(\frac{B_{mv}}{B_1} \right)^2 \left(\frac{\omega_{mv}}{\omega_1} \right)^2 \right) \tag{2.32}$$

The SL due to v-th harmonic is:

$$SL_V = P_{Eddy1} \left(\frac{B_{mv}}{B_1} \frac{\omega_{mv}}{\omega_1} \right)^2 \tag{2.33}$$

SL is hence,

$$SL = P_{Eddy_1} \left(\sum_{v=2}^{n} \left(\frac{B_{mv}}{B_1} \right)^2 \left(\frac{\omega_{mv}}{\omega_1} \right)^2 \right) \tag{2.34}$$

Two of major SL components in a non-skewed IM are surface eddy current losses and, tooth flux pulsation losses [46, 50, 51].

2.3.2.1 Surface eddy current losses

Modulation of the air-gap flux density due to slots results in higher-order space harmonics, creating additional eddy current losses on the surface of the stator and rotor laminations. The impact of stator slot openings is prominent and hence, the surface losses produced by the

rotor slots is negligible [46]. Harmonic numbers of the travelling flux-density waves of these harmonics are $v = N_s \pm p$ [46]. Frequency of the additional eddy currents induced on the rotor surface (corresponding to the $v = N_s \pm p$) is hence,

$$f_v = s_v f_1 \Rightarrow f_v = \left(1 - \frac{N_s \pm p}{p}\right) f_1 = \frac{N_s}{p} f_1 \tag{2.35}$$

The magnitudes of these harmonics are determined from the magnitudes of the variations in MMF due to slots as [49]

$$\frac{B_{mv}}{B_1} = \frac{F_{mv}\lambda_v}{F_1\lambda_1} = \frac{F_{mv}\lambda_{sv}}{F_1\lambda_{1s}} = \frac{L_{msv}}{L_{m1}} \tag{2.36}$$

where, F_{mv}, F_1 are, respectively, the v-th harmonic and fundamental MMFs. λ_m, λ_1 are specific permeances of v-th harmonic and fundamental flux paths, respectively. L_{mv} is magnetising inductance corresponding the v-th harmonic expressed as [46]

$$L_{mv} = \frac{6\mu_o (T_{Ph} K_w)^2}{\pi . v^2} \left(\frac{L.D}{p^2 . g . K_C . K_{Sv}}\right) \tag{2.37}$$

SL due to the eddy current losses corresponding to these harmonics (as per (5)) is:

$$SL_{surf} = P_{Eddy_1} \left(\left(\frac{N_s}{p}\right)^2 \sum_{v=2}^{n} \left(\frac{B_{mv}}{B_1}\right)^2 \right) \tag{2.38}$$

from 2.36-2.38

$$SL_{surf} = P_{Eddy_1} \left(\left(\frac{N_s}{p}\right)^2 \sum_{v=1}^{n} \left(\frac{L_{msv}}{L_{m1}}\right)^2 \right) \tag{2.39}$$

Using the expression for zig-zag leakage inductances (zig-zag leakage inductance is the sum of all the harmonic magnetising inductances other than fundamental [46]),

$$L_{lz} = \sum_{v=2}^{n} L_{mv} \tag{2.40}$$

from (2.39) and, (2.40),

$$SL_{surf} = P_{Eddy_1} \left(\frac{N_s}{p}\right)^2 \left(\frac{L_{lsz}}{L_m 1}\right)^2 \tag{2.41}$$

2.3.2.2 Flux pulsation losses

The variation in the main flux path permeance due to change in rotor position results in flux pulsation losses both in stator and rotor. The impact of rotor slot is very small in case closed or

narrow-opening rotor slots. The frequency of eddy currents generated by the flux pulsation due to stator slot openings is $f_v = \frac{N_s}{p} f_1$ and, the same due to rotor slot openings is $f_v = \frac{N_r}{p} f_1$. The magnitudes of these harmonics are given as [50]

$$B_{mtv} = K_{tv} B_1 \left(\frac{t_s}{b_{s0}} \right) \tag{2.42}$$

where, neglecting the skewing,

$$K_{tv} = 1 - \frac{L_{mv} + L_{lsz}}{L_{mv} + L_{lsz} + L_{Slot}} = \frac{L_{Slot}}{L_{mv} + L_{lsz} + L_{Slot}} \tag{2.43}$$

here, L_{Slot} is the slot leakage inductance. With $L_{mv} \gg L_{Slot} + L_{lsz}$,

$$B_{mtv} = \left(\frac{L_{Slot}}{L_{mv}} \right) \left(\frac{t_s}{b_{s0}} \right) B_1 \tag{2.44}$$

where, t_s and, b_{s0}, respectively represent the slot pitch and, slot opening. SL corresponding to these harmonics in stator is calculated as

$$SL_{pulsS} = P_{Eddy_1} \left(\left(\frac{N_s}{p} \right)^2 \sum_{v=2}^{n} \left(\frac{B_{mtv}}{B_1} \right)^2 \right) \tag{2.45}$$

With using (2.42)-(2.45),

$$SL_{pulsS} = P_{Eddy_1} \left(\left(\frac{N_s}{p} \right)^2 \left(\frac{L_{SlotS}}{L_{m1}} \frac{t_{sS}}{b_{s0S}} \right)^2 \right) \tag{2.46}$$

similarly, for rotor

$$SL_{pulsR} = P_{Eddy_1} \left(\left(\frac{N_R}{p} \right)^2 \left(\frac{L_{SlotR}}{L_{m1}} \frac{t_{sR}}{b_{s0R}} \right)^2 \right) \tag{2.47}$$

With (2.41),(2.46) and, (2.47)

$$SL = SL_{surf} + SL_{pulsS} + SL_{pulsR} \tag{2.48}$$

$$\Rightarrow SL = P_{Eddy_1} \left(\frac{N_s}{p} \right)^2 \left(\begin{array}{l} \left(\frac{L_{lsz}}{L_m} \right)^2 + \left(k_s \frac{L_{SlotS}}{L_{m1}} \right)^2 + \\ \left(k_r \frac{L_{SlotR}}{L_{m1}} \right)^2 \end{array} \right) \tag{2.49}$$

where, $k_s = \frac{t_{sS}}{b_{s0S}}$ and, $k_r = \frac{N_R t_{sR}}{N_S b_{s0R}}$. Equation (20) is written in form of IM's output power with using the relations shown in (2.50)-(2.53)

$$P_{Out} = 3\left(\frac{\omega^2 \lambda_s^2}{Z_s}\right)\cos\phi \tag{2.50}$$

where, ω,λ_s,Z_s and, cosϕ denote supply frequency,stator flux linkage, input impedance and, power factor of a three phase IM. Rewriting (2.50) in terms of average air-gap flux density (B) results:

$$P_{Out} = 3\left(\frac{\omega^2 (T_{Ph}^2 B^2 A^2)}{Z_s}\right)\frac{R_R}{Z_s} \Rightarrow P_{Out} = 3\left(\frac{T_{Ph}^2 A^2 R_R}{Z_s^2}\right)\omega^2 B^2 \tag{2.51}$$

where, T_{Ph}, A, R_R are, respectively, the stator number of turns/phase,area under a pole,and rotor resistance. The expression of eddy current loss is:

$$P_{Eddy} = k_e \omega^2 B^2 \tag{2.52}$$

Comparing (2.51) and (2.52),

$$\Rightarrow P_{Eddy} = k^2 P_{Out} \tag{2.53}$$

From (2.49) and,(2.53),

$$SL = k^2\left(\frac{1}{p}\right)^2\left(\left(\frac{L_{lsz}}{L_{m1}}\right)^2 + \left(k_s\frac{L_{SlotS}}{L_{m1}}\right)^2 + \left(k_r\frac{L_{SlotR}}{L_{m1}}\right)^2\right)P_{Out} \tag{2.54}$$

Since, in an IM $L_{lSlotS} \gg L_{lzs}$, $L_{lS} \approx L_{lSlotS}$ and, $L_{lR} \approx L_{lSlotR}$, the expression (25), with denoting L_{m1} as L_m yields the primary variables developing a stray loss model for the induction motor as

$$\frac{1}{p}\frac{L_{lS}}{L_m}, \ \frac{1}{p}\frac{L_{lR}}{L_m} \text{ and, } P_{Out}.$$

Chapter 3 of this report explains in brief the development of the SL model using these terms and, the SL measurement data.

2.4 Conclusion

This chapter presents a comprehensive analysis of the distribution and distortions in the magnetic field density in an induction motor. This distribution significantly affects the magnetic losses of the motor. The analysis leads to the preliminary findings of the chapter, which narrates the influences of various magnetic circuit parameters of the motor on the stray losses. These parameters include different inductances of the induction motor. The modeling of stray loss in the induction motor using these parameters is discussed in chapter 3 and Chapter 5 whereas, chapter 6 presents the accurate evaluation of the core loss of the motor considering the effect of all the harmonics discussed in this chapter.

3

Formulation of Stray losses in Medium-power Three-phase Induction Motors

Contents

3.1 Introduction

Stray losses in an induction motor comprise multiple components that originate from the several structural requirements to make a motor and the various non-linearities. The structural requirements primarily include formation of the stator and rotor slots and fixing the windings in them. Similarly, the magnetisation non-linearity is the most effective with others being the non-linearities associated with the electrical an d thermal conductances. As discussed in section 2.3 of the previous chapter, analytical evaluation of all these SL components is not straightforward, it is time-taking and associated with several assumptions.

In this chapter, an electrical circuit parameters (ECPs) based SL model in IM is presented to overcome the limitations of the previously proposed SL formulations. The ECPs used in this model are the lumped circuit parameters used to represent an induction motor's classical T-network equivalent circuit. Shapes of the stator and rotor slots of a motor affect the distribution of the magnetic field density, which has a direct impact on SL. In the equivalent circuit, the effect of the stator-rotor slots on the magnetic field gets reflected by their corresponding leakage and magnetization inductance. The work presents an SL model as a function of these inductances.

3.2 SL Modelling: Sources of SL and proposed Models

For the development of an SL model, it is imperative to recognise and understand the factors influencing it. The three fundamental sources of the SL comprise leakage fluxes [50], space-harmonics, and time-harmonics in the motor's air-gap field [52]. The step wise distribution of the windings' MMF and variation in the reluctance along the air-gap due the rotor and stator slots result in spatial harmonics, whereas the time harmonics are consequences of magnetic saturation predominantly in tooth tips of the slots and the power supply. Table 3.1 summarises all these sources of SL in an IM. It is, therefore, necessary for the loss model to include all these eleven causes. However, direct measurement or estimation of these sources is difficult; it becomes mandatory to represent them with measurable quantities. The most convenient and relevant measurable quantities in this regard are the motor inductances. The sources of SL mentioned in Table 3.1 are linked with the various inductances of an IM, and this enables

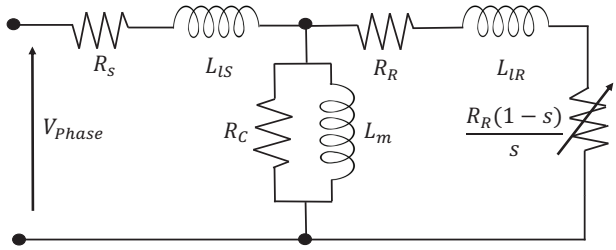

Fig. 3.1: T-model equivalent circuit of IM.

us to develop an SL model, which is a function of these inductances. The typical T-network equivalent circuit of an IM, as shown (neglecting the core losses) in Fig. 3.1, comprises three inductances, which are the stator leakage inductance (L_{lS}), rotor leakage inductance (L_{lR}), and the magnetisation inductance (L_m). The proposed model uses these three inductances to formulate the SL.

Table 3.1: Various Sources Of SL

Sr.No.	Source	Lead to
1	Stator slot leakage flux (ϕ_{lSS})	
2	Rotor slot leakage flux (ϕ_{lSR})	
3	Zig zag leakage flux (ϕ_{lzg})	
4	Skew leakage flux (ϕ_{lskew})	leakage fluxes
5	Belt leakage flux (ϕ_{lbelt})	
6	Overhang leakage flux (ϕ_{lOHS})	
7	Incremental leakage flux (ϕ_{lin})	
8	Peripheral leakage flux (ϕ_{lperi})	
9	Harmonics in air gap MMF	space
10	Variation in slot permeance	harmonics
11	Magnetic saturation in tooth tips	time harmonics

3.2.1 Correlation of SL and leakage Inductances

The first eight sources of SL (as given in Table 3.1 are the different leakage fluxes of an IM associated with the various flux-paths. Fig.3.2 shows the representative flux-paths of the these leakages fluxes. In Fig.3.2, zig-zag (ϕ_{lzg}), belt (ϕ_{lbelt}) and skew leakage (ϕ_{lskew}) altogether form

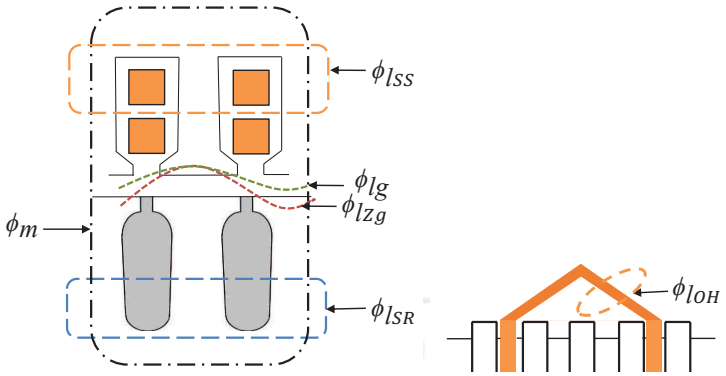

Fig. 3.2: Flux-paths of different leakage fluxes in IM with $q = 2$: *(a) for slot and gap leakage fluxes; (b) for end leakage flux.*

the gap leakage flux (ϕ_{lg}). These leakage fluxes are represented by the leakage inductances of the IM and, their expressions in terms of specific permeances corresponding to these flux paths and, winding pattern of the motor are written as [46]:

For stator leakage inductance((L_{lS})):

$$L_{lS} = \frac{2\mu_o T_{ph}^2 L}{p.q}\left(\lambda_{\text{lg}} + \lambda_{lSS} + \lambda_{lOHS}\right) \tag{3.1}$$

For rotor leakage inductance((L_{lR})):

$$L_{lR} = \frac{2\mu_o T_{ph}^2 L}{p.q}\left(\lambda_{\text{lg}} + \lambda_{lSR} + \lambda_{lOHR}\right) \tag{3.2}$$

where; p,L,T_{ph} and q symbolise the number of pole-pairs, active stack length, number of per-phase stator winding turns, and the number of slots per pole per phase, respectively. λ_{lg}, λ_{lSS}, λ_{lOHS} are the specific permeances that represent the stator side of the air gap leakage flux, slot leakage flux, and overhang leakage flux paths, respectively. The terms λ_{lSR} and λ_{lOHR} are the permeances that represent the rotor's slot leakage and overhang (end ring in case of cage rotor) leakage flux paths respectively. The expressions of these permeances are functions of stator and rotor slot geometries. A higher value of the specific permeance implies higher value of leakage inductance and leakage flux and eventually the higher SL and, hence,

$$SL \propto L_{lS} \text{ and } SL \propto L_{lR} \tag{3.3}$$

3.2.2 Correlation of SL and magnetising Inductance

The remaining three causes (*i.e*, 9 to 11 of the Table 3.1) represent the distribution of MMF, variation of the permeance along the air-gap, and saturation of the tooth bridges. All these factors are directly linked to the magnetisation inductance (L_m) as shown in Fig. 3.1. The analytical expression of (L_m) for a three-phase induction motor is given as [46]:

$$L_{\mathrm{m}} = \frac{\left(T_{ph}K_w\right)F_1}{I_0\sqrt{2}.S} = \frac{6\mu_o\left(T_{ph}K_w\right)^2}{\pi^2}\left(\frac{L.\tau}{p.g.K_C.K_S}\right) \tag{3.4}$$

where, τ , g and K_w are, respectively, the stator pole-pitch, length of the air-gap and winding factor. F_1 denotes the magnitude of fundamental component of the MMF's stepwise spatial distribution which depends upon winding scheme as

$$F_1 = \frac{3T_{ph}I_0\sqrt{2}K_{w1}}{\pi p} \tag{3.5}$$

and,

$$K_C = \frac{\tau}{\tau - 0.5\,\gamma\, g} \tag{3.6}$$

$$\gamma = 4\,\frac{{B_{s0}}^2}{g^2}\left(5 + 2\,\frac{B_{s0}}{g}\right)^{-1} \tag{3.7}$$

In the expression (3.4), the Carter's coefficient (K_C) reflects the effect of slot-openings and flux scattering which ultimately affects the harmonics in air gap MMF [46] and variation in slot permeance [46] (factors 9 and 10 in Table 3.1)). Similarly, the saturation factor (K_S) accounts for the tooth tips' magnetic saturation [46]. In (3.4), these factors (K_C) and (K_S) appear in the denominator, and therefore, the higher value of either of the air gap harmonics or the slot permeance variation results in higher K_C and, consequently lower L_m. The abundance of air gap harmonics or slot permeance variation lead to higher SL. In similar manner, higher saturation in the tooth tips is represented by higher number of K_S, which lowers the L_m and increases the SL. Hence, it can be concluded that,

$$SL \propto \frac{1}{L_m} \tag{3.8}$$

Development of the SL model makes uses of its the above mentioned dependance with the

motor inductances. The next section explains the comprehensive model development.

3.3 Empirical formulation of SL using ECPs and its validation

The proposed SL model uses the motor equivalent circuit parameters (ECPs) L_{lS}, L_{lR} and L_m. Eighteen three-phase induction motors, the series production of TMEIC, Japan are used to evaluate the SL model. The ECPs of these motors are extracted following the procedure specified in IEC 60034-2-1 and test data provided by TMEIC. In addition, TMEIC measured the SL of these motors using the test method described in IEC 60034-2-1. The SL values at rated operating conditions of these motors are expressed as

$$SL = K_{SL} P_{out} \tag{3.9}$$

K_{SL}, in the above expression, is a function of the three inductances L_{lS},L_{lR} and L_m. Based upon the dependency of SL postulated in (3.3) and (3.8), several possible empirical forms of K_{SL} are developed as listed in Table 3.2. Using the ECPs of these motors, the SL values are determined

Table 3.2: Models formulated For Representation of SL

Notation	K_{SL}	Notation	K_{SL}
F1	$\left(\frac{L_{ls}}{L_m}\right)^m$	F4	$\left(\frac{L_{ls}}{L_m}\right)^m + \left(\frac{L_{lr}}{L_m}\right)^n$
F2	$\left(\frac{L_{lr}}{L_m}\right)^m$	F5	$\left(\frac{L_{ls}}{L_m}\frac{L_{lr}}{L_m}\right)^m$
F3	$\left(\frac{L_{ls}}{L_m} + \frac{L_{lr}}{L_m}\right)^m$	F6	$\left(\frac{L_{ls}}{L_m}\right)^m \left(\frac{L_{lr}}{L_m}\right)^n$

by applying the six empirical relations given in Table 3.2. The exponents m and n used for these models are estimated adopting a two-stage procedure. Wherein, at first, the initial values of exponents are evaluated using the non-linear regression with 18 motors' measured SL values. Here, with leakage, magnetising inductances as variables and indices as constants, the expressions of K_{SL} or K'_{SL} (shown in Table 3.2/Table 3.3) are used as a predictive regression model. Five-fold cross-validation is used to fine-tune these initial values. The SL test data of 18 motors

is arbitrarily partitioned into five sub-sample sets of almost similar size without recurrence.Four of the five sample sets are utilised as training data, and the SL model's indicesare determined by fitting the model to these training data. Using the retrieved exponents, the SL for the test data set is determined.

The process is repeated five times, each time with a distinct set of training and test data.

For each (*ith*) repetition, the perdition error ($e_r(i)$) is determined as (3.10):

$$e_r(i) = \sum_{t=1}^{S} \left(P_{SLM(t)} - P_{SLC(t)}\right)^2 \tag{3.10}$$

where, $P_{SLM(t)}$ is the measured value of SL for motor t of the test data set;$P_{SLC(t)}$ is the calculated value of SL for the motor using the exponents evaluated with training data set and S denotes test data sample size. At the end of five repetitions, cross validation error (CV) is calculated as:

$$CV(x) = \frac{1}{5} \sum_{i=1}^{5} e_r(i) \tag{3.11}$$

The method is repeated until the CV value is reduced to a minimum. The final exponents are those that correspond to the absolute lowest of CV.

Table 3.6 indicates the percentage of errors in computing SL with respect to (*w.r.t.*) the measurements values. Table 3.6 reveals that, in comparison to the four models, models F1 and F6 provide SL that is closer to the measurement, with standard deviations of errors of 16.98 and 19.73, respectively. The fluctuation in the values of the exponents m and n among the motors of different pole-pairs, as shown in Table 3.7, however is the main shortcoming of these models.

Table 3.5 and Table 3.7 show, respectively, the calculated with the six SL models and the exponents' values for these models. Table 3.6 shows the percentage of errors in the calculation of SL with respect to (*w.r.t.*) measured values. The values of Table 3.6 show that the models F1 and F6 give SL closer to the measurement in comparison to the other four models, and the standard deviation of errors for F1 and F6 are 16.98 and 19.73, respectively. However, the main shortcoming of these models is the variation in the values of the exponents m and n among the motors of different pole-pairs, as shown in Table 3.7. The term, number of pole pairs p, is included in the model expressions F1-F6 in an attempt to address this. The formulas for K_{SL}

are changed as a result of this modification, as shown in Table 3.3. Where, K'_{SL} denotes the modified K_{SL} expressions.

Table 3.3: Modified Expressions of K_{SL} (K'_{SL})

Notation	K'_{SL}	Notation	K'_{SL}
F1	$\left(\frac{L_{ls}}{p.L_m}\right)^m$	F4	$\left(\frac{L_{ls}}{pL_m}\right)^m + \left(\frac{L_{lr}}{pL_m}\right)^n$
F2	$\left(\frac{L_{lr}}{pL_m}\right)^m$	F5	$\left(\frac{L_{ls}}{pL_m}\frac{L_{lr}}{L_m}\right)^m$
F3	$\left(\frac{L_{ls}}{pL_m} + \frac{L_{lr}}{pL_m}\right)^m$	F6	$\left(\frac{L_{ls}}{pL_m}\right)^m\left(\frac{L_{lr}}{pL_m}\right)^n$

Table 3.4: Specifications of TMEIC Motors Of Different Ratings and Pole-pairs Used For Development of The SL Models

Motor	p	P_{out} (kW)	rpm	I_S	pf	Motor	p	P_{out} (kW)	rpm	I_S	pf
M1	1	75	2970	130	0.878	M10	2	132	1485	240	0.834
M2	1	132	2976	220	0.896	M11	2	200	1487	355	0.859
M3	1	160	2979	275	0.875	M12	2	315	1487	560	0.851
M4	2	75	1482	132	0.864	M13	2	355	1486	660	0.854
M5	2	110	1484	200	0.844	M14	3	75	987	145	0.796
M6	2	160	1486	282	0.856	M15	3	90	989	170	0.801
M7	2	250	1486	435	0.869	M16	3	132	989	245	0.82
M8	2	375	1485	660	0.858	M17	3	160	989	295	0.825
M9	2	90	1482	160	0.857	M18	3	200	989	380	0.797

Tables 3.8 and Table 3.9 show the SL values computed with the updated K_{SL} expressions and, the error compared to themeasured SL. Table 3.10 lists the exponents utilised inthe modified expressions. The impact of incorporating the pole-pair term p in the SL models can be described as follows when comparing Tables 3.6 and Table 3.9:

- Not all models (F1 to F6) are affected in similar manner by this amendment.
- With this change, the standard deviations of errors for the models F1, F3, and F6 observe the reductions, while the same for the models F2 and F5 show increments.

Table 3.5: Calculated SL Values (In kW) For The 18 Motors With The 6 Models

Motor	SL-Measured	SL-Calculated with proposed 6 models					
		F1	F2	F3	F4	F5	F6
M1	0.56	0.72	0.58	0.71	0.60	0.65	0.63
M2	1.09	1.05	0.87	1.01	0.87	0.96	0.93
M3	1.25	1.35	0.89	1.21	1.13	1.09	1.12
M4	0.45	0.39	0.23	0.48	0.46	0.47	0.50
M5	0.74	0.63	0.38	0.79	0.74	0.75	0.80
M6	0.94	1.11	1.31	2.10	1.31	1.77	1.56
M7	1.46	1.27	1.07	1.89	1.51	1.79	1.73
M8	2.29	2.55	4.15	5.93	3.01	4.72	3.78
M9	0.45	0.56	0.12	0.47	0.65	0.42	0.60
M10	0.71	0.88	0.19	0.75	1.04	0.66	0.95
M11	1.55	1.08	0.17	0.80	1.28	0.71	1.11
M12	2.41	1.76	1.49	2.66	2.08	2.46	2.38
M13	2.82	2.30	3.73	5.30	2.72	4.26	3.42
M14	0.23	0.29	0.16	0.18	0.39	0.39	0.25
M15	0.48	0.33	0.42	0.36	0.44	0.63	0.32
M16	1.01	0.74	0.07	0.22	0.97	0.46	52.47
M17	1.20	0.98	0.10	0.30	1.28	0.60	46.59
M18	1.08	1.99	0.13	0.64	2.53	0.98	1.22

- The modification makes the indices m and n of models F4 to F6 independent of the pole number for the minimum values of their standard deviation.
- The exponents of models F1 to F3 still depend upon the number of pole-pairs for their minimum values of standard deviations.
- Prior to this modification, model F1 expressed the least values of average error as well as the standards deviation. The model F6 seconds. The modification does not alter this trend and these two models show the minimum average errors and minimum standard deviations in same order.
- Even after correction, the indices of F1 vary with the number of pole pairs (for the least value of error's standard deviation), which makes model F6 preferable.

The ideally appropriate model among these six models is identified after examining their relative prediction performance as described in section IV.

Table 3.6: Percentage Errors In SL Calculation Using the Proposed Models

Motor	F1	F2	F3	F4	F5	F6
M1	29.38	4.51	27.13	8.42	16.02	0.63
M2	3.58	19.84	7.28	19.80	12.15	14.60
M3	8.61	28.69	3.24	9.51	12.92	10.11
M4	13.47	48.26	7.36	2.58	3.93	11.04
M5	14.74	48.87	7.38	0.78	1.79	8.82
M6	18.07	39.16	123.42	39.06	88.50	66.11
M7	13.06	26.68	29.17	3.20	22.23	18.14
M8	11.36	81.36	159.05	31.67	106.17	65.33
M9	22.60	73.04	2.73	44.48	7.68	32.28
M10	24.51	72.55	5.67	46.36	6.72	33.73
M11	30.50	89.05	48.62	17.75	54.53	28.37
M12	26.79	38.07	10.43	13.35	2.30	1.07
M13	18.48	32.56	88.13	3.49	51.42	21.39
M14	27.02	29.13	20.03	70.12	70.05	9.78
M15	31.77	11.52	24.02	8.09	32.10	32.18
M16	26.81	92.79	78.30	3.86	55.02	52.47
M17	17.94	91.84	74.75	7.29	49.80	46.59
M18	83.30	87.56	40.88	133.66	9.17	12.43
Standard deviation	16.98	29.69	45.41	33.18	31.88	19.73

Table 3.7: Values Of Exponents Used For Proposed 6 SL Models

Model	F1	F2	F3	F4	F4	F5	F6	F6
Pole pairs	m	m	m	m	n	m	m	n
1.00	1.30	1.10	1.45	1.35	2.50	0.60	0.94	0.32
2.00	1.55	1.60	1.80	1.50	3.50	0.73	1.20	0.26
3.00	1.90	2.10	2.70	1.80	4.50	0.90	1.60	0.35

3.4 Selection of the appropriate model

As per the conclusion drawn in the precious section, the SL representations by models F1 and F6 are more significant. In a next step of evaluating the relative capabilities of these models, two models-relative quality estimators *viz.* Akaike Information Criterion (BIC) and Bayesian Information Criterion (BIC) are determined for all the models. The expressions for the AIC and BIC weights (for a discrete distribution) are (3.12),(3.13):

$$AIC(k) = -n.\ln\left(\frac{{\sigma_k}^2}{n}\right) + 2.K(k) \tag{3.12}$$

Table 3.8: Calculated SL Values With K_{SL} modified as K'_{SL}

Motor	SL-Measured	SL-Calculated with proposed 6 models					
		F1	F2	F3	F4	F5	F6
M1	0.56	0.69	0.61	0.71	0.60	0.62	0.58
M2	1.09	1.01	0.91	1.01	0.87	0.92	0.86
M3	1.25	1.31	0.93	1.21	1.13	1.04	1.03
M4	0.45	0.37	0.66	0.32	0.30	0.74	0.36
M5	0.74	0.59	1.03	0.52	0.48	1.17	0.57
M6	0.94	1.00	2.74	1.27	0.85	2.54	1.12
M7	1.46	1.21	2.75	1.23	1.00	2.77	1.26
M8	2.82	2.32	7.91	3.50	1.99	6.62	2.76
M9	0.45	0.51	0.45	0.32	0.42	0.70	0.40
M10	0.71	0.80	0.70	0.51	0.66	1.09	0.63
M11	1.55	1.02	0.72	0.57	0.83	1.23	0.74
M12	2.41	1.65	3.70	1.70	1.37	3.75	1.72
M13	2.29	2.10	7.23	3.15	1.80	6.03	2.51
M14	0.23	0.25	0.12	0.07	0.34	0.58	0.42
M15	0.48	0.28	0.26	0.12	0.39	0.88	0.55
M16	1.01	0.58	0.08	0.09	0.76	0.74	0.71
M17	1.20	0.75	0.10	0.12	0.98	0.96	0.92
M18	1.08	1.34	0.13	0.23	1.72	1.49	1.48

and,

$$BIC(k) = -n.\ln\left(\frac{{\sigma_k}^2}{n}\right) + 2.K(k).\ln(n) \tag{3.13}$$

Where, n is the sample size, σ_k is the residual sum of squares (w.r.t. the measured) SL for $k-th$ model and $K(k)$ denotes number of model parameters.

The model with minimum AIC or BIC score is considered the to express the most accurate representation. The difference between the score a model and, score of the model with least score (possessing the ΔAIC or ΔBIC of zero) provides the model's relative quality. The interpretation of ΔAIC or ΔBIC scores to select a model or to differentiate the two models is reported as follows:

Criterion for AIC (as per Burnham and Anderson [53]):

- For $\Delta AIC < 2 \Rightarrow$ substantial evidence for the model.
- For $7 > \Delta AIC > 3 \Rightarrow$ less support for the model.

Table 3.9: Percentage Error In SL Calculation With K'_{SL}

Motor	F1	F2	F3	F4	F5	F6
M1	24.84	9.23	27.13	8.54	11.48	5.19
M2	7.10	16.10	7.28	19.73	15.72	21.38
M3	4.69	25.24	3.24	9.45	16.50	17.34
M4	17.91	46.70	28.65	32.53	64.56	20.52
M5	20.31	40.70	29.66	34.28	58.78	22.90
M6	6.90	191.55	35.03	9.65	170.32	19.10
M7	17.25	87.90	15.97	31.67	89.01	13.78
M8	17.77	180.94	24.14	29.45	135.09	1.85
M9	13.12	0.99	29.70	7.08	53.78	11.65
M10	13.43	1.73	28.57	6.58	53.42	11.46
M11	34.47	53.47	63.60	46.46	20.59	52.24
M12	31.37	53.94	29.20	43.11	55.80	28.54
M13	8.16	215.82	37.51	21.43	163.43	9.66
M14	8.29	47.44	69.75	45.56	153.20	82.54
M15	40.70	45.33	74.25	18.27	84.32	15.34
M16	43.06	92.59	91.05	25.41	26.54	29.73
M17	37.57	91.81	89.87	18.46	19.53	23.41
M18	23.49	87.80	78.91	58.37	37.12	36.67
Standard deviation	12.35	64.62	27.82	15.44	53.44	18.88

Table 3.10: Exponent Values With K'_{SL}

Model	F1	F2	F3	F4	F4	F5	F6	F6
Pole pairs	m	m	m	m	n	m	m	n
1.00	1.30	1.09	1.45	1.35	2.40	0.60	0.95	0.33
2.00	1.30	1.10	1.56	1.35	2.40	0.60	0.95	0.34
3.00	1.42	1.60	2.10	1.35	2.40	0.70	0.95	0.34

- For ΔAIC $> 10 \Rightarrow$ the model is unlikely.

Criterion for BIC (as per Kass and Raftery [54]): The strength of the evidence against the model with the higher BIC value is given as follows:

- For ΔBIC $< 2 \Rightarrow$ not a significant difference between the two models.
- For $6 >$ ΔBIC $> 2 \Rightarrow$ positive.
- For $10 >$ ΔBIC $> 6 \Rightarrow$ strong.
- For ΔBIC $> 10 \Rightarrow$ very strong

For the selected six SL models (of Table3.3), the values of absolute and relative AIC and BIC scores are given in Table3.11.

Table 3.11: SL-prediction scores of the K'_{SL} models

SL Model	n	σ_k	AIC	ΔAIC	BIC	ΔAIC
F1	4.00	1.78	-33.70	0.00	-30.13	0.00
F2	4.00	60.96	29.96	63.65	33.52	63.65
F3	4.00	5.88	-12.14	21.55	-8.58	21.55
F4	5.00	3.43	-19.83	13.87	-15.38	14.76
F5	4.00	35.76	20.35	54.05	23.92	54.05
F6	5.00	1.77	-31.73	1.96	-27.28	2.85

The values of Table3.11 conclude that, the least values of both AIC and BIC belong to the SL model F1 and, the model F6 comes next to it. However, the relative AIC and BIC scores of F6 (*i.e*, score of F6- score of F1) are 1.96 and 2.85 respectively. This suggests that evaluation with both the F1 and F6 models posses almost equal degree of accuracy and convenience. Since the exponents *m* and *n* of the model F6 do not change with the pole number (as shown in Table 3.10), model F6 is adopted for the SL representation.

Calculated values of SL with the modified F-6 are compared with the four other latest and prominent empirical SL relations reported in the literature. These relations include a). SL formula by Pillay *et al.*; b). SL formula by Agamloh *et al.*; c). SL percentage provided by IEEE 112-B; d). SL's logarithmic expression of IEC 60034-2-1. Fig. 3.3 shows the comparison of SL values obtained from the the proposed and existing models. It is noteworthy to observe from Fig. 3.3 that, for the motors of different power ratings, the trend of calculated SL values, with the proposed model, is in compliance with the results of the existing four SL relations and the measurements. However, the proposed model F-6 shows minimum error in comparison to the existing models. Also, the existing models yield the same SL values for the motors of the same output power but the different pole-pairs, whereas the proposed model F6 results in the different SL values for such motors in line with the measurement.

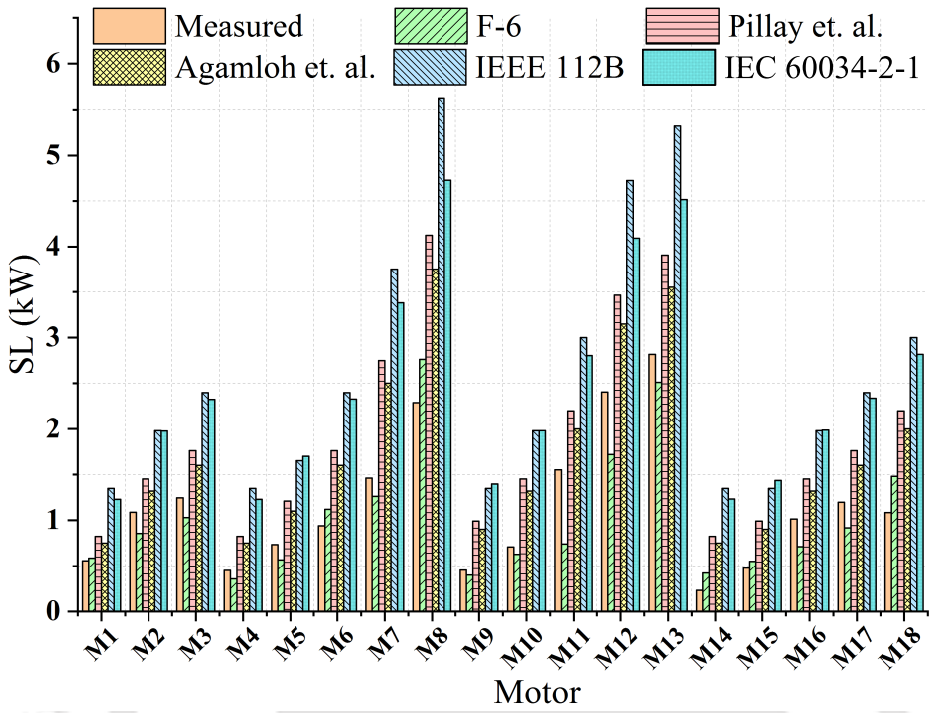

Fig. 3.3: Comparison of the results with: *a).Measurement values of SL b).Proposed SL model F-6 c).SL formula provided by Pillay et al.; d). SL relation provided by Agamloh et al.; e). SL % fixed by IEEE 112-B; f). Logarithmic SL expression of IEC 60034-2-1*

3.5 Impact of motor's loading on SL

The SL formulation presented in above sections provides the rated SL value of a motor. However, in many of industrial applications, motors do not always run at its rated capacity. On an average, 44% of the motors in industrial sector operate with loads less than or equal to 40% of their rated load [55]. SL also changes with loading of the motor and an SL model needs to incorporate it. This section presents the adaption of the proposed model for variable load operation of the induction motor.

3.5.1 SL variation with loading

Eight different IMs of 2.5kW output power are tested to understand the trend of SL variation with the loading. Nameplate details of these motors are given in Table 3.12. These prototype motors are designed with the permutations of two distinct stator and rotor slot designs as shown in Table 3.13 for two different rotor bar materials *i.e*, copper and aluminium. The test set of these motors, hence consists:

- Eight distinct motors of equal power ratings.
- Four sets of two IMs with each set comprising motors of same exactly geometry but different rotor bar cum end-ring material (copper and aluminium).

Table 3.12: Specifications of Tested IMs

Motor	P_{Out} kW	Design		Speed (rpm)	Cage bar material	Voltage /f	Slots N_S-N_r	Lamination thickness
		Stator	Rotor					
M-1	2.5	SD-1	RD-1	1482	Copper	200/50	36-28	0.5mm
M-2	2.5	SD-2	RD-1	1482	Copper	200/50	36-28	0.5mm
M-3	2.5	SD-2	RD-2	1482	Copper	200/50	36-28	0.5mm
M-4	2.5	SD-1	RD-2	1482	Copper	200/50	36-28	0.5mm
M-5	2.5	SD-1	RD-1	1482	Aluminium	200/50	36-28	0.5mm
M-6	2.5	SD-2	RD-1	1482	Aluminium	200/50	36-28	0.5mm
M-7	2.5	SD-2	RD-2	1482	Aluminium	200/50	36-28	0.5mm
M-8	2.5	SD-1	RD-2	1482	Aluminium	200/50	36-28	0.5mm

Table 3.13: Slot Shapes Of The Two Design Prototypes

Stator slots: ***Initial design***	**SD1**	**Stator slots:** ***Modified design***	**SD-2**
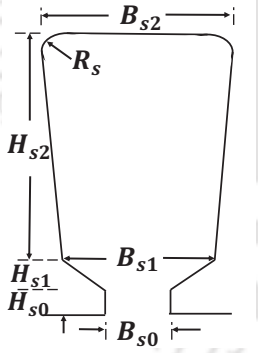	Dim. (mm) B_{s0}=2.4 B_{s1}=6.0 B_{s2}=8.5 R_s=2.75 H_{s0}=1.0 H_{s1}=0.67 H_{s2}=18.33	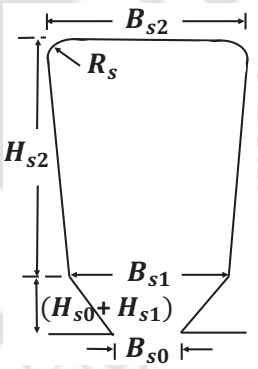	Dim. (mm) B_{s0}=1.5 B_{s1}=6.0 B_{s2}=9.5 R_s=2.5 H_{s0}=0 H_{s1}= 1.67 H_{s2}=18.0
Rotor slots: ***Initial design***	**RD1**	**Rotor slots:** ***Modified design***	**RD-2**
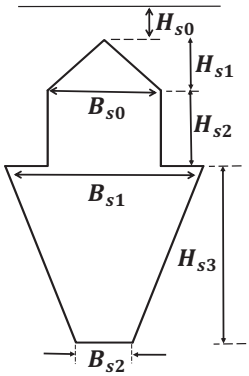	Dim. (mm) B_{s0}=5.5 B_{s1}=6.32 B_{s2}=3.17 H_{s0}=0.3 H_{s1}=1.0 H_{s2}=2.5 H_{s3}=14.0	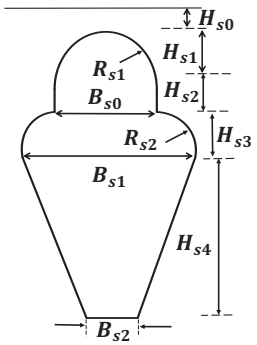	Dim. (mm) B_{s0}=5.0 B_{s1}=6.32 B_{s2}=1.50 H_{s0}=0.3 H_{s1}= 2.25 H_{s2}=1.25 H_{s3}=1.80 H_{s4}= 14.0 R_1=2.4 R_2=3.12

The design parameters common to all these eight IMs are: inner-outer diameters, slot area and end-rings area, stack length and, winding scheme. The eight IMs differ only in terms of slot geometries and rotor bar material. These IMs are tested for SL at variable load conditions adhering the test standard-IEC60034-2-1. Next subsection details the test-procedure and the results.

3.5.2 Experiments and SL test results

The SLs, for the eight IMs are measured using the Eh-star test (as per the procedure mentioned in section 6.2.1). Figure 3.4(a)-(b) show the results for copper and aluminium rotor motors. respectively.

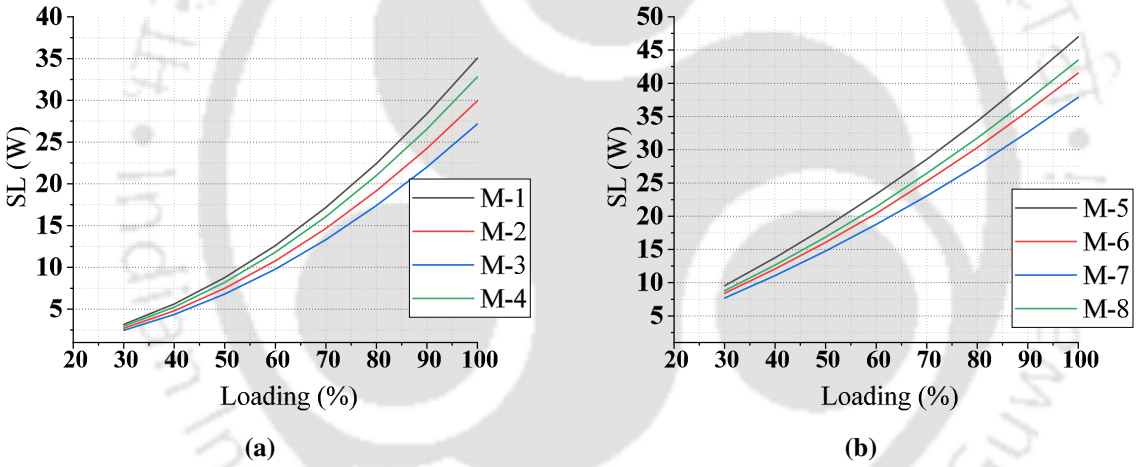

Fig. 3.4: Test results:variation of SL with loading for the 2.5kW IMs: (a) Cu motors, (b) Al motors

The results shown in Fig. 3.4(a)-(b) reveal that:

- All the motors (M1 to M8) provide same rated output power and belong to the same efficiency class yet, their SL values are different.
- SL of an IM does not exactly vary in the same proportion of output power ($i.e. \frac{\partial(SL)}{SL} \neq \frac{\partial(Pout)}{Pout}$) and, this implies that the relation between SL and P_{Out} is not linear. The SL varies with the order of variation higher than unity with output power, and hence a fixed percentage-based formulation of SL *w.r.t.* P_{Out} is not justified for variable load scenarios.
- For the same output power, the motors with aluminium rotors show higher SL values, vis-a-vie copper rotors. This is because of higher values of slips the aluminium rotor motors run at, for the same P_{Out} in comparison to the copper rotor motors. Hence, the

stator current and the leakage fluxes result higher values of SL.

An empirical relation of SL is formulated based on the above observations and rated SL values of set-1. The next section explains the model's development in detail.

3.5.3 Adapting SL model for loading condition

As discussed in previous subsection, the variation of SL with motor's output power is not linear. Followings are the feasible adjustments in the proposed SL model to incorporate impact of motor's loading.

(i) Selecting current dependent leakage inductances (*i.e*, writing L_{lS} and L_{lR} functions of stator and rotor currents, respectively).

(ii) Forming L_m a function of the magnetising current.

(iii) Making the exponents m and n functions of motor's slip.

The L_{lS} and L_{lR} do not vary much with loading due to a large air in the path of leakage flux lines in comparison to the magnetising flux lines(till $I_S/I_{S\,rated} < 2$) [46, 49]. Since the L_{lS} and L_{lR} do not show a significant variation w.r.t load current, they considered constant (as determined from no-load and block rotor test). On the other hand, the L_m changes with the loading because variation in load results in a change of the magnetising voltage due to the change in stator resistive drop as:

$$E_m = V_S - IR_S$$

The magnetising flux-linkage corresponding to the is:

$$\psi_m = \int E_m dt = -\frac{1}{\omega_e} jE_m$$

$$L_m(\psi_m) = \frac{\psi_m}{I_m(\psi_m)}$$

From the above expression, it is evident that L_m is a function of flux-linkage ψ_m, and magnetising current (I_m). Since both, ψ_m and I_m change due to loading, the L_m also changes with loading. The variation of L_m can is evaluated using the no-load test at different voltages, and Fig. 3.5.3 shows a typical L_m variation. It is clear from Fig. 3.5.3 that L_m rises with an increase in load current. However, the L_m variation shown in this figure does not take into account the impact of

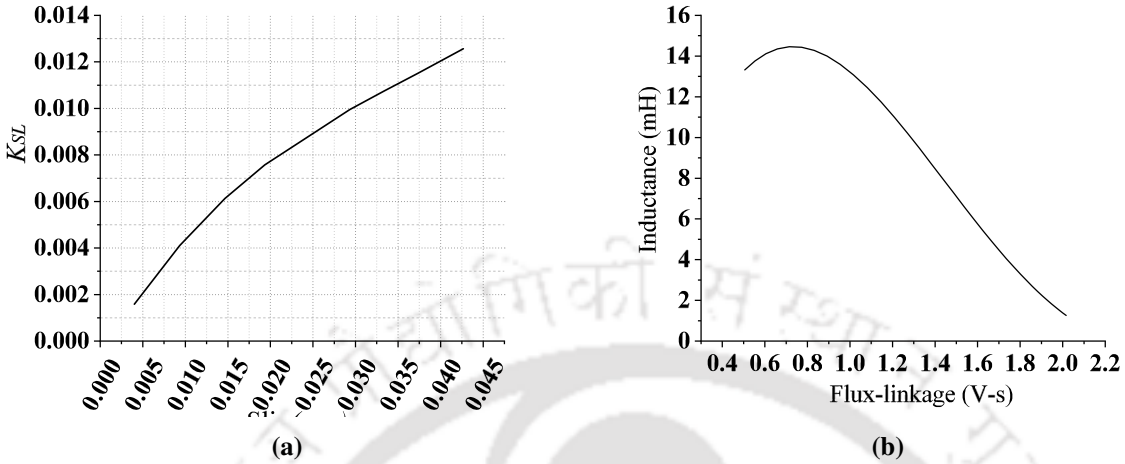

Fig. 3.5: Variations due to load-change: (a) K_{SL} with slip for M-1, (b) L_m with ψ_m.

leakage fluxes as it uses no-load test data and the leakage flux is minimal at no-load conditions.

The other factor that affects L_m is tooth-bridge saturation. As the leakage fluxes increase with the load current, the tooth-bridge begins to saturate. Thereby, the permeance of the slots reduces leading to decrease in L_m.Since, both the above phenomena tend to have an opposing influence on L_m, the L_m variation w.r.t loading is dependent on the motor's geometry. For example, a motor with a higher tooth width has a different L_m variation than a motor with a narrower tooth. To incorporate the effect of L_m variation on SL (i.e. flux dependent variation), the relation is modified for load-dependent L_m as:

$$K_{SL} = \frac{SL}{P_{Out}} = \left(\frac{1}{p}\frac{L_{ls}}{L_m(I_m)}\right)^m \left(\frac{1}{p}\frac{L_{lr}}{L_m(I_m)}\right)^n \tag{3.14}$$

The third option is to make the exponents m and n function of slip. Hence, based on the above discussion, the modified version of (3.14) is:

$$K_{SL} = \left(\frac{1}{p}\frac{L_{lS}}{L_m(I_m)}\right)^{m(s)} \left(\frac{1}{p}\frac{L_{lR}}{L_m(I_m)}\right)^{n(s)} \tag{3.15}$$

To keep the number of variables small, exponent $n(s)$ is taken as a constant multiplier of $m(s)$ with zero offset, i.e. $n(s) = k.m(s)$. Using this, (3.15) becomes:

$$K_{SL} = \left(\frac{1}{p}\frac{L_{lS}}{L_m(I_m)}\right)^{m(s)} \left(\frac{1}{p}\frac{L_{lR}}{L_m(I_m)}\right)^{k.m(s)} \tag{3.16}$$

Determination of the exponents $m(s)$ and $n(s)$ uses measured values of SL fractions in total

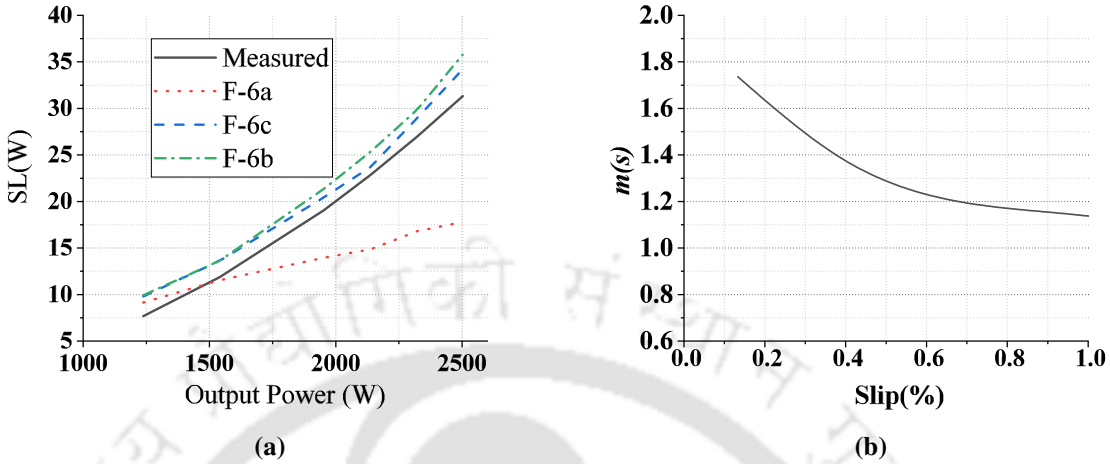

Fig. 3.6: (a) SL variation: Measured and estimated with the three variants of SL model for M-1, (b) Variation of the exponent $m(s)$ corresponding to (3.17)

output power i.e., SL/P_{Out} at different loadings of the motor. This fraction is the measure of K_{SL} by its definition. 3.5.3 shows the K_{SL} variation for the motor M-1. The relation between these K_{SL} values and the $m(s)$ is given as:

$$\frac{1}{m(s)} \log\left(K_{SL}\right) = \log(A) + k\log(B) \tag{3.17}$$

where,

$$A = \frac{1}{p}\left(\frac{L_{lS}}{L_m}\right) \text{and,} B = \frac{1}{p}\left(\frac{L_{lR}}{L_m}\right).$$

The right term in (3.17) is solely a geometry and material dependant term and can be evaluated during the design or the testing. However, neglecting the saturation makes this term a constant and as a result, the variation of $m(s)$ *w.r.t.* loading (or the P_{Out} or the measured K_{SL}) will always lead to a constant:

$$\frac{1}{m(s)} \log\left(K_{SL}\right) \tag{3.18}$$

The $m(s)$ variation meeting this constraint with correlation $R^2 = 0.99$ is deduced as:

$$m(s) = (1 - s)^{\sqrt{2}\pi} \tag{3.19}$$

$$k = \frac{1}{2\sqrt{2}} \tag{3.20}$$

3.6 Conclusion

This work described in this chapter presents a model to estimate the SL for the three-phase grid-connected induction motors. The presented model uses motors' inductances and other nameplate data to determine the SL. The accuracy of the proposed model is compared with results obtained with the other prominent SL formulation present in the literature, which include the SL relations of IM test standards IEC-60034-2-1 and IEEE-112B. It is reported that the proposed model estimates SL more accurately for the given set of induction motors. The SL value in motors increases with the number of poles for the same output power. However, all the existing SL models do not account for this fact while estimating it. The proposed model, being the number of pole dependant, is able to estimate the SL close to the measurement in line with this fact.

An important motor-design related question that arises now is: *"In case two motors have same output power, the same number of poles, the same number of slots on the stator and rotor, will the SL of these motors be different and will the proposed model be able to predict it?"* To answer this, motors of same output power but different slot shapes are designed using the hypothesis the proposed model. The next chapter describes the design of these motors in details.

4

Design of Motors for High Efficiency

Contents

4.1 Introduction

The work presented in this report, regarding the SL, has two-fold objectives. The first objective is to propose a model that can be used to estimate the SL in IMs. For this purpose, we used 18 motors in the range of 75kW to 375 kW. These motors are under series production in TMEIC and have been extensively tested. We used this data to test and calibrate the proposed models. Chapter 2 of this report describes the work on above mentioned first objective. The second objective of the work is to apply the SL model to design of IMs. For this purpose, IMs of 2.5kW output power rating are designed using the SL model obtained in chapter 3. The reason for choosing smaller motors for this purpose are:

- Validation of the model required two stator designs, 2 rotor designs with copper bars and 2 rotors design aluminium bars. Therefore, 2 stators and 4 rotors, in total, are prototyped. The cost of prototyping 2 stators and 4 rotors for 75kW (or higher power) motors was beyond the financial means of the laboratory.
- The lab does not have a test-bed that can be used for reliable measurements beyond 5kW. Moreover, in this work, it can be seen that the proposed SL model works for motors with smaller ratings as well. The experiments also led to the conclusion that it can cover a wide range of IMs. The models can predict the SL for larger as well as smaller motors because it is based on the premise that SLs are dependent on leakage and magnetisation inductions. The large and small motors have a different ratio of leakage to magnetising inductances, and the proposed models capture it.

4.2 Design specifications

4.2.1 Essential standard specifications

The design specification of the motor are as listed below in Table 4.1. It is a radial flux, squirrel cage, three-phase induction motor adhering the IE3 efficiency class. The structure of the motor is aimed to support both the flange and foot mounted IM 2001 arrangements.

Table 4.1: Specifications of 2.5kW Induction Motor

Sr.No.	Specification	Value	Unit	Symbol
1	Continuous shaft power	2.5	kW	P_{Out}
2	Pole-pairs	2	Number	p
3	Rated speed	1485	rpm	N_r
4	Supply voltage (line)	200	Volt.	V_S
5	Frequency	50	Hz	f
6	Phases	73	Number	m
7	Power factor (desired)	≥ 0.85	-	$p.f.$
8	Efficiency (desired)	≥ 0.85	-	η
9	Insulation class	F	-	-
10	Slot fill-factor	0.4-0.65	%	FF
11	Cooling	Air natural	-	-

4.2.2 Design constraints

The design constrains and guidelines followed to achieve the IM design of adequate power density and minimal losses are listed in Table 4.2 - Table 4.4.

Table 4.2: Current densities' allowances

Current densities for air-natural IMs:				
Sr.No.	Specification	Value	Unit	Symbol
1	In stator conductors	5	A/mm^2	J_S
2	In rotor bars	2	A/mm^2	J_{RB}
3	In end-rings	Air natural	A/mm^2	J_{RE}

Table 4.3: Selection of motor-slots

Selection of stator-rotor slots:		
Sr.No.	Slot-combination	Consequence
1	$N_S = N_R$	Magnetic locking
2	N_S - $N_R = \pm 3P$	Cogging and crawling
3	N_S - $N_R = \pm P, \pm 2P, \pm 5P$	Hooks and cusps
4	N_S - $N_R = \pm 1, \pm 2, (\pm P \pm 1), (\pm P \pm 2)$	Noisy operation

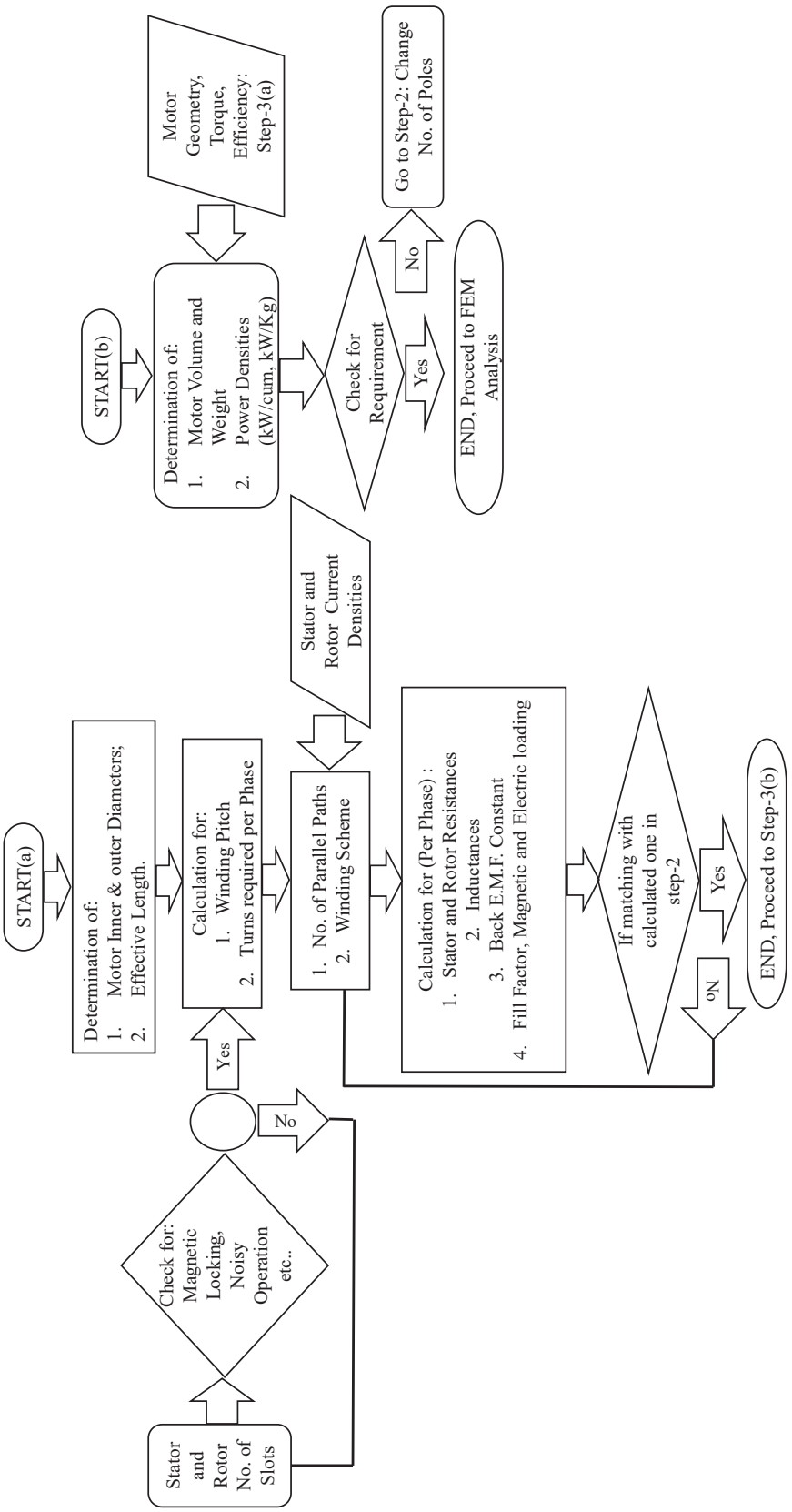

Fig. 4.1: Flowchart showing the design algorithm for obtaining the initial motor design

Table 4.4: Design guidelines

Selection of stator-rotor slots:		
Sr.No.	Parameter	design value
1	Air-gap length	$\leqslant 1mm$
2	Specific magnetic loading	$\leqslant 0.7T$
3	Slot loading	$\leqslant 125A/inch^2$
4	FF	$\leqslant 65\%$
5	Lamination thickness	$\leqslant 0.5mm$
6	Stacking factor	$\geq 95\%$
7	Aspect ratio (Stack length/pole-pitch)	$\leqslant 3$

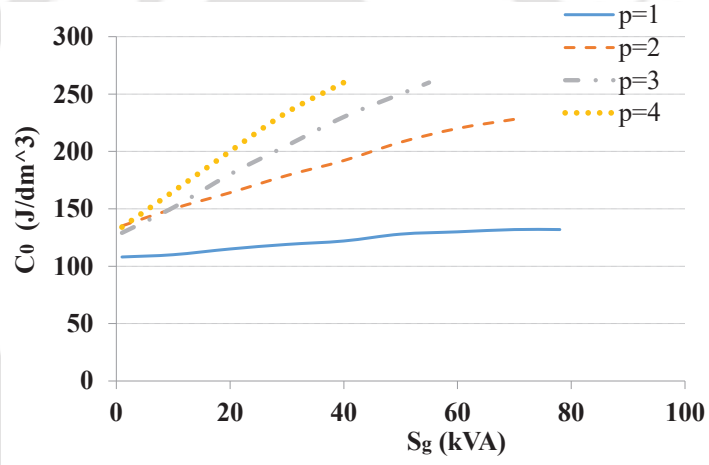

Fig. 4.2: Variation of the output-coefficient (C_0) with apparent airgap power (S_g) and pole-pairs (p) of the motor

4.3 Design of initial motor model

4.3.1 Initial sizing of the motor

There exist two state of the art design concepts to approximate the motor's dimensions (*i.e*, airgap diameter D_g and active stack length L). These two concepts are: a.) output-coefficient based design concept b.) rotor's tangential stress based design concept. The first one starts the motor design with the term $D_g{}^2L$, known as output coefficient (C_0). C_0 , in fact, reflects the volume of the motor and, its value varies with the motor's power rating as shown in Fig. 4.2. Similarly, tangential stress based method begins with tangential stress (σ_t)on the rotor's surface which varies between 0.2-4 Nm/cm^2 based upon the power rating of the motor. This work adopts the output-coefficient based design concept to design the 2.5kW IMs.

4.3.1.1 Stator dimensions

The airgap apparent power (S_g) of the motor is

$$S_g = 3E_{mag}I_S = 3K_E V_{Ph} I_S = K_E \frac{P_{Out}}{\cos\theta_{In}\eta_n} \tag{4.1}$$

where, $K_E = \frac{E_{mag}}{V_{Ph}}$. $\cos\phi_{in}$, η_n, V_{Ph}, I_S are, respectively, the input power factor, efficiency, input phase voltage and phase current at rated operating condition. With the definitions of specific current loading (ac) as

$$ac = \frac{3(2T_{Ph})I_S}{\pi D_{is}} \tag{4.2}$$

and, exploring the expression of E_{mag} as

$$E_{mag} = 2\pi f K_W T_{Ph} \phi_g \tag{4.3}$$

Using the expressions 4.1-4.3,

$$S_g = K_W \pi^2 D_{is}^2 L\, n\, ac B_g = C_0 D_{is}^2 L\, n \tag{4.4}$$

where, C_0 is the output coefficient expressed as $C_0 = K_W \pi^2 ac B_g$.

With the comparison of 4.1 and, 4.4

$$D_{is}^2 L = \frac{1}{nC_0} \frac{K_E P_{Out}}{\cos\theta_{In}\eta_n} \tag{4.5}$$

With introducing the ratio of stack length to pole-pitch ($\lambda = \frac{L}{(\frac{\pi D}{P})}$), which lies between 0.6 to 3,

$$D_{is} = \sqrt[3]{\frac{2p^2 K_E P_{Out}}{\pi\lambda C_0 f \eta_n \cos\theta_{In}}} \tag{4.6}$$

and,

$$L = \left(\frac{\pi D}{P}\right)\lambda = \tau\lambda \tag{4.7}$$

Total height of the stator slot (H_S) is determined from the tooth flux density B_{ts}, ac, B_g, stator current density (J_S) and the fill factor (FF) as

$$H_S = \frac{ac\, B_{ts}}{B_g J_S FF} \tag{4.8}$$

The height of the stator yoke is evaluated such that the flux density in yoke remains half of that in the stator-tooth. With the target value of the yoke flux density of as B_{cs}, the height of stator yoke (H_{CS}) is given as

$$H_{CS} = \frac{\pi D_{is} B_g}{4 p B_{cs}} \tag{4.9}$$

The outer diameter of the motor is hence

$$D_{out} = D_{is} + 2\left(H_{CS} + H_S\right) \tag{4.10}$$

4.3.1.2 Size of stator slots

Previous subsection details the evaluation of stator-slot height. For the determination of rest of the slot-dimensions, at first effective slot area (Acu), which includes the area of copper conductors with insulation, is estimated from the fill-factor (FF) as

$$A_{Cu} = \frac{Z_S \pi d^2}{4FF} \tag{4.11}$$

Slot width at the top (B_{S1}) is determined at first and for this, the width of tooth-bridge W_{tS} is fixed. W_{tS} is chosen using the target value of the tooth flux density B_{tS} and, B_{tS}. With applying the flux balance,

$$W_{tS} = \frac{B_g}{B_{tS}} \frac{\pi D_{is}}{N_S} \tag{4.12}$$

B_{S1} is obtained as

$$B_{S1} = \frac{\pi D_{i+}}{N_S} - W_{tS} \tag{4.13}$$

where, $D_{i+} = D_{is} + 2(H_{0s} + H_{01s})$. H_{0s} and, H_{01s} are the heights of slot opening and slot wedge, respectively. There values lie in the range of 0.5mm to 3mm. Another width of the slot *i.e*, slot height at the bottom (B_{S2}) is calculated by solving the expressions of Acu and, H_S in terms of (B_{S1}) and, (B_{S2}). This results

$$B_{S2} = \left(4 A_{Cu} \tan\left(\frac{\pi}{N_S}\right) + B_{S1}^2\right)^{0.5} \tag{4.14}$$

Opening of the slot (B_{S1}) is kept as 2mm. Its value varied between 2mm to 3mm in all the further design iterations.

4.3.1.3 Airgap length and rotor dimensions

Typical value of the airgap in medoum power IMs lies between 0.35mm to 6mm. The airgap length is a tradeoff between the magnetization current (or no-load power factor), the unbalanced magnetic pull, and manufacturing accuracy. Empirical relation followed for its initial value's (in *mm*) determination are as undermentioned:
The airgap length for a two pole motor-

$$l_g \approx \left(0.1 + 0.02\sqrt[3]{P_{Out}}\right) \tag{4.15}$$

and, for the motors with higher number of pole-pairs-

$$l_g \approx \left(0.1 + 0.012\sqrt[3]{P_{Out}}\right) \tag{4.16}$$

The diameter of the rotor (D_r) is hence,

$$D_r = D_{out} - 2l_g \tag{4.17}$$

4.3.1.4 Stator winding

Double layer, 5/6 short pitched, distributed winding scheme is adopted for these 2.5kW machines to keep the MMF harmonics as well as the copper losses (with the reduction of mean-length of the coil)small. Initial estimation of the number of turns per phase is done following the under-mentioned expressions. For the given values of magnetic flux (airgap) per pole (ϕ_g), winding factor (K_w)and, phase value the of magnetisation voltage (E_{mag}), the turns per phase are

$$E_{mag} = -K_w T_{Ph}\frac{d\phi_g}{dt} \Rightarrow E_{mag}(\omega) = -K_w T_{Ph}\omega\phi_g(\omega) \tag{4.18}$$

For the rated frequency of f,

$$E_{mag}(f) = -2\pi f K_w T_{Ph}\phi_g(f) \tag{4.19}$$

where, ϕ_g is calculated as

$$\phi_g = L \int_0^{\frac{\pi D}{P}} B_g(s).ds = \ < B_g > \frac{\pi D_{is} L}{P} \tag{4.20}$$

where, ds is the incremental displacement along the airgap and, $< B_g >$ denotes the average airgap flux density over a pole-pitch. Total number of conductors (for the three-phase IM) are

$$Z = 3(2T_{Ph}) \tag{4.21}$$

and, this gives conductors per slot equal to Z/N_S. Size of the concoctor is selected such that, the current density remains within prescribed limit (as given in Table 4.2). These numbers are further tuned to match the desired requirement of power factor, efficiency, slot-fill factor, no-load and blocked rotor currents of the motor as shown in Fig. 4.1.

4.3.1.5 Rotor bar and end rings

The rated current in the rotor bar is calculated by applying the MMF balance as (for 3-phase IM)

$$I_{RB} = \frac{6T_{Ph}K_W}{N_R} I_S \tag{4.22}$$

The area of rotor bar is selected that, the current density in the bar remains within prescribed limit (as given in Table 4.2). Similarly, the end-ring current is found with the summation of currents of the bars under one pole as

$$I_{RE} = \frac{0.5}{\sin\left(\frac{\pi p}{N_r}\right)} I_{RB} \tag{4.23}$$

Area of end-ring is chosen to keep its current density in the limit given in Table 4.2. All the rotor slot dimensions are estimated applying the (4.12) to (4.12) with reference to the rotor parameters. The height of the end-ring is estimated such that, the gap between the shaft diameter and the end-ring's inner diameter remains 3mm-6mm. Accordingly, the width of end-ring is calculated using its calculated area.

4.4 Determination of equivalent circuit parameters

T-network equivalent circuit of an induction motor is shown is Fig.3.1. Chapter 2 includes the expressions of three parameters of this circuit out of the total five (with neglecting the core losses). The estimation of the remaining two elements of this circuit is done as

a.) Stator resistance:

$$R_S = \rho \frac{1}{A} T_{Ph} \frac{l_m}{a_{CS}} \chi \tag{4.24}$$

where, A,a_{CS} and,χ denote number of parallel paths, conductor area and, AC resistance factor, respectively.

b.) Rotor resistance:

$$R'_R = \rho \frac{l_B}{a_{BR}} + \rho \frac{l_{ER}}{a_{ER}} \left(\frac{1}{2\sin^2\left(\frac{\pi p}{N_r}\right)} \right) \tag{4.25}$$

where, l_B,$l_E R$,a_{BR} and, a_{ER} are the bar-length,end-ring's length, bar-area and, end-ring's area, respectively. The resistance equivalence of R'_R in the T-network is

$$R_R = R'_R \frac{(2T_{Ph}K_W)^2 N_S}{N_R} \tag{4.26}$$

Temperature corrections of these resistances are done as $R(T_2) = R(T_1)\,(1 + \alpha\,(T_2 - T_1))$. Here, $R(T_2)$, $R(T_1)$ are the resistance values at temperature T_2, T_2 respectively and, α is the temperature coefficent of the resistance.

4.5 Design improvements with revamping geometry for higher efficiency

The geometry parameters obtained from the relations mentioned in section 4.3 are further tuned following the algorithm shown in Fig. 4.1. The tuning of the parameters aims to assure the maximum possible values of efficiency and power factor avoiding the thresholds of current densities, fill-factor and magnetic saturation for the selected materials. Table 4.5 enlists the design specifications of the IM and, Table 4.6 shows the shapes and dimensions of slot-geometries.

Table 4.5: Design Specifications Common To Both 2.5kW Motors

Parameter	Unit	Value	Parameter	Unit	Value
Stator:					
Outer diameter	mm	170	Number of circuits	-	1 x Star
Inner diameter	mm	100	Turn/Coil	number	15
No. of slots		36	Wire size	mm	0.8 mm x 4
Length	mm	80	Coil pitch	slots	8 (88.33%)
Rotor:					
Outer diameter	mm	99	Mean length of turn	mm	192
Inner diameter	mm	30	Turns/phase	number	180
No. of slots		28	Core material	Steel grade	50C350
Windings:					
Type	-	Double layer	Rotor bar material		Copper
Skew	-	Non skewed			
Insulation class	-	F			

Table 4.6: Slot Shapes Of The Two Design Prototypes

Stator slots: ***Initial design***	**SD1**	**Stator slots:** ***Modified design***	**SD-2**
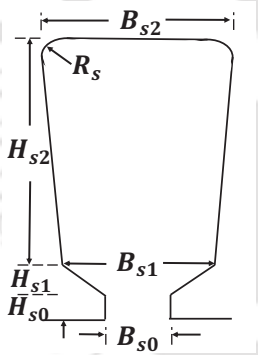	Dim. (mm) B_{s0}=2.4 B_{s1}=6.0 B_{s2}=8.5 R_s=2.75 H_{s0}=1.0 H_{s1}=0.67 H_{s2}=18.33	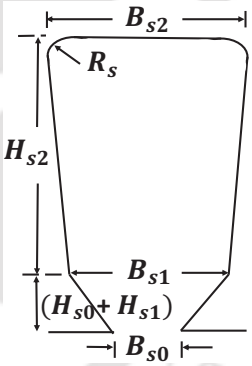	Dim. (mm) B_{s0}=1.5 B_{s1}=6.0 B_{s2}=9.5 R_s=2.5 H_{s0}=0 H_{s1}= 1.67 H_{s2}=18.0
Rotor slots: ***Initial design***	**RD1**	**Rotor slots:** ***Modified design***	**RD-2**
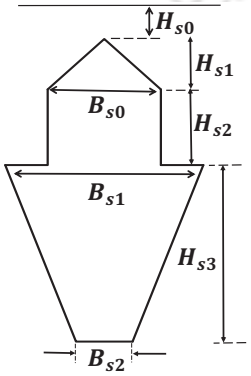	Dim. (mm) B_{s0}=5.5 B_{s1}=6.32 B_{s2}=3.17 H_{s0}=0.3 H_{s1}=1.0 H_{s2}=2.5 H_{s3}=14.0	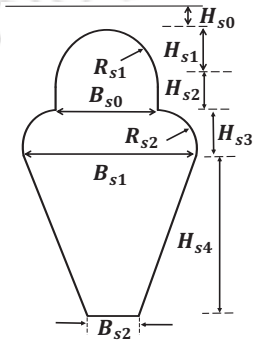	Dim. (mm) B_{s0}=5.0 B_{s1}=6.32 B_{s2}=1.50 H_{s0}=0.3 H_{s1}= 2.25 H_{s2}=1.25 H_{s3}=1.80 H_{s4}= 14.0 R_1=2.4 R_2=3.12

4.6 Motor Design using proposed SL model

This section presents the investigation of the proposed model for its suitability in the design of induction motors with a lower SL. The design of four-pole, 2.5 kW, 200 V IM, as detailed in the previous sections, is considered for this. The stator and rotor slot shapes of the motor are re-designed using the proposed SL model. All the other parameters of the motors *voz*. number of slots (both in stator and rotor), ferromagnetic material, winding scheme, motor diameters, stack-length, air-gap length (given in Table 4.5) are kept as it is. The design steps followed are discussed in the forthcoming subsections in detail.

4.6.1 Design strategy

The discussion in section III showed that the SL, in different models (Table 3.2), is a function of the ratio of L_{ls}/L_m and L_{lr}/L_m. Hence, the design strategy of an IM, for reduced SL, is based on minimization of these ratios without affecting the motor's characteristics. The expressions for these ratios in terms of slot geometries can be written using (3.1), (3.2) and (3.4) as [46]

$$\frac{L_{lS}}{L_m} = \frac{\pi^2 g K_C K_S \left(\lambda_{\mathrm{lg}} + \lambda_{lSS} + \lambda_{lOHS}\right)}{q {K_W}^2 \tau} \tag{4.27}$$

$$\frac{L_{lR}}{L_m} = \frac{\pi^2 g K_C K_S \left(\lambda_{\mathrm{lg}} + \lambda_{lSR} + \lambda_{lOHR}\right)}{q {K_W}^2 \tau} \tag{4.28}$$

The permeances λ_{lg}, λ_{lSS}, λ_{lOHS} of the stator for a two-layer winding are:

$$\lambda_{lSS} = \frac{1}{4}\sum_{k=1}^{5} \lambda_{lSS\_k} \tag{4.29}$$

where

$$\lambda_{lSS\_1} = \frac{H_{s1} + H_{s0}\cos^2\gamma_k}{3B_{s1}}; \lambda_{lSS\_2} = \frac{H_{s2}}{B_{s2}};$$

$$\lambda_{lSS\_3} = \frac{H_{s2}\cos\gamma_k}{B_{s2}}; \lambda_{lSS\_4} = \frac{H_{s2}}{B_{s2}};$$

$$\lambda_{lSS\_5} = (1+\cos\gamma_k)^2\left(\frac{H_{s0}}{B_{s0}} + \frac{H_{s1}}{B_{s1}} + \frac{H_{s2}}{B_{s2}}\right)$$

In the above expressions, γ_k is the phaser displacement between the currents of upper and lower layer of stator winding. If both the layers belong to same phase, $\gamma_k = 0$.

$$\lambda_{\text{lg}} = \frac{5gK_C/B_{s0}}{5 + 4gK_C/B_{s0}} \tag{4.30}$$

$$\lambda_{lOHS} = 0.34\frac{q}{L}\left(l_{es} - 0.64y\right) \tag{4.31}$$

where l_{es} is the length of end-connection and y is the coil pitch. Similarly, the slot permeance for rotor slots of geometry RD1 (in Table 4.6) is:

$$\lambda_{lSR} = \frac{2K_1}{3A}\left[\left(\frac{H_{s1}A_1}{B_{s0}} + \frac{H_{s2}A_2}{B_{s0}} + \frac{3H_{S3}A_3}{B_{s1} + 2B_{s2}}\right)\right]K_2 \tag{4.32}$$

where $K_1 = 1/4 + 3/4K_2$; $K_2 = \frac{1+3\beta}{4}$ and, $\beta = \frac{coil-pitch}{pole-pitch}$. Permeances λ_{lg} and λ_{lOHR} of the rotor are similar to that of the stator as (4.30) and (4.31). Since the winding scheme and geometries other than slot geometries are unchanged during modifications, the objective to reduce L_{lS}/L_m and L_{lR}/L_m in (4.27) can be summarised as reduction of term:

$$F_{obj} = K_C K_S\left(\lambda_{\text{lg}} + \lambda_{lSS}\right) \tag{4.33}$$

The magnitude of F_{obj} can be reduced by:

(i) Reducing B_{s0}: Decreasing B_{s0} to the minimum value constrained by the winding placement, reduces Carter's coefficient K_C, thereby increasing L_m.

(ii) Increasing B_{s2}: Decreasing B_{s0} will, however, increase λ_{lSS} as seen from (4.29). B_{s2} is increased to compensate for the increase in λ_{lSS}, and thus, the overall λ_{lSS} remains unchanged.

(iii) Decreasing H_{s0}: To reduce the λ_{lSS}, without impacting L_m, H_{s0} can be reduced. Here, reducing H_{s0} to zero, while keeping the total slot depth constant, reduces λ_{lSS}.

By doing the above three changes, the stator slot geometry SD1 changes to SD2, as shown in Table 4.6. The overall impact of the changes is that the magnetizing inductance L_m increases, and hence SL reduces. Moreover, the changes done ensure that both the slot geometries, SD1

and SD2, have the same slot area and hence, the same slot fill factor. Similar to the changes made in stator slot geometry, the rotor slot geometry RD1 (Table 4.6) is modified as follows:

(i) All the sharp edges in RD1 are rounded to reduce the flux concentration. A circular arc replaces the triangular shape in the uppermost section of RD1 in RD2.This change reduces the leakage flux at the slot's tip and results in uniform distribution of flux density along the section's height. However, to keep the net leakage flux of this section constant, the width of the section is reduced.

(ii) Adding a segment S3 to RD1 increases the slot width, resulting in lower flux leakage. However, to keep the net slot area same as RD1, the slot bottom width Bs2 is decreased.

The above changes in RD1, result in the new rotor shape RD2 and its permeance function is:

$$\lambda_{lSR} = \frac{1}{4}\sum_{k=1}^{4}\lambda_{lSS\_k} \tag{4.34}$$

where

$$\lambda_{lSR\_1} = \frac{1}{\pi}\ln\left(\frac{1+\left(\frac{H_{s1}}{B_{s0}}\right)^2}{4\frac{H_{s1}}{B_{s0}}}\right)$$

$$\lambda_{lSR\_2} = H_{s2}/B_{s0}$$

$$\lambda_{lSR\_3} = \frac{1}{\pi}\left(\frac{-1+\left(\frac{H_{s3}}{B_{s1}}\right)^2}{\left(\frac{H_{s3}}{B_{s1}}\right)}\right)\ln\left(\frac{-1+\frac{H_{s3}}{B_{s1}}}{1+\frac{H_{s3}}{B_{s1}}}\right)$$

$$\lambda_{lSR\_4} = 2H_{S3}A_3/3(B_{s1}+2B_{s2})$$

The shape RD2 results in lower saturation factor K_S and hence increases L_m. Since the expression of L_m in (3.4) does not explicitly involve the rotor slot geometry; hence, FEA is necessary to understand the extent of the impact the rotor slot shape has on L_m. The next subsection discusses the FEA of the motor geometries.

4.6.2 FEM Simulation

This subsection presents the FEA of all the four motor types. The FEA models are run at synchronous speed to simulate the no-load (NL) condition to accurately evaluate the L_m, and verify the impact of the slot geometry on L_m. Fig. 4.4 shows the results of FEA, and it can be seen that the no-load current(I_{NL}) for M3 is least, and it is 14.67% less in comparison to M1

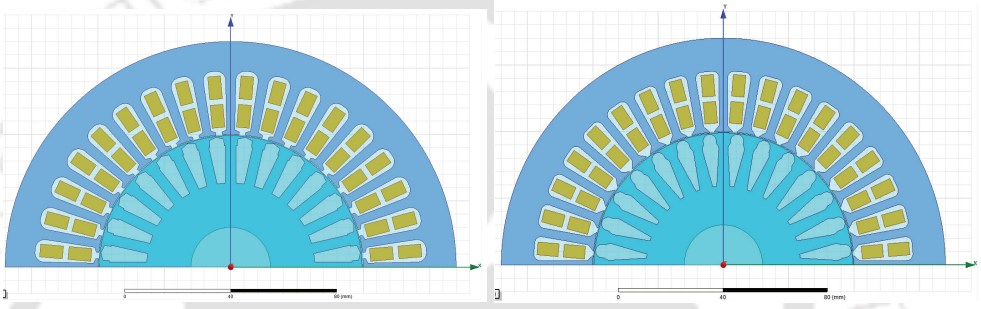

(a) Design-1 **(b)** Design-2

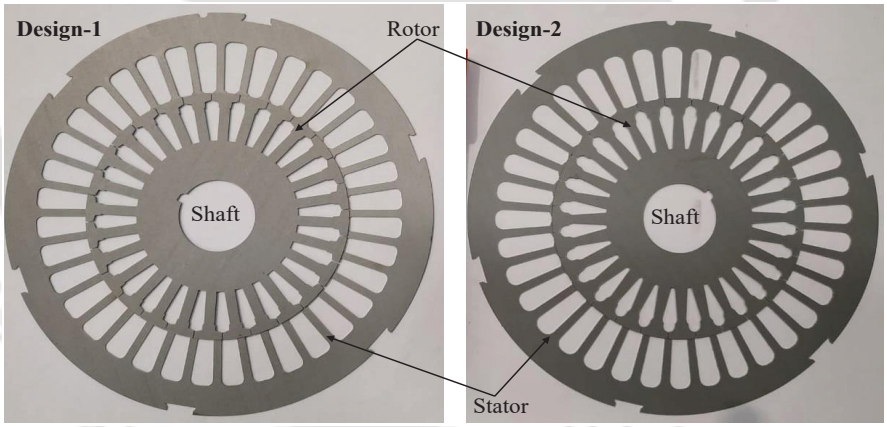

(c) Laminations of Design-1 and Design-2

Fig. 4.3: 4 Pole, 2.5 kW motor designs- *Design-1: standard-design motor (initial design); Design-2:motor with modified slot geometry (modified design); Photographs of the laminations of Design-1 and Design-2.*

(from 5.45 A in M1 to 4.65 A in M3). Moreover, the stator and rotor tooth flux density (Fig. 4.4e), for one rotation of the rotor, shows least harmonic content for motor M3. Furthermore, the performance parameters of all the four motors are evaluated using FEA and are listed in Table 4.8. The results in Table 4.8 show that all the motors have almost the same operating parameters, but M3 has the smallest L_{lS}/L_m and L_{lR}/L_m ratio.

Table 4.7: 2.5kW Motor Variants

Prototype	M1	M2	M3	M4
Stator-Rotor	SD1-RD1	SD2-RD1	SD2-RD2	SD1-RD2

The analysis given in this subsection, confirm that the motor M3 has the highest L_m and hence, should have the least SL. In the next section, it eventually will be shown that M3 indeed has the least SL.

Table 4.8: Specifications Of The Prototype Motors

Sr.No.	Parameter	M1	M2	M3	M4
1	$I_S(A)$	10.39	10.28	10.14	10.13
2	$T_{Rtd.}(Nm)$	17.65	17.65	17.64	17.73
3	pf	0.83	0.84	0.85	0.85
4	$P_{In}(W)$	2989.65	2984.25	2977.54	2990.64
5	$P_{CuP}(W)$	216.68	211.93	206.65	206.00
6	$P_{CuS}(W)$	64.70	64.69	64.65	64.97
7	$P_{Out}(W)$	2708.27	2707.63	2706.24	2719.67
8	rpm	1465.00	1465.00	1465.00	1465.00
9.	$T_{Start}(Nm)$	20.62	24.17	26.97	22.75
10	$T_{Max}(Nm)$	40.99	42.94	44.37	42.08
11	$L_{lS}(mH)$	3.06	3.13	3.19	3.08
12	$L_{lR}(mH)$	5.00	4.95	4.89	4.80
13	$L_m(mH)$	78.87	83.23	87.60	82.02
14	L_{lS}/L_m	0.039	0.038	0.036	0.038
15	L_{lR}/L_m	0.063	0.059	0.056	0.059

4.7 Experimental results with prototyped motors

The previous section discussed the design of IM for lower SL, and out of the four motors, M3 was predicted to have the least SL. To verify the conclusions, both the stators SD1 and SD2, and the rotors RD1 and RD2, were prototyped and tested. This section discusses the test

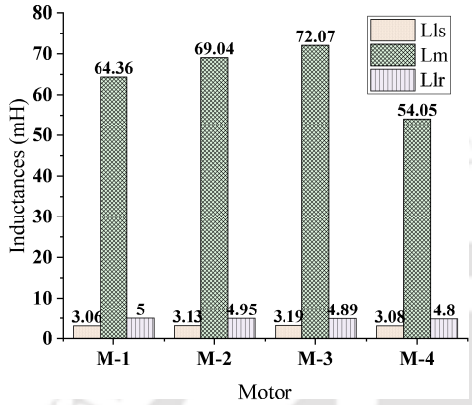

(a) Various motor inductances

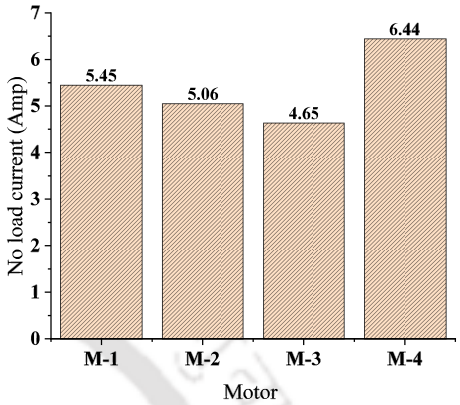

(b) No-load currents (I_{NL})

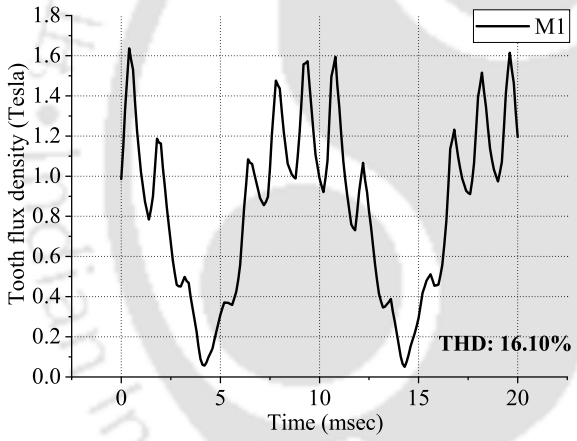

(c) Tooth flux density (B_t) in M1

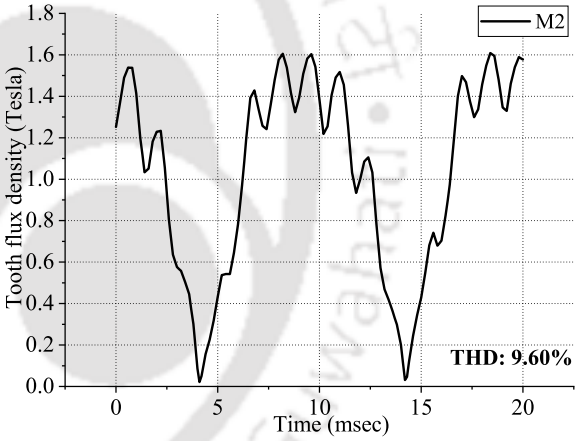

(d) Tooth flux density (B_t) in M2

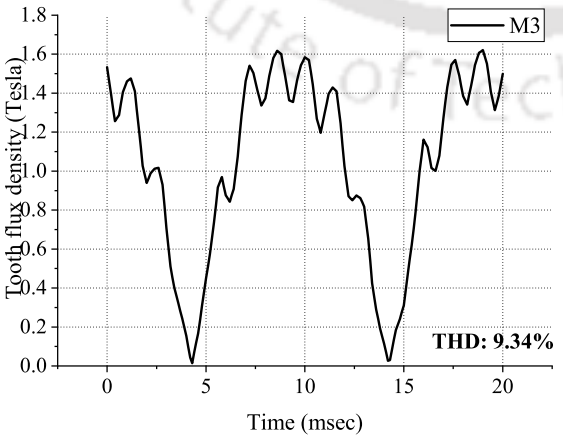

(e) Tooth flux density (B_t) in M3

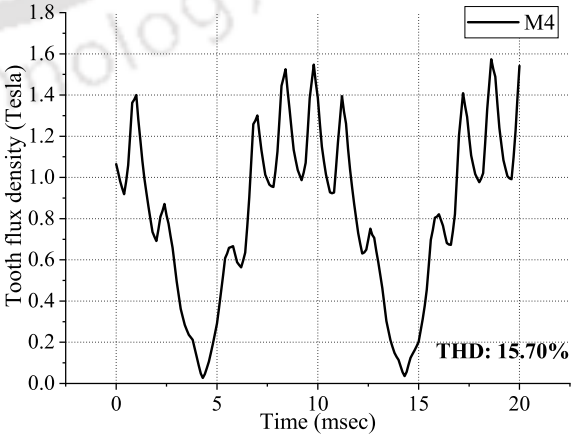

(f) Tooth flux density (B_t) in M4

Fig. 4.4: FEM results: *for four design variants obtained from the two stator and two rotor designs*

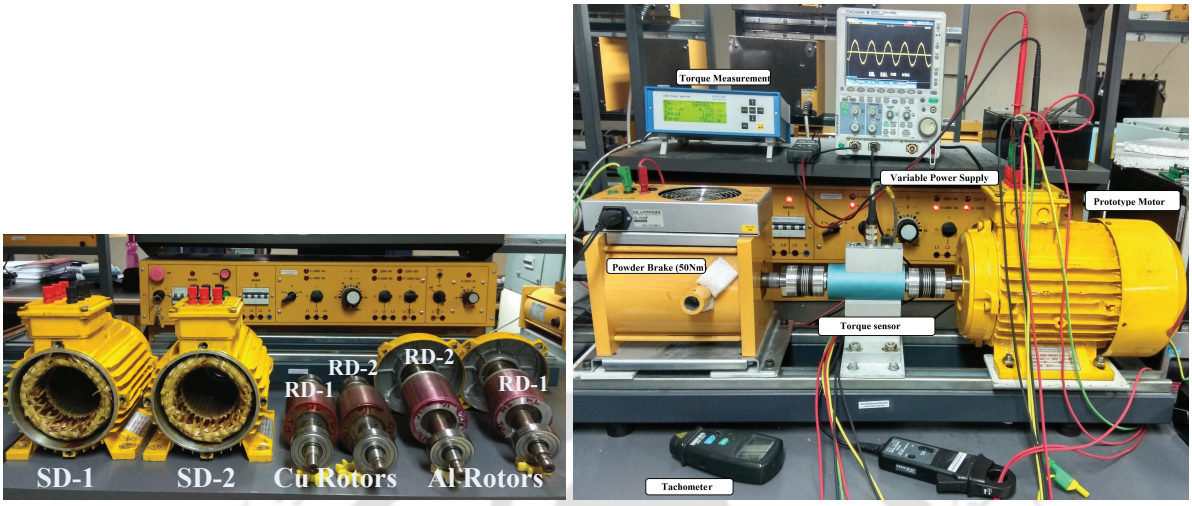

(a) Motor Prototypes **(b)** Load test setup

Fig. 4.5: Photographs of the 4 pole, 2.5 kW motor prototypes and load test setup

procedure and the measurement results. The tests done on the motors are: a). No-load and blocked rotor (NLBR) tests- for evaluation of ECPs, b). Eh-star test- for SL measurement. The following subsections describe the test procedure and discuss the results.

4.7.1 Tests On motor-prototypes

1). No-load and blocked rotor tests: Results obtained from NLBR tests are given in Table 4.9. The windage and friction losses are determined here by extending the $Voltage^2$ versus input power minus joule losses curve to zero value of $Voltage^2$ [9] and no-load core loss (P_{Core}) is calculated as:

$$P_{Core} = P_{in\_NL} - P_W - R_S(T) \sum_{i=1}^{3} I_i^2$$

where, P_{in_NL} is the input power to the motor in no-load condition, P_W is windage and friction losses, $R_S(T)$ denotes temperature-corrected per phase resistance of the stator winding and I_i is the rms value of stator current of i phase. The ECPs evaluated from the NLBR test data are shown in Table 4.10, and the results show that the motor M3 has the highest value of L_m, as well as the smallest values of L_{lS}/L_m and L_{lR}/L_m.

2). Eh-star test: The SL, for all four motors, was measured using Eh-star test, following the procedure given in [9]. The reason for choosing the Eh-star test is that it does not need mechanical coupling or any dynamometer, and hence easy to implement with minimum numbers

Table 4.9: No-Load And Blocked Rotor Test Results

Motor	I_{NL} (A)	W_{NL} $-P_{CuP}(W)$	P_W (W)	P_{Core} (W)	V_{BL} (V)	I_{BL} (A)
M1	4.84	58.25	20.44	37.81	38.14	11.24
M2	4.36	59.17	21.15	38.02	37.59	11.28
M3	4.20	55.00	20.59	34.41	36.41	11.12
M4	4.42	59.25	22.25	37.00	38.72	11.98

Table 4.10: ECPs Calculated With NLBR Test Data

Sr.No.	ECP	M1	M2	M3	M4
1	$R_S(\Omega)$	0.90	0.90	0.90	0.90
2	$L_{lS}(mH)$	3.70	3.53	3.53	3.52
3	$R_R(\Omega)$	0.32	0.33	0.33	0.32
4	$L_{lR}(mH)$	6.49	6.26	6.19	6.17
5	$L_m(mH)$	77.67	80.52	84.15	79.40
6	L_{lS}/L_m	0.048	0.044	0.042	0.044
7	L_{lR}/L_m	0.084	0.078	0.074	0.078

of equipment [56]. Moreover, this test has higher precision, and the accuracy of the Eh-star test is higher in comparison to the reverse rotation test [56]. The results of the test have a reasonable correlation with the input-output test in compliance with IEC 60034-2-1 [56]. The SL value, using Eh-star test, is given by:

$$SL = k[(1-s)(P_+ - P_-) - P_W - P_{Core}$$

where $k = 1/1 + \left(\frac{I_+}{I_-}\right)^2$. Measurements were recorded for 6 test points and it is ensured that I_+ remains less than one third of I_-. The measured values of SL are shown in Table 4.11. Plots between SL and $(I_-/I_t)^2$ for all four prototypes are shown in Fig.4.6. The slopes of these plots give SL at rated operating conditions. The maximum and minimum SL values are 35.9 W and 25.87 W, which correspond to the motors M1 and M3, respectively.

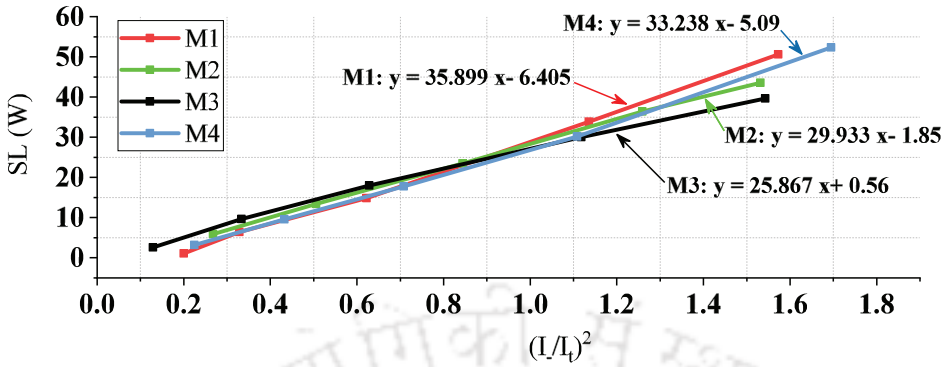

Fig. 4.6: Eh-star test results obtained for different motor prototypes

4.7.2 Comparison of SL with different relations

SL values are calculated for all the motor prototypes with the proposed model F6 (modified for pole pairs) and compared with measured SL along with the SL calculated using four other stage-of-the-art relations mentioned in the literature, and the values are shown in Table 4.11.

Table 4.11: SL For 2.5kW Motor Prototypes(In watt)

Motor	Measured	F6	IEEE 112	IEC 60034-2-1	Pillay *et.al*	Agamloh *et.al.*
M1	35.90	27.85	45.00	57.53	31.98	34.88
M2	29.93	25.13	45.00	57.53	31.98	34.88
M3	25.87	23.66	45.00	57.53	31.98	34.88
M4	33.24	25.39	45.00	57.53	31.98	34.88

A careful investigation of the SL data shown in Table 4.11, reveals that:

- Measured SL is maximum for M1 and minimum for M3, with respective SL values equal to 1.44% and 1.03% of the rated output power. Hence, the slot geometry plays a significant role in reducing SL.
- Measurements show different SL values for all the four prototypes, and the relations reported so far in the literature (Columns 4 to 7 of Table 4.11) give a constant value for all the four motors.
- The proposed model F6 gives different SL values for all these motors. The value of SL, predicted using F-6, is highest for M1 and lowest for M3, which is in line with measurements.

5

Stray loss in Inverter fed Motors

Contents

5.1 Introduction

The time harmonics of the inverter power supply result in a higher rate of change in magnetic field densities at different segments of the iron core. As a consequence, both the SL and CL get increased by an inverter power supply. Compared to a sinusoidally excited motor with the same fundamental frequency, the CL in an inverter fed IM has risen to 35% [57], [58]. Furthermore, applications such as electric traction demand a wide range of field weakening (high-frequency operation), which elevates the CL proportion even more. The impact of time harmonics depends upon the ratio of fundamental to the switching frequency [59]. This ratio varies from 20 (medium power application) to 200 (small power applications) in the majority of inverter fed IM-drives [60, 61].

However, when addressing the SL, literature is broadly restricted to the space harmonics, and sinusoidal excitation [22, 46, 47]. [46] and [47], present theoretical expressions to estimate the SL in a grid-connected IM. These expressions are rather complex, require the motor's complete geometry details, and need modifications as the slots' geometry changes. In a lumped element-based approach, Alger et al. present an extended equivalent circuit of IM to include the impact of harmonics [47]. Direct and exact evaluation of these coupled lumped parameters is strenuous. As discussed in Chapter 1, a precise model representation of the SL accelerates the iterative motor design process. It requires less response time when incorporated in motor control than the purely physics-based methods. This chapter illustrates the adaptation of the proposed SL model (detailed in chapter 3) for an inverter driven environment.

5.2 Background: Stray losses in inverter fed IM

Primary sources of SL in an IM are the various leakage fluxes, space and, time harmonics of the magnetic flux density ($B(t)$). These space and time harmonics of $B(t)$ are traced to the variation of magnetomotive force MMF. This section describes the space and harmonics in an inverter fed IM and their correlation with SL.

5.2.1 Space harmonics with sinusoidal excitation

Fourier decomposition of the magnetomotive force (MMF) generated by a distributed winding of one-phase (in a three-phase machine) is given as [47]:

$$F_A(\theta, t) = \frac{2}{\pi} N_S i(t) \sum_{v=1}^{n} \frac{K_W(v)}{v} \sin(vp\theta) \tag{5.1}$$

where,

$$i(t) = I_m \sin(\omega t) \tag{5.2}$$

, $K_W(v)$ is the winding factor of the v-th space harmonic. N_S and, p are, respectively, per phase number of turns in stator winding and, pole-pairs. For a three-phase machine drawing a balanced set of currents, the net MMF is given as the sum of MMFs of all the three phases, which are 120 shifted in space and it is:

$$F_S(\theta, t) = F_A(\theta, t) + F_B(\theta, t) + F_C(\theta, t) \tag{5.3}$$

Using (1) and (2), the net MMF is given as:

$$F_S(\theta, t) = \frac{3}{2} \left[\begin{array}{l} A_1 cos(\omega t - \theta) - \frac{A_5}{5} cos(\omega t + 5\theta) + \\ \frac{A_7}{7} cos(\omega t - 7\theta) ..... \end{array} \right] \tag{5.4}$$

where,

$$A_v = \frac{2}{\pi} N_S I_m . K_W(v) \tag{5.5}$$

Expression (5.4) represents multiple travelling waves rotating in different directions. All these MMF harmonic waves travel with a speed less than the synchronous speed i.e., the speed of the fundamental MMF-wave.The MMF waves corresponding to space harmonic numbers $v = 6k-1$ rotate in the reverse direction of the MMF wave of fundamental whereas, the MMF waves with harmonic number $6k+1$ rotate in the direction of fundamental MMF wave. The space harmonics of order higher than 7 are negligible [49] and hence are neglected.

5.2.2 Space harmonics with inverter fed excitation

For an inverter-fed IM, the motor currents are expressed as:

$$i_a(t) = \sum_{n=1}^{h} I_m(n) \sin(n\omega t + \phi(n)) \tag{5.6}$$

$$i_b(t) = \sum_{n=1}^{h} I_m(n) \sin(n\omega t + \phi(n) - \frac{2\pi}{3}) \tag{5.7}$$

$$i_c(t) = \sum_{n=1}^{h} I_m(n) \sin(n\omega t + \phi(n) + \frac{2\pi}{3}) \tag{5.8}$$

Evaluation of (5.1)-(5.3) for the MMF in relation to the current expressions (5.6)-(5.8) gives:

$$F_S(\theta, t) = F_1(\theta, t) + F_5(\theta, t) + F_7(\theta, t) + ... \tag{5.9}$$

where,

$$F_1(\theta, t) = \sum_{v=1}^{n} A_v cos(v\omega t - p\theta) \tag{5.10}$$

$$F_5(\theta, t) = \sum_{v=1}^{n} A_v cos(v\omega t + 5p\theta) \tag{5.11}$$

$$F_7(\theta, t) = \sum_{v=1}^{n} A_v cos(v\omega t - 7p\theta) \tag{5.12}$$

From expressions (5.10)-(5.12), it is seen that the harmonics in current superimpose various high-frequency waves to the MMF waves corresponding to the fundamental frequency. All these rotating MMF waves produce additional SL.

5.2.3 Correlation of SL with the inverter power supply

The major components of SL *viz.* surface core loss, tooth flux pulsation loss and, phase belt pulsation loss are the additional eddy current losses in reaction to the space harmonics of the $B(t)$. The expressions of these losses derived using the diffusion equation and Faraday's law show that these losses vary directly as the square of MMF [46, 49]. Hence, SL in a cumulative

effect of all the MMF harmonics for an inverter fed motor can be expressed as:

$$SL = \sum_{i=1}^{n} SL(i) = \sum_{i=1}^{n} K_i F_i^2 \tag{5.13}$$

$$\Rightarrow SL = K_1 F_1^2 \left(1 + k_2 \left(\frac{F_2}{F_1}\right)^2 + k_3 \left(\frac{F_3}{F_1}\right)^2 + ...\right) \tag{5.14}$$

where, $SL(i)$ is the net SL with i-th time-harmonic and all the space harmonics. F_i is the magnitude of the MMF corresponding to the i-th current harmonic (as shown by (7)-(9)). K_i is the proportional coefficient of the SL-MMF relation. With a linear relation of MMF with current, the series sum used in (5.14) is directly proportional to the total harmonic distortion (THD) in the motor-current (a directly measurable quantity), and hence the SL in an inverter fed motor can be written as

$$SL = K_1 F_1^2 f(THD) \tag{5.15}$$

where, $f(THD)$ is a single valued monotonic function of motor's current THD. The determination of this function is explained in section-IV, which uses the experimental results of SL. The test procedure and the experimental results are detailed in the next section, i.e. section-III.

5.3 Experimental Estimation of SL

Total six squirrel cage induction motors of different slot geometries are selected to record the variation of SL with inverter power supply. Among these six motors, four motors are of same power ratings but different slot-geometries whereas, the other two motors are of another power ratings which differ only in terms of lamination thickness. Nameplate details of these motors are given in Table 5.1 and, Table 5.3 shows their slot geometries. As the literature report, two prominent sources of the SL *i.e.*, tooth-saturation and permeance variation are very specific to the slot shape. The major limitations of existing analytical SL methods [46, 47, 51] is that, they use conformal transformation for the airgap flux density distribution (to determine the arigap conductance harmonics) assuming that the slots are infinitely long and possess uniform width (equal to slot-opening B_{S0}). As a consequence, the airgap conductance harmonics' calculations

in [46,47,51] use only two dimensions of a slot (*i.e.*, slot-opening and tooth width), it is therefore not possible with these expressions to differentiate two IMs of same number of slots but different slot geometries (except the slot-opening) for SL. The purpose of selection of four similar motors is, hence, to examine the SL variation among the IMs of the same power rating and, pole pairs but different slot geometries.

Table 5.1: Specifications of Tested IMs

Motor	P_{Out}	Design		Speed	Cage bar	Volt.	Slots	Lamination
	kW	Stator	Rotor	(rpm)	material	/f	N_S-N_r	thickness
M-1	2.5	SD-1	RD-1	1482	Copper	200/50	36-28	0.5mm
M-2	2.5	SD-2	RD-1	1482	Copper	200/50	36-28	0.5mm
M-3	2.5	SD-2	RD-2	1482	Copper	200/50	36-28	0.5mm
M-4	2.5	SD-1	RD-2	1482	Copper	200/50	36-28	0.5mm
M-5	1.5	SD-3	RD-3	2889	Aluminium	415/50	36-34	0.5mm
M-6	1.5	SD-3	RD-3	2889	Aluminium	415/50	36-34	0.3mm

5.3.1 Test operating points

The ratio of switching frequency to the fundamental frequency varies highly among the various applications (from 10 to 200). Therefore, the IMs selected in this work (as shown Table 5.1) are tested for a wide range of this ratio. Another important parameter affecting the SL is the fundamental frequency and loading of the motor. The SL measurements are performed to analyse all these parameters' impact on all the operating points as given in Table 5.2.

Table 5.2: IMs Operation Domain

	f_0 (Hz)	Torque (Nm)	f_0/f_{sw} Ratio
Minimum	30	0	10
Maximum	60	14	200
Steps	4	5	5

5.3.2 Measurement procedure

SL for these four IMs is evaluated using the input-output test. The test is reported to be the most accurate among all the SL evaluation methods [56]. Since the power ratings of the IMs are

Table 5.3: Slot Shapes Of The Two Design Prototypes

Stator slots:	**SD1**	**Stator slots:**	**SD-2**
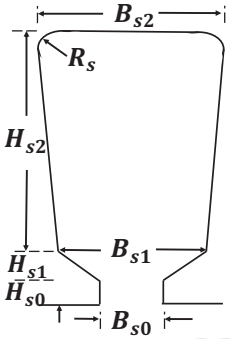	Dim. (mm) B_{s0}=2.4 B_{s1}=6.0 B_{s2}=8.5 R_s=2.75 H_{s0}=1.0 H_{s1}=0.67 H_{s2}=18.33	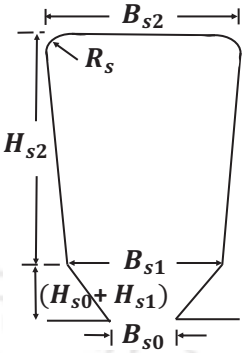	Dim. (mm) B_{s0}=1.5 B_{s1}=6.0 B_{s2}=9.5 R_s=2.5 H_{s0}=0 H_{s1}= 1.67 H_{s2}=18.0
Rotor slots:	**RD1**	**Rotor slots:**	**RD-2**
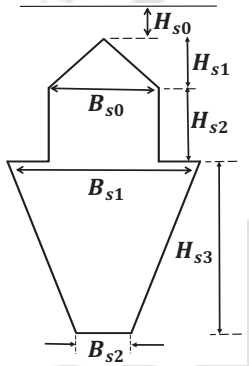	Dim. (mm) B_{s01}=0 B_{s0}=5.5 B_{s1}=6.32 B_{s2}=3.17 H_{s0}=0.3 H_{s1}=1.0 H_{s2}=2.5 H_{s3}=14.0	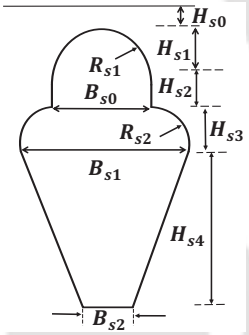	Dim. (mm) B_{s01}=0 B_{s0}=5.0 B_{s1}=6.32 B_{s2}=1.50 H_{s0}=0.3 H_{s1}= 2.25 H_{s2}=1.25 H_{s3}=1.80 H_{s4}= 14.0 R_1=2.4 R_2=3.12
Stator slots:	**SD3**	**Rotor slots:**	**RD-3**
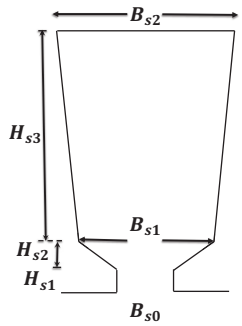	Dim. (mm) B_{s0}=2.0 B_{s1}=8.0 B_{s2}=10.0 H_{s1}=1.0 H_{s2}=0.9 H_{s3}=8.6	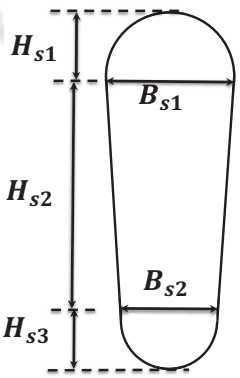	Dim. (mm) B_{s1}=3.65 B_{s2}=1.22 H_{s1}= 3.0 H_{s2}=10.12 H_{s3}=2.80

not very high and they can be loaded upto their rated power, the input-output test is preferred. If the IM is inverter fed, all the CL and SL related tests require two sets of measurements- a)- load and no-load test with PWM power supply b)-load and no-load tests with sinusoidal excitation. These tests are performed as follows:

5.3.2.1 Rated load test

The test IM is coupled with magnetic power brake as load and loaded for different torque values as shown in Table 5.2. Voltages, currents and shaft torque are recorded at the thermal equilibrium.

5.3.2.2 No-load test

The no-load (NL) test is performed with the hot motor after the load test. The friction and windage losses and core loss are obtained from the no-load test at different supply voltages with sinusoidal power supply. Fig. 5.2 (a)-(b) show the NL-test results. Detailed step-wise procedure for these test in line with IEC-60034-3-2 is discussed in [62], [63]. Given the fact that, SL-estimation is highly sensitive to the torque and current measurements [64], the equipments used are selected in compliance with IEEE 112-B (*i.e*, 0.2% accuracy for voltage and current measurements and, 0.5% accuracy for toque and speed measurements).

The measurement set-up for these test (as shown in Fig.5.1 comprises: a).torque sensor (Kistler 4503B) and CoMo Torque Type 4700 data acquisition system. b) 2-level, H-bridge three-phase inverter c). 1.5 kW IM motor prototype d). Digital oscilloscope: YOKOGAWA DLM2054 with voltage and current probes e). Voltage and current transducers: LEM sensors LV25-P and LA 15P f). dSpace DS1103 for data acquisition g).Photo-tachometer. SL from these test data is obtained as difference of CL between the loaded and no-load conditions of the IM [14], [51] *i.e*.,

$$SL = P_{Core\_L} - P_{Core\_NL} \tag{5.16}$$

where, P_{Core_L} and, P_{Core_NL} are, respectively, the CL at loaded and no-load conditions for the same voltage,f and f_{sw}. The CL, here, is calculated using the cycle-averaged value of input power (P_{In}) and then, applying the input-output power balance as:

$$P_{Core} = P_{In} - P_{CuS} - P_{CuR} - P_{Out} \tag{5.17}$$

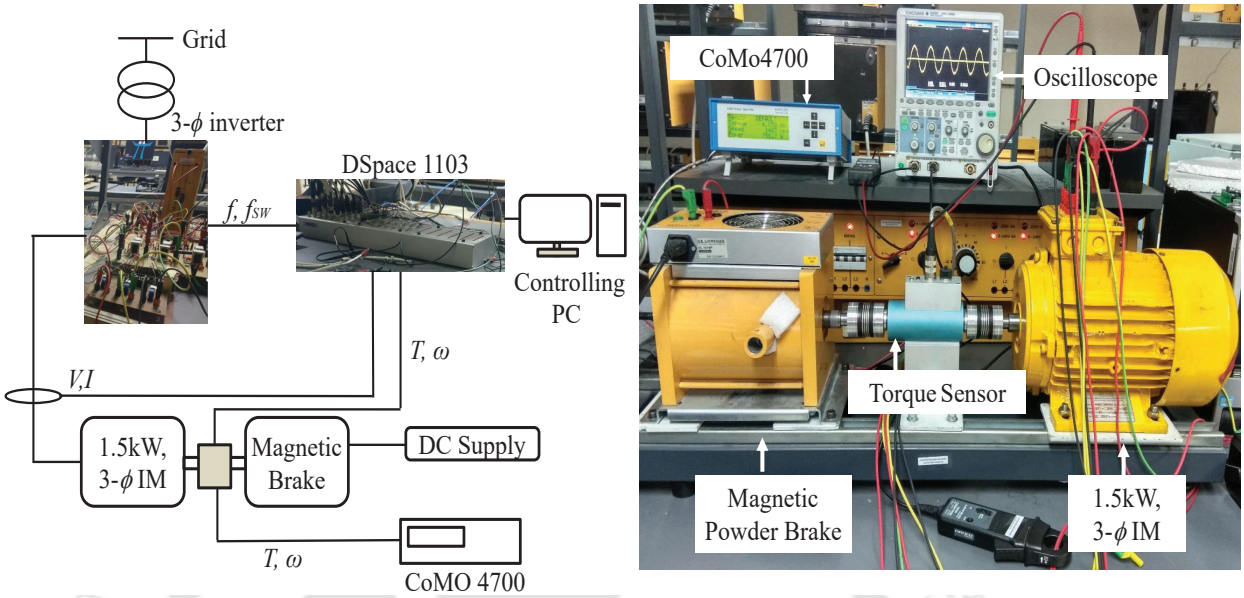

Fig. 5.1: Experimental setup: Schematic and test-bench

where, P_{CuS} and, P_{CuR} are the stator and, rotor copper losses, respectively, determined using the frequency and temperature dependant values of stator and rotor resistances (*i.e.*, $R_S(T, f_i)$, $R_R(T, f_i)$) and stator-current harmonics I_i as

$$P_{CuS} = 3\sum_{i=1}^{100} I_i^2 R_S(T, f_i) \tag{5.18}$$

,

$$P_{CuR} = 3R_R(T, f){I_{R1}}^2 + 3\sum_{i=2}^{100} R_R(T, f_i)\left(I_i \frac{X_{mi}}{X_{lRi} + X_{mi}}\right)^2 \tag{5.19}$$

here, X_{mi} and, X_{lRi} are the magnetising and rotor-leakage reactances *w.r.t.* *i*-th harmonic,

$$P_{Out} = P_{Shaft} + P_{Windage} + P_{Bearing} \tag{5.20}$$

and,

$$P_{Shaft} = T_{Shaft}\omega_r \tag{5.21}$$

T_{Shaft} and ω_r are the measured values of shaft torque and rotor speed in rad/s respectively. To reduce the measurement discrepancy, the obtained SL test data is smoothened (for correlation coefficient, $R^2 > 0.95$) by applying linear regression analysis with squared value of the torque. The process needs repeated measurements. The SL for the rated operating point is then

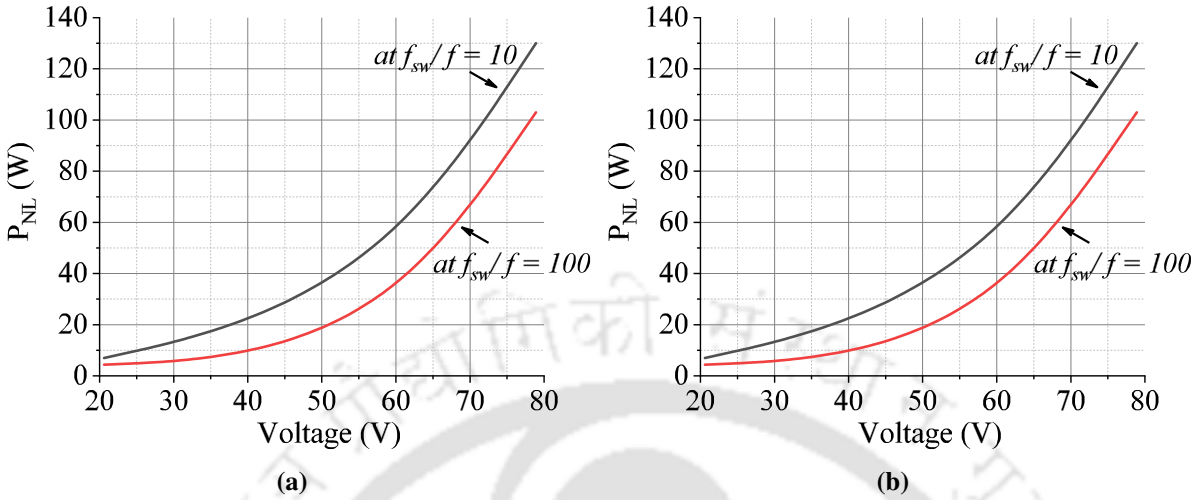

Fig. 5.2: No-load test results for at(a) M1, (b) M2.

calculated by multiplying the slope of the plot with rated torque. Fig. 5.3 and Fig. 5.4 ((a)-(e)) show the SL values of M1 and M2 plotted against the fundamental and switching frequency for different torque values (operating points of Table 5.2). Similarly, Fig. 5.5 show the measured SL values for M3 and, M4. Examination and comparison of these results for different IMs draw following observations:

- As can be seen, the SL of the M1 is always the highest value and lowest for M3 in all the experiments. SL values for M2 and M4 always lie between the same of M1 and M3. For example, at the rated torque at 30Hz frequency with 300Hz switchings, they amount to 62.18W, 57.83 W, 48.30 W, and 52.25W for M1, M2, M3 and M4, respectively.
- SL notably increases with frequency. As Fig. 5.3(f) shows, the order of variation of SL with frequency is greater than one.
- The impact of carrier frequency on SL is quite prominent as expected. Low switching frequency (f_{sw}) operation makes the motor current highly distorted and consequently, raise the net SL. As shown in Fig. 5.3 and Fig. 5.4 ((a)-(e)) (a)-(d), the impact of f_{sw} shows a rapid decrement in the f_{sw}/f range of [10,50]. For very high f_{sw}/f (i.e. 100-200), SL with inverter fed IM is almost equal to that of a sinusoidally excited IM.

5.4 Proposed SL formulation

This section presents the development of the SL model for inverter fed IM using the measured values of SL. The exact analytical formulation of the SL is not possible [18] due to non-linear behaviour of magnetic core, dependence of iron-loss coefficients on magnetisation and frequency, impact of magnetic field distribution on current density distribution within the conductors (proximity and skin effect) and, the impact of slot-tapering on flux pulsation. Development of an empirical model is, hence, the most suitable option to account quantitatively the SL. [65] presents an empirical SL model for grid-connected IMs, which includes the impact of motor geometry on SL as well. The model in [65] uses motor inductances, the number of pole pairs and, output power as input variables. However, this model is developed neglecting the impact of power supply harmonics, which limits its application to the grid connected IMs. When modified to use inverter fed IM, the model will need to incorporate the following additional variables: THD, f_{sw} (or f_{sw}/f).

5.4.1 SL Model structure

In case of inverter fed IM, the variation in SL is associated with the changes in three power supply parameters: 1.) Output power (P_{out}), 2.) Supply frequency (f) and, 3.) f/f_{sw} ratio (τ) or current THD in motor current.

Incremental change in SL,corresponding to the changes in above three parameters is:

$$dSL = \frac{\partial SL}{\partial P_{Out}} dP_{Out} + \frac{\partial SL}{\partial f} df + \frac{\partial SL}{\partial \tau} d\tau \tag{5.22}$$

Since, the three variables (P_{out}),f and,τ) are mutually exclusive, the variation (5.22) can be expressed as:

$$SL = f_1(P_{Out}) f_2(f) f_3(\tau) \tag{5.23}$$

Here, variation of SL with P_{Out} (i.e. $f_1(P_{out})$ in (5.22)) is recognised as reported in [65] *i.e.*,

$$f_1(P_{Out}) = K_{SL} P_{Out} = \left(\frac{1}{p}\frac{L_{lS}}{L_m}\right)^m \left(\frac{1}{p}\frac{L_{lR}}{L_m}\right)^n P_{Out} \tag{5.24}$$

where, p is number of pole-pairs and, L_m,L_{lS} ,L_{lR} are the magnetising inductance, stator leakage

inductance and rotor leakage inductance, respectively (as shown in Fig.3.1). Formulation of $f_2(f)$ and, $f_3(\tau)$ uses following measurement observations:

5.4.1.1 Impact of frequency (for $f_2(f)$)

As shown in Fig. 5.3(f), SL increases with the fundamental frequency for constant f_{sw} and, load torque (T_L). With two trend related observations that, the rate of increment of SL with f is higher than one and, SL is zero at zero f, the simplest form of is given as:

$$f_2(f) = \alpha\left(\frac{f}{f_r}\right)^{\beta} \tag{5.25}$$

where, α and β are the constants and f_r is rated frequency i.e. supply frequency for rated speed, rated torque.

5.4.1.2 Impact of THD in motor-current (for $f_3(\tau)$)

Fig. 5.3 and Fig. 5.4 show the measured values of current THD and SL for different switching frequency-ratio. Here it is evident that SL decreases monotonously with increment in f_{sw}/f ratio following the grid SL value asymptotically. Also,the rate of change of SL with f_{sw}/f depends upon the f_{sw}/f. This rate decreases as the ratio f_{sw}/f increases i.e. the impact of switching frequency variation is high at low switching frequency. Hence, the fractional change in SL (due to change in τ only) shows a decreasing trend with τ i.e.,

$$\frac{df_3(\tau)}{f_3(\tau)} = \frac{d\tau}{(a + b\tau)} \tag{5.26}$$

Solving (5.26) provides the general solution as:

$$f_3(\tau) = \frac{k}{(a + b\tau)^r} + C \tag{5.27}$$

where, a, b, r, k and, C are the equation constants. The expression (5.27) relates SL (analogously the current THD) variation with f/f_{sw} for constant T_L. However, the current THD decreases as the T_L is increased (Fig. 5.3(e) and Fig. 5.4(e))). This is because only the fundamental current increases when T_L is increased. The rotor resistance to slip ratio for higher order harmonic currents observe negligible change due to higher value of their synchronous speed and thus, the change in harmonic current with T_L (or slip) is very small. To incorporate this, $f_3(\tau)$ is

further multiplied with a factor $(I/I_0)^2$. Here, I_0 is the no-load current at the same f_{sw}.The final expression of SL with the $f_2(f)$ and $f_3(\tau)$ is

$$SL = \underbrace{\left(\left(\frac{1}{p}\frac{L_{lS}}{L_m}\right)^m\left(\frac{1}{p}\frac{L_{lR}}{L_m}\right)^n P_{Out}\right)}_{f_1(P_{Out})}\underbrace{\left(\alpha\left(\frac{f}{f_r}\right)^\beta\right)}_{f_2(f)}\underbrace{\left(\frac{I}{I_0}\right)^2\left(C+\frac{k}{(a+b\tau)^r}\right)}_{f_3(\tau)} \tag{5.28}$$

The expression (5.28)is summarised as

$$SL = K_{Grid}K_{Inv}P_{Out} \tag{5.29}$$

where,

$$K_{Grid} = \left(\left(\frac{1}{p}\frac{L_{lS}}{L_m}\right)^m\left(\frac{1}{p}\frac{L_{lR}}{L_m}\right)^n\right) \tag{5.30}$$

and,

$$K_{Inv} = \left(\alpha\left(\frac{f}{f_r}\right)^\beta\right)\left(\frac{I}{I_0}\right)^2\left(C+\frac{k}{(a+b\tau)^r}\right) \tag{5.31}$$

5.4.2 Parameter identification

Extraction of parameters of the SL model (5.28) uses both the end-conditions (f=f_r & τ=0) and, non-linear regression. At first, α is determined as $f_2(f_r)$ =1 $\Rightarrow$ α =1. Similarly, at τ= ∞ , $f_3(\tau)$=1 which implies, C=1. For identification of remaining constants, non-linear regression with the least least-squares technique is applied and, the best empirical fit for K_{Inv} is exhibited by the relation:

$$SL = \underbrace{\left(\left(\frac{1}{p}\frac{L_{lS}}{L_m}\right)^m\left(\frac{1}{p}\frac{L_{lR}}{L_m}\right)^n P_{Out}\right)}_{f_1(P_{Out})}\underbrace{\left(\left(\frac{f}{f_r}\right)^2\right)}_{f_2(f)}\underbrace{\left(\frac{I}{I_0}\right)^2\left(1+\frac{1}{(1+0.5\tau)}\right)}_{f_3(\tau)} \tag{5.32}$$

The obtained value of the coefficient of correlation (R^2) with (5.31) is 0.98. The values of the exponents m and, n are 0.95 and 0.34, respectively.

5.4.3 Statistical evaluation

The errors spectrum with the proposed model for results is given in Table 5.4. There is no reference model in available in the literature to compare with (in terms of relative error), and, hence, only the absolute error with the measurements is compared. The model parameters are trained using the test data of M1 and M2 and, in further verification of these parameters, the SL for M3, M4, M5 and, M6 is calculated. Comparison of the calculated and measured SL for M3, M4, M5 and, M6 for the two extremes of f_{SW}/f and T_L is shown in Fig. 5.5 ((a)-(d)).

Table 5.4: Error Spectrum Of the Proposed SL Model for Four IMs

Error(%)	No. of test-points	% of test-points
10-20	51	17.83
21-30	132	46.15
31-50	59	20.63
50-70	33	11.54
70-100	11	3.85
>100	0	0

Noteworthy observations, derived from the Table 5.4 and Fig. 5.5, regarding the prediction capability of the proposed SL model are mentioned below as:

- The proposed method ensures the accuracy of SL estimation with the estimation error less than 30% for 63.98% operating points of the test sample. Test points with error higher than 50% are 15.39% of the test domain.
- Measured SL is maximum for M1 and minimum for M3,with respective SL values equal to 1.44% and 1.03% of the rated output power. Hence, the slot geometry plays a significant role in SL deviation.

5.5 Conclusion

This chapter describes the up-gradation of the proposed SL model for inverter fed applications of the IM. In order to understand the impact of inverter power supply pattern on SL, experimental data of a wide range of inverter power supply parameters (*i.e.*,f and f_{SW}/f) and motors' loading (T_L) of two IMs is analysed to develop this model. Total 128 IMs' operating points are tested in this dimensional space of f, f_{SW}/f,T_L. The model uses IMs equivalent circuit parameters, nameplate details, and directly measurable electrical quantities to estimate the

SL, making the model applicable for both design and operation stages. To verify the accuracy of the proposed model, two IMs (of similar rated characteristics but different geometries) are tested for SL for another 128 operating points. Comparing the calculated SL with the measured SL shows the 50% interval of the accuracy to have 84.61% of the total 288 operating points. The correlation coefficient (r^2) with the proposed model is estimated to be 0.997.

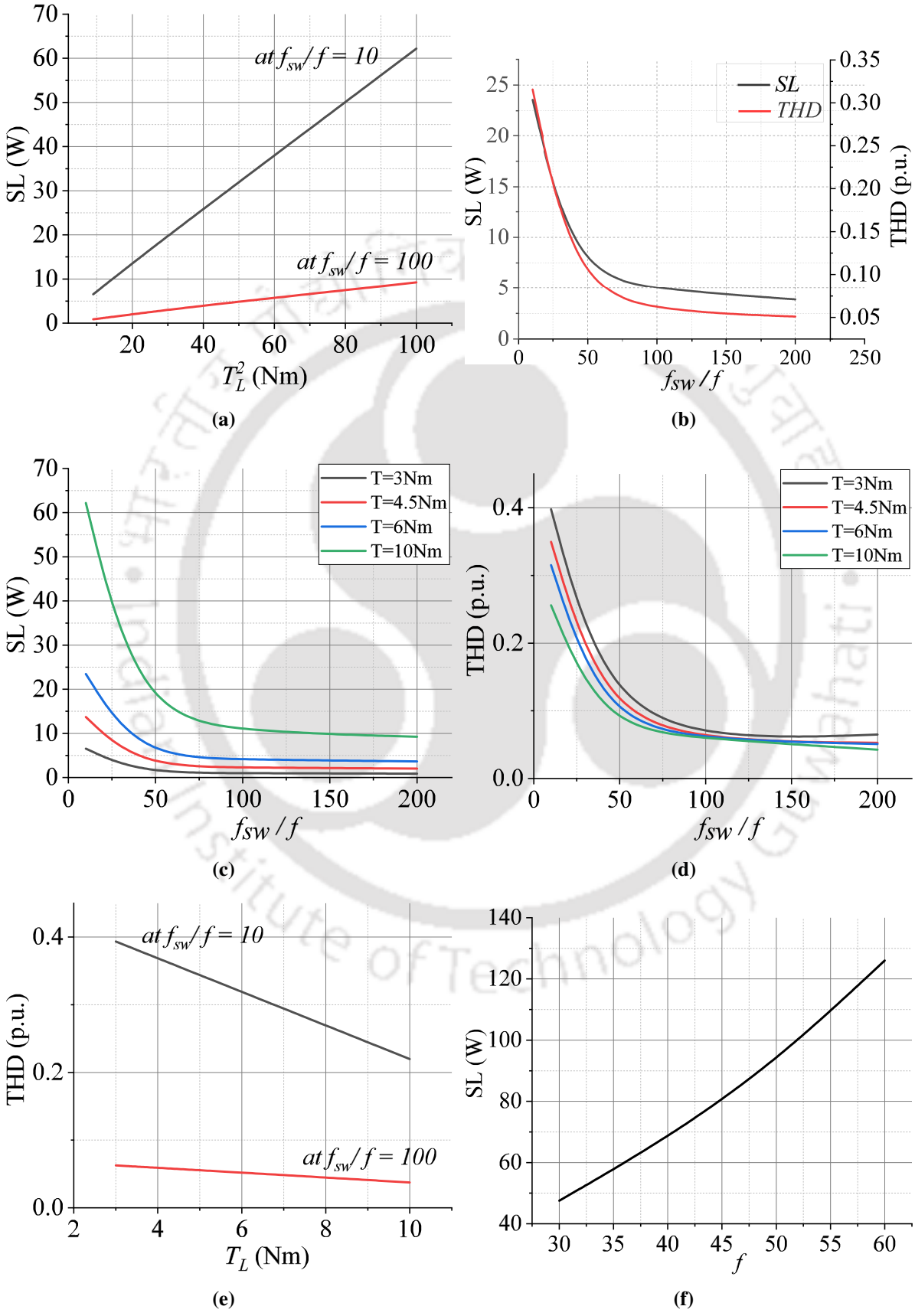

Fig. 5.3: Measurement results for IM-M1 (a) Variation of SL with T_L^2 for high and small values of f_{SW}/f at, (b) Correlation of SL and THD variations with f_{SW}/f, (c) Variation of SL with f_{SW}/f for different T_L, (d) Variation of THD with f_{SW}/f for different T_L, (e) Impact of loading on THD at high and small f_{SW}/f, (f) SL variation with f at constant f_{SW}/f (=10) and, T_L (=10Nm). f, in all these plots, = 30Hz.

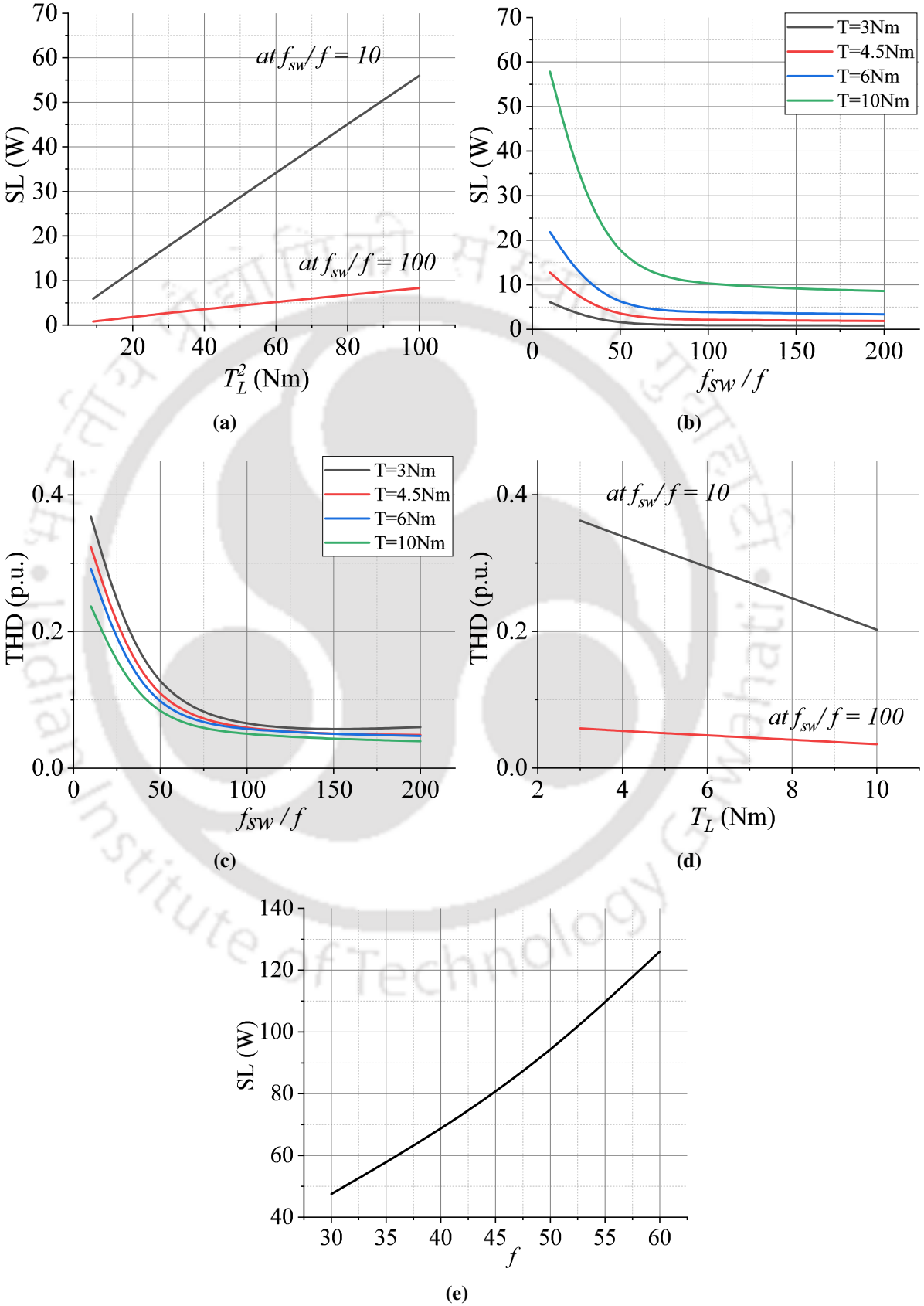

Fig. 5.4: Measurement results for IM-M1 (a) Variation of SL with T_L^2 for high and small values of f_{SW}/f, (b) Correlation of SL and THD variations with f_{SW}/f, (c) Variation of SL with f_{SW}/f for different T_L, (d) Variation of THD with f_{SW}/f for different T_L, (e) Impact of loading on THD at high and small f_{SW}/f, (f) SL variation with f at constant f_{SW}/f (=10) and, T_L (=10Nm). f, in all these plots, = 30Hz.

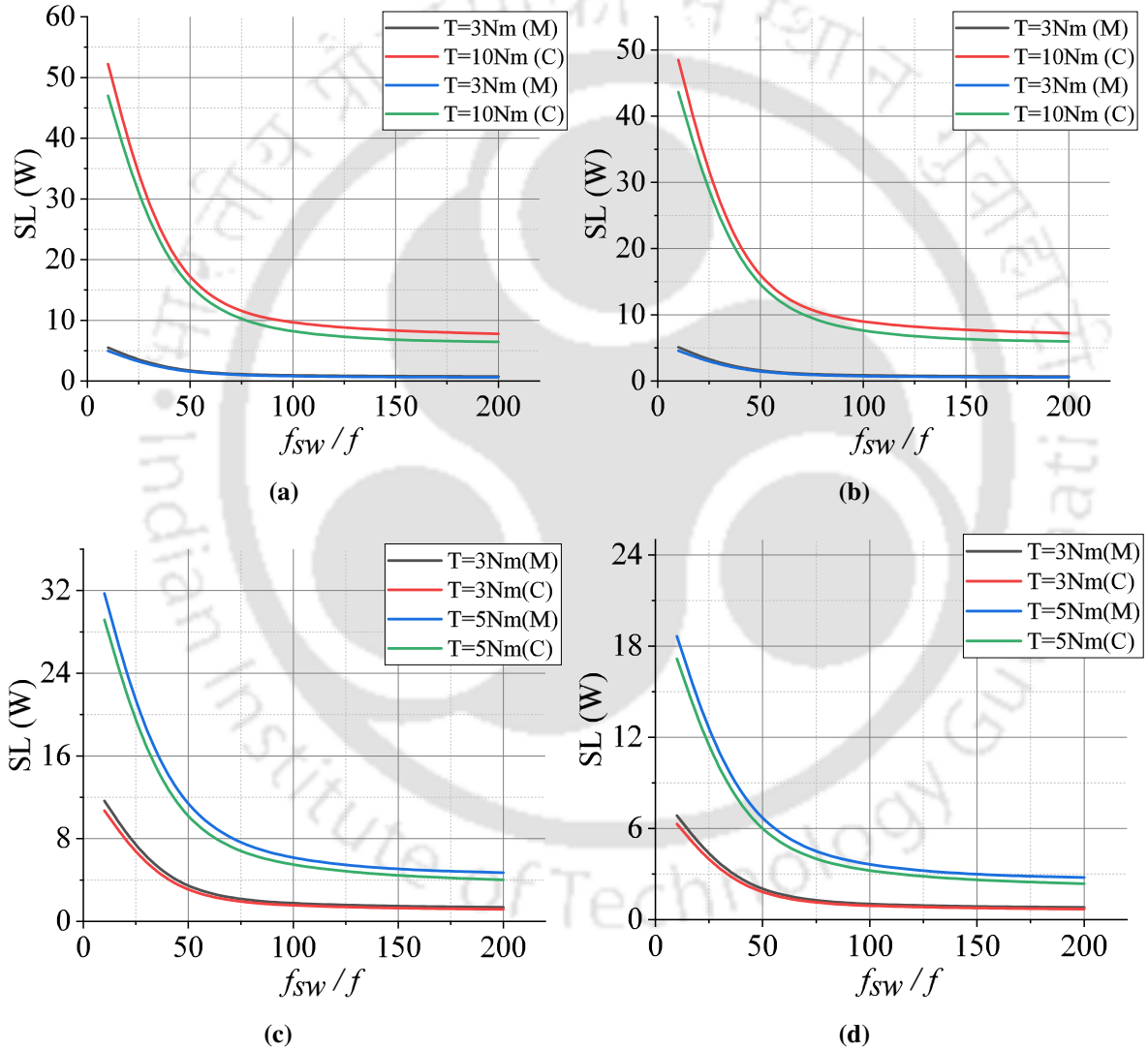

Fig. 5.5: Measured (M) and calculated (C) SL values for (a) M-4, (b) M-3, (c) M-5, (d) M-6.

6

Core loss for Inverter fed Motors

Contents

6.1 Introduction

Unlike the SL, the fundamental components of CL, the physical theories associated with these components and, their mathematical representation have been explored extensively. CL comprises only two or three (if excess loss is treated separately) distinct components, whereas the SL is the result of a total 9 different sources (as given in Table 3.1). As a result, the evaluation of CL with the post-FEA calculation is not as complex (and erroneous) as it is in the case of SL. In the opinion of chapter 2 of getting the exact loss-estimate of an IM, this chapter describes a fast and precise core loss estimation method for the inverter-fed induction machines. The presented method considers the influence of time variation of magnetic permeability on the lamination thickness and, consequently, the eddy current loss. In addition, the proposed method offers an objective approach to precisely evaluate the hysteresis loss. The results obtained from the proposed method are compared with the existing methods for an inverter-driven induction motor. The technique exhibits sufficiently high accuracy with reduced complexity and implementation time for a wide range of inverter switching frequency and motors loading.

6.2 Classification of CL models

Evaluation of the CL Steinmetz equation(SE) and the classical two-term model (CTTM) are the two empirical relations for CL evaluation for a sinusoidal magnetic field variation. However, in an electric machine, due to various reasons like stepwise MMF distribution, variation in air-gap permeance due to slots,magnetic saturation, and power supply harmonics, the stator and rotor's flux density deviates from the sinusoid. Consequently, CL estimation with these two relations (*i.e.*, SE, and CTTM) is not suitable for a motor and shows erroneous results. Therefore, researchers have proposed various techniques to estimate CL, and they can be broadly classified as:

6.2.0.1 Superposition based CL models (SBM)

Superposition based models use the Fourier decomposition of the flux density (B) waveforms, and net specific core loss (P_{CL_s}) is calculated as the sum of CLs of all the harmonics as

$$P_{CL_s} = \sum_{i=1}^{n} P_{CL_s i}(f_i, B_{max\_i}) \tag{6.1}$$

where, $P_{CL_s i}(f_i, B_{max\_i})$ is the specific core loss generated individually by the $i-th$ harmonic of B_{max_i} magnitude and, f_i frequency. Two different formulations/models are in wide practice to determine the CL with (6.1). These models are developed for a sinusoidal excitation. One of them is the Steinmetz equation written as

$$P_{CL_s} = C_m . f^{\alpha} B_{max}^{\beta} \tag{6.2}$$

where, f, B_{max} denote frequency and, magnitude of the magnetisation, respectively. C_m, α and, β are Steinmetz coefficients. The model (*i.e*, (6.2)) employs least number of coefficients. However, its application range (in terms of B_{max},f) is very limited as it is erroneous to represent the two phenomenal components of the core loss (hysteresis loss and eddy current loss) using a single empirical term. Since, both of these components show different degrees of variations with the B_{max} and f. Therefore, another model of CL, with a scientific formulation of the eddy current loss, represents it with two-terms as

$$P_{CL_s} = k_h f B_{max}^{\beta} + k_e f^2 B_{max}^2 \tag{6.3}$$

where, K_h, K_e, and α are frequency and magnetization dependant loss-coefficients.

The FFT decomposition facilitates the application of (6.2) and, (6.3) as it is. However, applying the superposition for a non-linear routine is the main concern here, particularly for P_{Hys}.

6.2.0.2 Non-superposition based CL models (NSBM)

These methods evaluate the CL in the time-domain analysis of the instantaneous magnetization quantities, *i.e*., $B(t)$ and $H(t)$. This time-domain analysis led to several modifications in the (1) and (2) to present an empirical relation. For example, the first such dynamic time-domain model MSE(Modified Steinmetz Equation) presented the CL using a cycle averaged value of the squared rate of change of $B(t)$, *i.e*., equivalent frequency (f_{eq}) as

$$P_{CL_s} = (C_m f_{eq}^{\alpha-1} B_{max}^{\beta}) f \tag{6.4}$$

where,

$$f_{eq} = \frac{2}{\Delta B^2 \pi^2} \int_0^T \left[\frac{dB}{dt}\right]^2 .dt \tag{6.5}$$

The above techniques 1) and 2) can be further branched out and a comprehensive overview is given in Fig.6.1 Also, there exist hybrid methods which determine the P_{Eddy} using (6.3) and

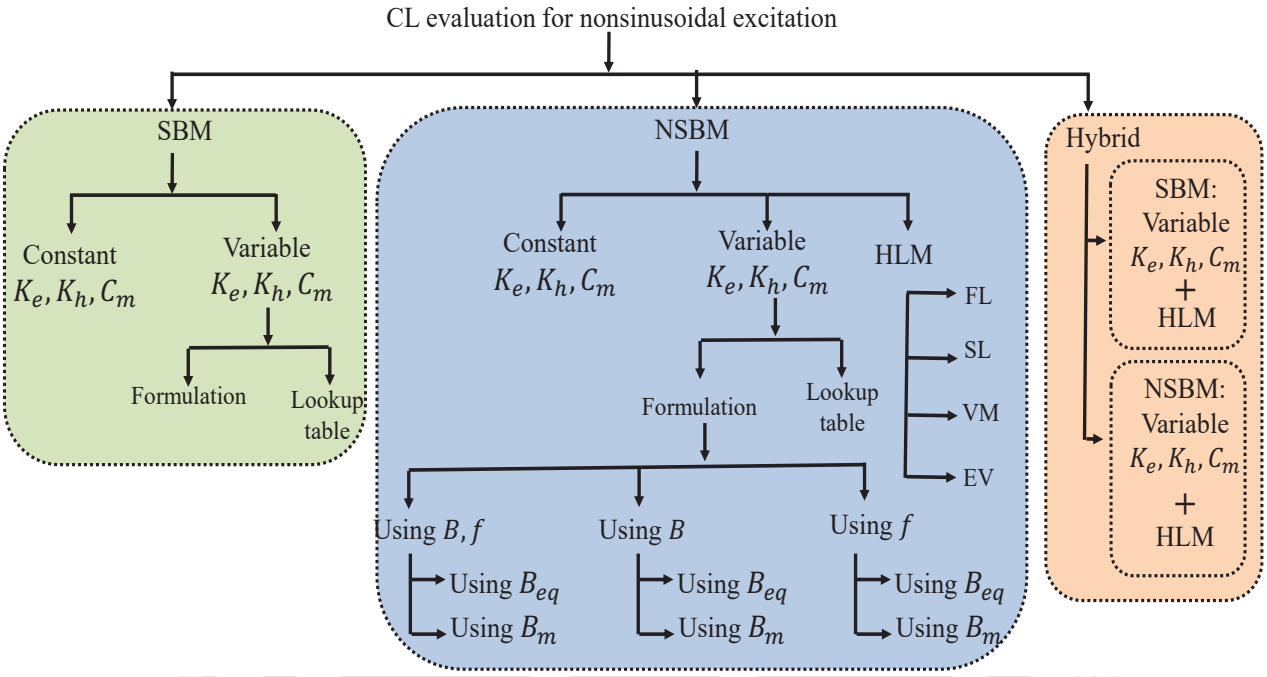

Fig. 6.1: Classifications of the CL estimation approaches

P_{Hyss} using hysteresis loss models [37, 66].

6.3 Qualitative analysis

All the existing models claim to have good accuracy for the range (in terms of B_{max},f) and, the material using which they are developed. Hence, the utilization of these models needs a thorough comparative qualitative analysis. Table 1.1 narrates their relative comparison for various application parameters. The estimation error with the above models varies depending on the application. In some cases, the error exceeds 80% of the estimation [15]. One of the main reasons for higher error is that these approaches are based on curve fitting an equation to the measurement results, and so the fitting is performed at a certain condition. Hence, the model gives an accurate loss estimation as long as the test conditions match with the conditions in which the data is taken. On the other hand, the mathematical hysteresis models in combination

with 1-D eddy current models show a much higher accuracy. The overall performance of these hybrid techniques is mainly attributed to the hysteresis model used. Based upon the synthesis approach, the HLMs broadly fall into two categories, *i.e.*, a).domain wall movement based HLMs and b). curve fitting based HLMs. The relative comparison of various HLMs is given in Table 6.1. However, the development of the hysteresis models requires in-depth insight

Table 6.1: Prominent hysteresis loop models and their comparison

Sr.No.	Parameter	JA	Preisach	Glabus modified	Stoner-Wohlfarth
1	Approach	CF	CF	DWM	DWM+RT
2	Reversibility	Additional model	Additional model	Yes	Yes
3	Anhysteresistc	Yes	Yes	Yes	Yes
4	Variables	5	5	4	6
5	Run Time	H	VVH	H	VH
6	Realisation	Easy	Moderate	Difficult	Difficult
7	Materials	Medium ferrites	Thin films	Soft ferrites	Hard magnetic materials
8	Minor loops	Yes	Yes	-	Yes

CF: Curve-fitting; DWM: Domain wall movement; RT:rotation of H-vector

into the material properties and measurement data under different test conditions. There exists a possibility of further treatment for centro-symmetricity in case of DC bias magnetisation [67].Moreover, the integration of these models into the FEA simulations is not straightforward and simulations take much longer time to run.

From the above discussion, it is evident that there is a need of a comprehensive CL model. Such CL model should address the following difficulties:

- The high error in the estimation of P_{Eddy} due to variation of lamination thickness especially, at higher magnetisation.
- Precise and rapid evaluation of P_{Hyss} for a highly distorted magnetic field variation.

Next section details the proposed CL method addressing the above difficulties.

6.4 Proposed CL Method

The proposed method uses flux density waveforms retrieved from the FEA and evaluates the CL in the post-processing. The formulation of the proposed method employs the superposition based approach for P_{Eddy} and, time-domain approach for P_{Hyss} [36,37], which, in classical form

(for a homogeneous distribution of B) is expressed as [68], [69]

$$P_{CL_s} = \underbrace{\frac{1}{T}\int_{-B_m}^{+B_m}\left(\frac{\sigma\tau^2}{12}\frac{dB(t)}{dt}\right).dB(t)}_{\mathrm{P_{Eddy_S}}} + \underbrace{\frac{1}{T}\oint_C H(t).dB(t)}_{\mathrm{P_{Hys_S}}} \tag{6.6}$$

where, τ is the lamination thickness and μ is material's magnetic permeability. The dependance of τ on frequency (f) and material permeability (μ) due to skin-effect further complicates (6.6) by replacing τ with $\tau(f,\mu)$ *i.e.*, [69]

$$\tau(f,\mu) = \tau\sqrt{3\pi}\left(\frac{\sinh\varepsilon - \sin\varepsilon}{\varepsilon(cosh\varepsilon - \cos\varepsilon)}\right)^{1/2} \tag{6.7}$$

where,

$$\varepsilon = \tau\sqrt{\mu f\sigma\pi} \tag{6.8}$$

The computation of (6.6) is difficult because it uses $B(t)$ as primary variable and, frequency dependant permeability expression *i.e.*, (6.7). To simplify (6.6) and, use it for CL estimation, the following modifications have to be done:

1. Changing of the equation's domain (*i.e.*, from $B(t)$-variable form to time-variable form).
2. Assuming the permeability time-invariant for the range of integral.

In the the following subsections, the use of equation (6.6) for CL estimation is explained.

6.4.1 Eddy current loss(P_{Eddy})

Rewriting the integral term of P_{Eddy_S}(6.6) in time-variable form gives

$$P_{Ed}(f,\mu) = \frac{1}{T}\frac{\sigma\tau(f,\mu)^2}{12}\int_0^T\left(\frac{dB(t)}{dt}\right)^2.dt \tag{6.9}$$

Evaluation of (6.9) for a sinusoidal field variation($B(t)$) with time-independent τ *i.e.* $\tau(f,\mu)$ provides

$$P_{Ed}(f,\mu,B_{\max}) = \left(\frac{\sigma\tau(f,\mu)^2}{6}\right)B^2{}_{\max}f^2 \tag{6.10}$$

To apply (6.10) for a nonsinusoidal field variation ($B(t)$), magnitudes of all the harmonic orders are calculated and net P_{Eddy_S} is determined as sum of P_{Eddy_S}s of all harmonics *i.e.* for

$$B(t) = \sum_{i=1}^{n} B_{\max i} \cos(\omega_i t + \phi_i) \tag{6.11}$$

,

$$P_{Eddy_s} = \sum_{i=1}^{n} P_{Ed}(f_i, \mu_i, B_{\max\_i}) \tag{6.12}$$

Generally, while solving (6.9) to get (6.10), the material permeability (μ) is assumed constant for a particular value of B_{max} and f. This, in fact simplifies the evaluation of (6.9) treating $\tau(f, \mu)$ a constant. In [70], this constant μ is taken corresponding to the B_{max} whereas, [66] suggests the μ at average value of excitation.

However, the value of μ depends upon the magnetisation (as shown in Fig.6.3-(b)), and hence, it does not remain constant for all the instants of a time period. Fig. 6.3(c) shows the variation of μ over a time period *i.e.*, $\mu(B(t))$. Value of μ is minimum at the maximum value of the excitation. Hence, taking the μ of maximum magnetisation overestimates the lamination thickness (as per (6.7)) and consequently gives higher P_{Eddy_S} value (as per (6.10)). Also, it is imperative to mention here that the variation in μ within the cycle increases with the increase in the maximum magnitude of the waveform (B_{max}). The Fig.6.3(c)-(d) show its variation for both higher and smaller magnetisation B_{max}. As a consequence, τ also modulates along a fixed value $\tau(f, \mu)$ (as shown in Fig.6.3(e)) calculated by (6.7)-(6.8). As mentioned in Section II-C, the variation in τ has been one of the major sources of error in P_{Eddy} estimation. Hence, the expression (6.9) needs to be evaluated with taking the time-variation of τ into account as

$$P_{Ed}(f_i) = \frac{1}{T_i} \frac{\sigma}{12} \int_0^{T_i} \tau(f_i, \mu(B(t))^2 \left(\frac{dB(t)}{dt}\right)^2 dt \tag{6.13}$$

In a simplest form, the variation in τ (as shown in Fig.6.3-(e)) can be written as

$$\tau(f, t) = \tau_{0f} + \Delta\tau_f |\sin(\omega t)| \tag{6.14}$$

where,

$$\tau_{0f} = \frac{\tau(f,\mu_{max}) + \tau(f,\mu_{min})}{2} \tag{6.15}$$

$$\Delta\tau_f = \tau(f,\mu_{min}) - \tau(f,\mu_{max}) \tag{6.16}$$

Solving the expression (6.13) and (6.14) for sinusoidal $B(t)$ gives

$$P_{Ed}(f, B_{\max}, \tau') = \left(\frac{\sigma\tau'(f,\mu)^2}{6}\right) {B^2}_{\max} f^2 \tag{6.17}$$

where, $\tau'(f,\mu)$ comes out as

$$\tau'(f,\mu) = \left({\tau^2}_{0f} + \left(\frac{\Delta\tau_f}{4}\right)^2\right)^{1/2} \tag{6.18}$$

which is the root mean squared (rms) value of $\tau(f,t)$. The proposed method hence suggests the evaluation of (6.13) with taking the rms of the τ. This rms value of $\tau(f,t)$ is calculated using (6.7), (6.14) and,(6.15). The proposed modification does not impose the restriction on applying the superposition and, the P_{Eddy_S} for a non-sinusoidal $B(t)$, with it is calculated as

$$P_{Eddy_s} = \sum_{i=1}^{n} P_{Ed}(f_i, {B_{\max}}_i, \tau_i') \tag{6.19}$$

where, $P_{Ed}(f, B_{\max}, \tau')$ is calculated using (6.17). For numerical values of B-data obtained by FEA, the discrete form of the proposed evaluation (6.19) is used as

$$P_{Ed}(f_i) = \frac{1}{N_i}\frac{\sigma}{12}\sum_{k=1}^{N_i} \tau'(f_i, \mu(B_i(k))^2 \frac{(B_i(k+1) - B_i(k))^2}{t_{k+1} - t_k} \tag{6.20}$$

where, k denotes the discrete time instant and, N_i is total number of time instants in the time-period of T_i. Comparison of the P_{Eddy} values obtained from (6.10) and (6.17) with the measured values is shown in Fig.6.2.

6.4.2 Hysteresis loss P_{Hys}

The term for P_{Hys_s} in (6.6) is f -times the area of the hysteresis loop in $B-H$ plane. In inverter fed motors, flux density waveforms (of different motor segments) consist of higher-order time harmonics, which results in several minor loops. SBMs, in this case, calculate the

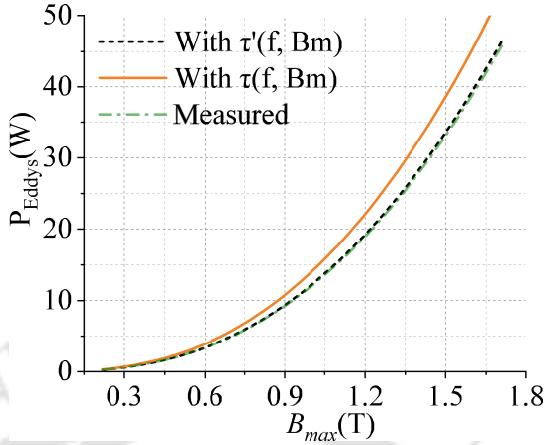

Fig. 6.2: Eddy current losses evaluations with the proposed (6.17) and existing (6.10) method at $f = 400Hz$.

net hysteresis loss as sum of areas of all the loops [31, 35].

However, this method results in higher P_{Hys_s} because the sum of areas of the loops created by each harmonic independently is greater than the actual hysteresis area. The reason for the higher estimation of P_{Hys_s} is mainly due to the following three reasons:

- The addition of a harmonic in a sinusoidal B-waveform does not always create a minor loop. As shown in Fig.6.4 (a and b), both the B-waveforms (of equal fundamental component B_{max_1}) comprise equal magnitudes of 3^{rd} and 5^{th} harmonics (B_{max_3},B_{max_5}) but their B-H loops are different.The B-H loop of B-waveform (a) does not form any minor loop whereas, the B-H loop of B-waveform(b) results in two minor loops, each corresponding to the one harmonic component.
- the area of the minor loop (if generated) for a particular harmonic is not exactly equal to the area of the hysteresis loop created by that harmonic independently with the same magnitude.The minor loop area is affected by the DC-bias offered at its location by the major loop. Fig.6.3(f) shows this impact taking DC offset 0T and, 0.8T.
- it is not necessary that the difference of time instants of maxima and minima of a minor loop provides the time period of a particular harmonic. The superposition of multiple harmonics with different phase-angles may shift the location of these maxima and minima.

The above limitations result in the inaccurate prediction of the hysteresis loss for a distorted B-waveform using an empirical expression. Modelling of the hysteresis loop gives a good solution. The Preisach model, the Glabus modified, and the Jiles-Atherton model are the prominent hysteresis loop models [71]. These models use H (or B) as an independent variable and compute

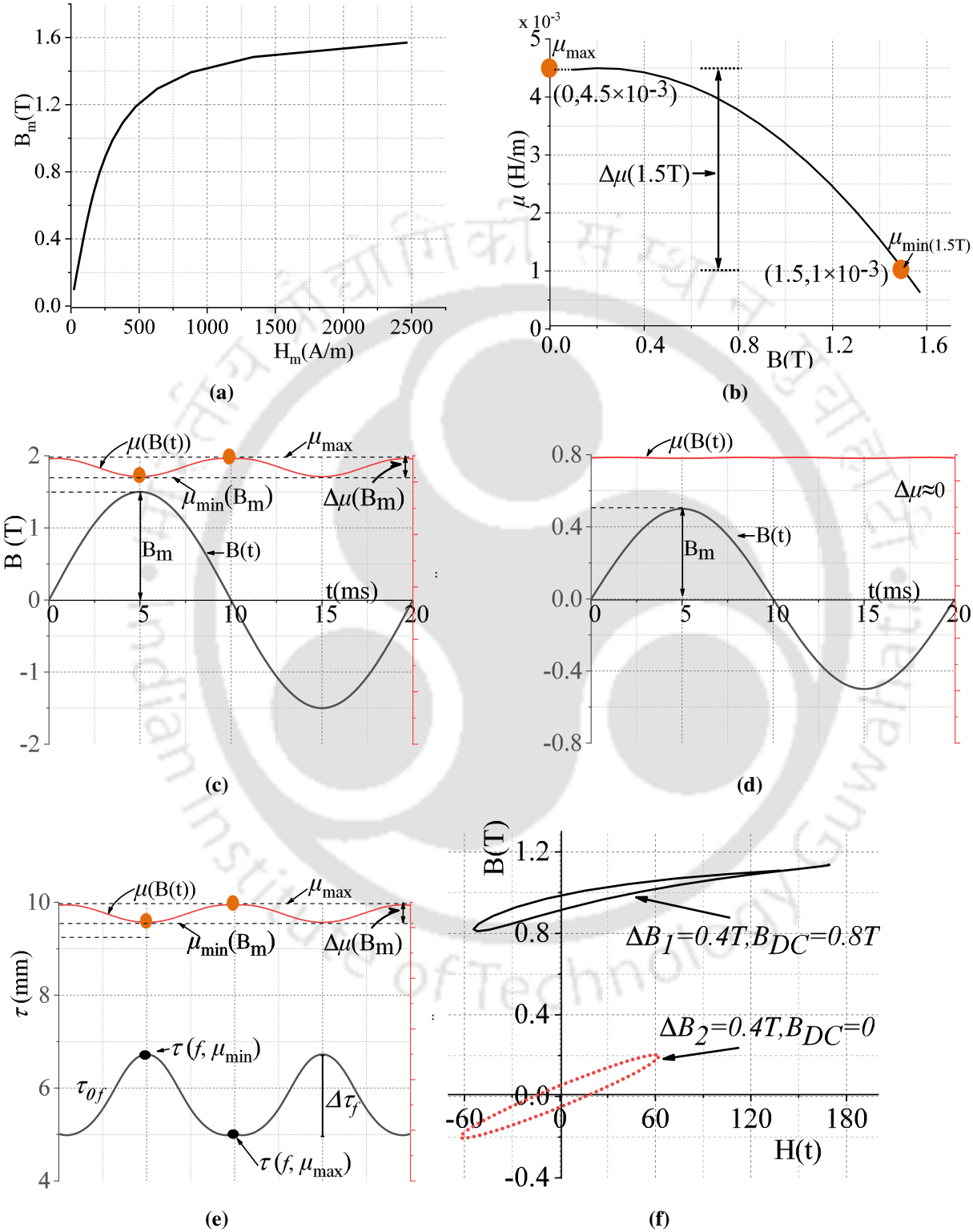

Fig. 6.3: (a) $B-H$ graph for the ferromagnetic material 50C350; (b) Differential permeability (μ) with $B(t)$ for graph (a); (c) Deviation in (μ) for a sinusoidal induction of higher B_{max}; (d) Deviation in (μ) for the sinusoidal induction of lower B_{max}; (e) Fluctuation in τ with μ of (c); (f) Effect of the DC-bias on area of the hysteresis minor loop.

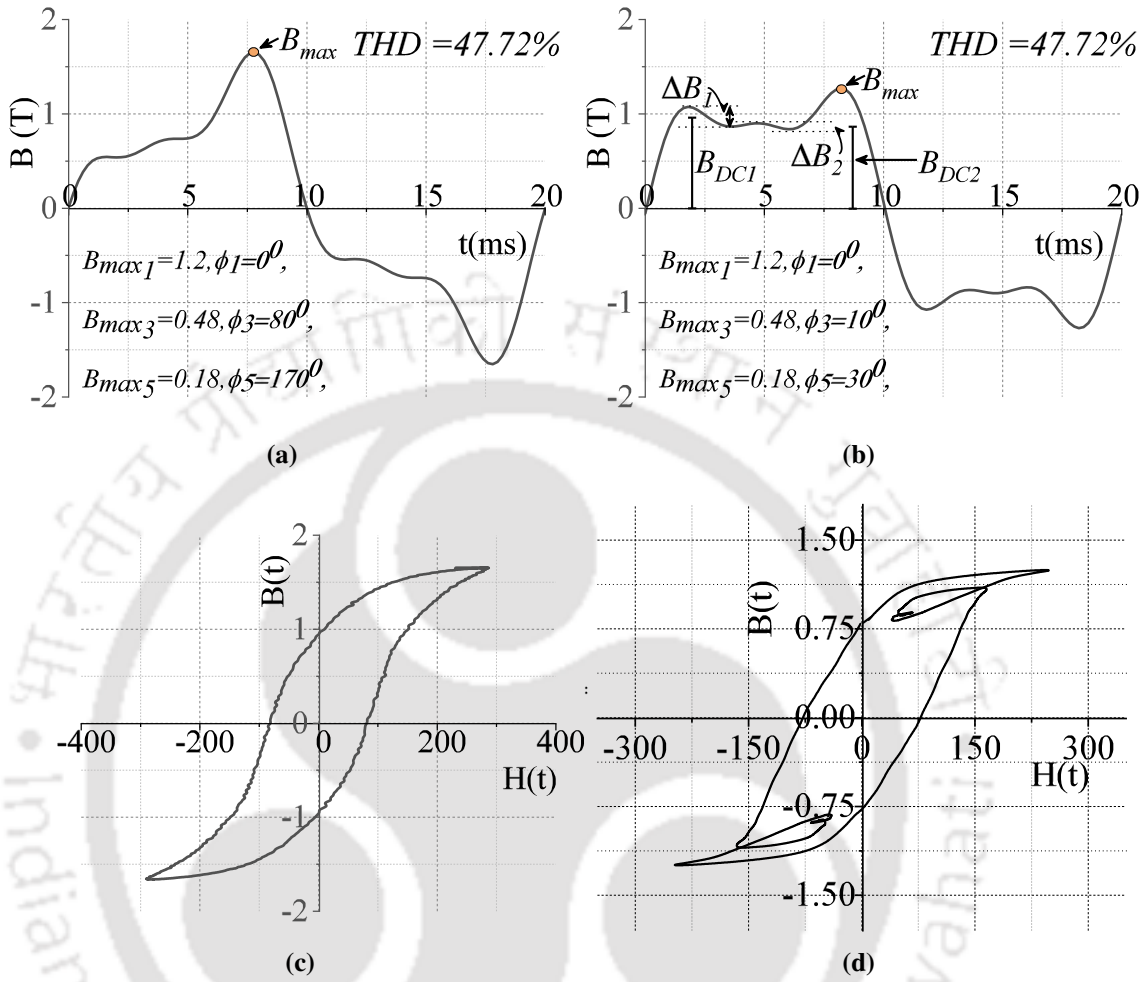

Fig. 6.4: (a) Electromagnetic induction waveform-A (47.2% THD); (b) Electromagnetic induction waveform-B (47.2% THD); (c) Hysteresis loop with reference to the waveform-A; (d) Hysteresis loop with reference to the waveform-B.

the corresponding B (or H) value. HL is created using these B-H values for one complete cycle.

The proposed method puts forward a new alternate time-domain approach to determine the area of HL for a distorted B-waveform without evaluating the H (*i.e.*, without forming the major and minor HL). The method uses the following two data: a).measured values of HL areas (dynamic) with sinusoidal excitations as a prerequisite which are evaluated using Epstein frame as detailed in section III. b).time-instant B values of the distorted B-waveform which can be directly retrieved from the magnetic vector potential based formulation in FEM. Due to the symmetry of B-waveform, only the half-cycle data is used here. In execution of the proposed method, time spaced half cycle B-data is examined sequentially for its rate of change to get all its local and global extrema (B_1,B_2,B_3..B_M as shown in Fig.6.4-(b)) as points of zero slope. From the sequentially stored values of these extrema, the net HL area is evaluated using the

measured HL areas for sinusoidal magnetisation of different magnitudes as described below:

- area of major loop (A_m)- the maximum absolute value of the stored extrema(B_{max}) corresponds to the major loop. Hence, the loop area measured for maximum magnetisation = B_{max} for sinusoidal excitation is taken as an area of major loop.
- the area of a minor loop (A_i)- the difference between consecutive maxima and minima (ΔB_i=$B_n - B_{n-1}$) gives the height of minor loop in B-H plane. The measured HL area corresponding to the maximum B value equal to the half of the ΔB_i is taken as the area of the minor loop(with zero DC bias) *i.e.*,

$$A_{0i} = A_{measured}\left(\frac{\Delta B_i}{2}\right) \tag{6.21}$$

where $A_{measured}(B_i)$ is the measured value of the HL area with the sinusoidal magnetization of the maximum magnitude of B_i without DC bias. The DC bias offered at the location of a minor loop is equal to B_{DC_i}=$(B_n + B_{n-1})/2$)(Fig.6.4(b)). The area of minor loop with this DC bias is calculated as [72]

$$A_i = A_{0i}\left(1 + k_{DC}{B_{DC_i}}^{\alpha}\right) \tag{6.22}$$

where k_{DC} and α are the constants representing the variation in HL area with DC bias. They are obtained from the measurements as per [72] and, there values for the steel used in this work are 0.67 and 2 respectively.

- total area of the HL and, the corresponding specific hysteresis loss is determined as

$$P_{Hys_s} = \left(A_m + \sum_{i=1}^{L} A_i\right) f \tag{6.23}$$

where L and f are total number of the minor loops and fundamental frequency respectively.

The proposed method uses hysteresis loss data with sinusoidal excitation as a prerequisite which are evaluated as detailed in Section IV.

6.5 CL Characterisation of material

The IM used in this work is made of ferromagnetic core material 50C350. The loss characterisation of this material is done with 352 turns Epstein frame. The setup consists of primary and secondary windings mounted uniformly on the four sides of the frame inside which the sample iron-sheets are placed. A pulsating (of sinusoidal time variation) magnetic field is set up in the sample iron sheets by exciting the primary side from a 3kW power amplifier. The THD in voltage (or B-waveform) is limited to 0.5%. The field strength $H(t)$ inside the sample sheet is determined from the primary current as:

$$H(t) = \frac{N_P I(t)}{l_{mean}} \tag{6.24}$$

where, l_{mean} is mean length of the magnetic flux path, N_P is the number of turns in primary winding. The flux density B is defined via measurement of the voltage induced in the secondary winding ($v_S(t)$) as

$$B(t) = \frac{\phi(t)}{A_{core}} = \frac{1}{A_{core} N_S} \int_0^t v_S(t) dt \tag{6.25}$$

where, A_{Core} is the crosssection area for the flux, N_S is the number of secondary windings. The total iron loss for the volume of sample iron-sheets is obtained as shown

$$P_{CL} = \frac{N_P}{N_S}(P_{in} - I^2 R_P) \tag{6.26}$$

where, P_{CL} is the total iron loss of the core sample, P_{In} is the input power for the primary coil, R_P is the primary coil resistance. Total core loss estimated with (6.26) is sum of two losses *viz.* eddy current loss and hysteresis losses,

$$P_{CL} = P_{Eddy} + P_{Hyst.} \tag{6.27}$$

The components of field strength $H(t)$ in (6.24) corresponding to these losses are,

$$H(t) = H(t)_{Eddy} + H(t)_{Hyst.} \tag{6.28}$$

The instantaneous value of $H(t)_{Eddy}$ is determined from the instantaneous flux density in (6.25) as

$$H(t)_{Eddy} = \frac{\sigma}{12}\tau'(f,\mu)^2\frac{dB(t)}{dt} \tag{6.29}$$

Using (6.28), (6.18) for the effective $\tau'(f,\mu)$ lamination thickness, field strength corresponding to the magnetic hysteresis $H(t)_{Hyst.}$ is obtained as

$$H(t)_{Hyst.} = H(t) - \frac{\sigma}{12}\tau'(f,\mu)^2\frac{dB(t)}{dt} \tag{6.30}$$

The area under the $B(t)$ versus $H(t)$ curve, *i.e.*,

$$A_{Net} = \oint H(t)dB(t) \tag{6.31}$$

gives the net core loss P_{CL} of a cycle, whereas the area under the $B(t)$ versus $H(t)_{Hyst.}$ curve

$$A_{Hyst.} = \oint H(t)_{Hyst.}dB(t) \tag{6.32}$$

evaluates the hysteresis loss. Fig.6.5 shows both these areas for 1.3T, 100Hz. Fig.6.6(a)-(d) show the the separated specific losses (P_{Eddy_s} and P_{Hys_s}) for the range of and magnetisation strength at low and high frequencies. As P_{Eddy} here is determined with taking the skin effect into account, applying loss separation to the measured total CL gives P_{Hys} with skin effect. The excess loss term is neglected in this estimation [35, 73, 74].

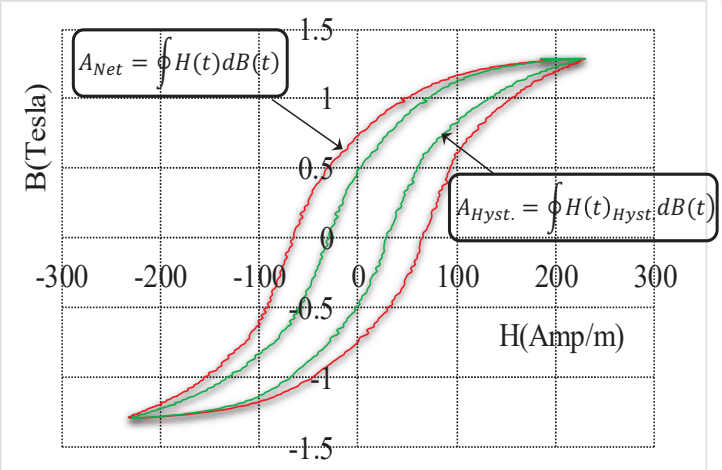

Fig. 6.5: B-H loops with reference to the overall and magnetising field intensities at "100Hz,1.3T".

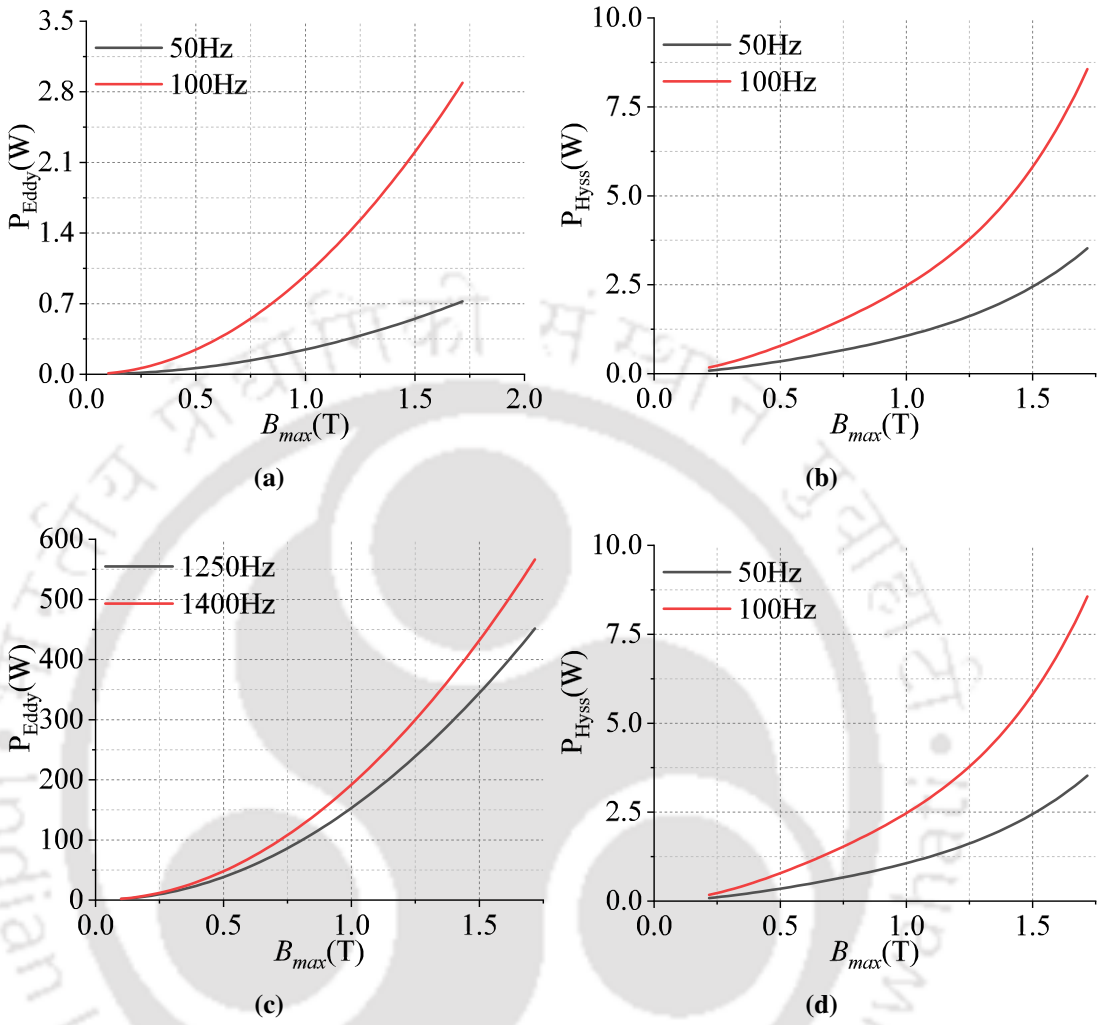

Fig. 6.6: Loss segregation: "P_{Eddy} and $P_{Hyst.}$" for the end-values of the magnetic-induction and supply frequency.

6.6 CL Evaluation for IM

This section presents the application of the proposed method in the evaluation of CL for an inverter fed IM. For this, a 1.5kW three phase IM is selected. Table 6.3 shows the rated parameters of this IM. As mentioned in Section-IIC, the proposed method uses one cycle time data of flux density, a 2-D FEA model of the 1.5kW IM is developed in Maxwell Ansys 19.2. The stator windings of the FEA model are excited with measured current waveforms and, the model is run with the anhysteretic magnetisation and active eddy current effect.

Retrieving the B-data for all the nodes of mesh elements and their CL calculation demands requires storage. Hence, the motor geometry is divided into small segments [15, 75, 76] of homogenous flux density. Both the tangential (B_T)and radial(B_R) components of magnetic field

density inside a segment are constant [15, 75, 76]. Fig.6.7 shows the motor crosssection with segments. To apply the proposed method,both B_T and B_T are extracted from the FEA model for one fundamental time period.Using the B_T and B_R, specific CL for the segment evaluated as

a). P_{Eddy_S}: using the expression (6.20) *i.e.*, the evaluation with instantaneous flux density dependant permeability (*i.e.*, $\mu(B(t))$. P_{Eddy_s} with B_T and B_R are determined separately and added to get total P_{Eddy_s}.

b). P_{Hys_s}: using the expression (6.23).

Net CL of the machine is estimated as

$$P_{CL} = \sum_{i=1}^{S} m_i[P_{Hys_s\_i} + P_{Eddy_s\_i}] \tag{6.33}$$

where, S is the total number of geometry segments and, m_i denotes the mass of i-th segment.

The FEA model is run for multiple measurements of motor currents to encase the entire range of the IM's operation (0.5 Nm to 2.5 Nm) and carrier frequency variation (300Hz to 5kHz). For each operating point, CL is evaluated by applying the proposed method at two conditions, *i.e.*, a). on-load and, b). no-load at the same voltage.

For the selected motor, the housing-stator interface stress is very small (0.423 MPa); hence its impact is not included in FEA [77]. FEA with taking the stress into account prerequisites a static 2-D stress/structure FEA to get the stress values for each location of the core [78], [79]. The electromagnetic FEA is then performed using the stress dependant permeability *i.e.*, $\mu = \mu(\sigma_1, \sigma_2, B_1, B_2)$ where, σ and B are the von Mises stress and magnetic flux density, respectively. Subscripts 1 and 2 denote the orthogonal components of a 2-D distribution [78], [79]. Fig.6.8 shows the evaluation process for both conditions (*i.e.*, with and, without stress).

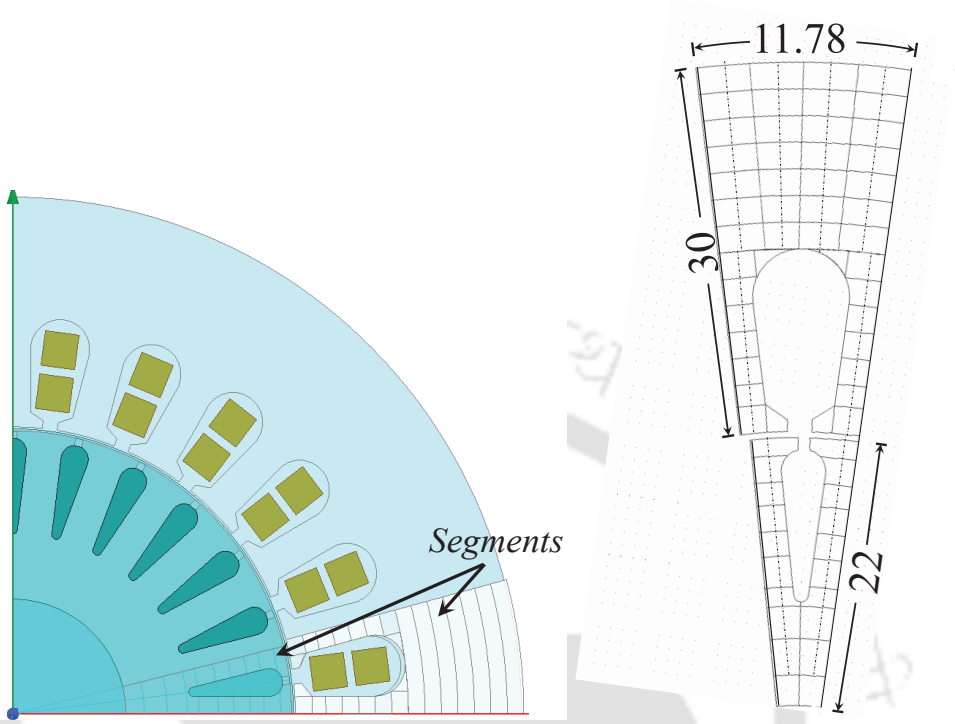

(a) (b)

Fig. 6.7: (a). IM model for the 2-D FEA , (b). Segments for one slot-pitch (in mm).

Table 6.2: Motor Operation Domain

	Speed (rpm)	Torque (Nm)	f_{SW}	Power -supply
Upper value	2889	2.5	5000	Sine pulse width
Lower value	2889	0.5	300	modulation
Steps	1	5	10	(SPWM)

6.7 Experimental measurement of CL

Fig. 6.9 shows the results obtained with the proposed technique. For experimental verification of these results, the IM is operated with an inverter power supply.

CL is evaluated for a total 50 operating points of the motor, as given in Table 6.2. For all these operating points,the motors's is fixed at 2889rpm by varying its terminal voltage. Fig.6.13

shows the voltage variation for the two extremes of switching frequencies, *i.e.*, 300 Hz and 5 kHz. No-load CL values corresponding to these 50 operating points are obtained by running the decoupled motor at voltage corresponding to the torque value (as shown in Fig. 6.13-(a).)

Table 6.3: Specifications of the test IM

Sr.	Parameter	Unit	Value
1	Pole-pair	-	1
2	V_{Rated},frequency	Volt./Hz	415/50
3	Output power	kW	1.5
4	Core iron-grade		50C350
5	Lamination thickness	mm	0.5
6	Slots: Stator, Rotor	Number	36,34
7	Outer diameter	mm	135
8	Inner diameter	mm	75
9	Stack length	mm	100
10	Air-gap width	mm	0.5

6.7.1 Measurements-Set-up and procedure:

Mechanical (windage and bearing) losses of the IM are first calculated with the sinusoidal power supply as per [9]. Correction for stator resistance for temperature, skin depth and proximity effect is done as[24]:

$$R_S(T,f) = R_{S0}(1+\alpha(T-20))(1+\frac{l_s}{l_w}(k_{nR}(\xi)-1) \tag{6.34}$$

where, l_s is the the stack length and l_w is half the mean length of a stator turn. $k_{nR}(\xi)$ is skin and proximity effect factor depends upon the conductor size, number of strands, conductor per slot and slot dimensions. Stator copper losses are calculated with the measured values of input *rms* phase currents (I_s) as:

$$P_{CuS} = R_S(T,f)\sum_{i=1}^{3} I_i^2 \tag{6.35}$$

However, it is not possible to directly measure the rotor copper losses (P_{CuR}) for an inverter fed

squirrel cage IM.

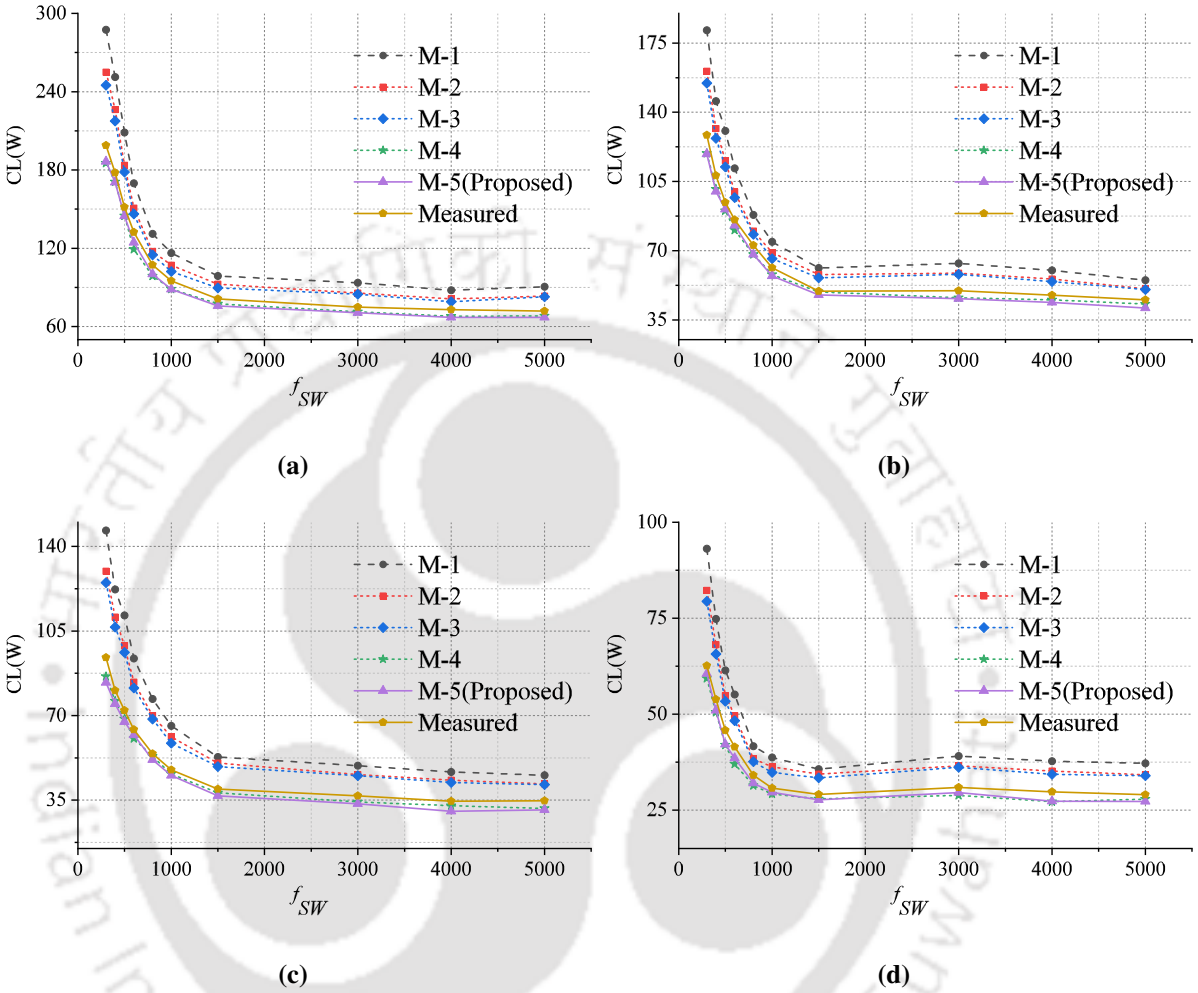

Fig. 6.9: Variation in on-load CL with f_{SW} for T_L equal to (a) 2.5 Nm, (b) 1.5 Nm, (c) 1.0 Nm (d), 0.5 Nm.

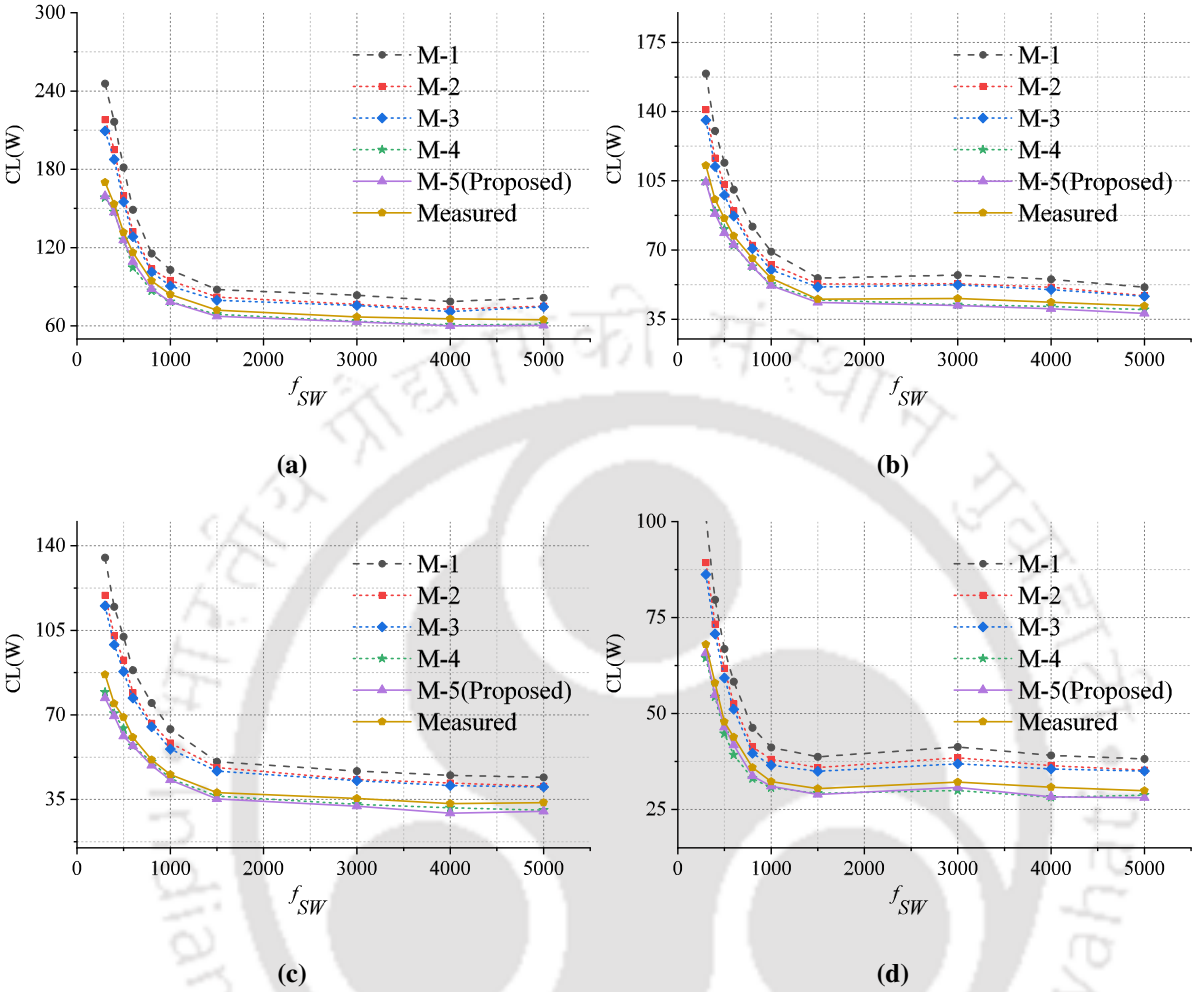

Fig. 6.10: Variation in no-load CL with f_{SW} for T_L equal to (a) 2.5 Nm, (b) 1.5 Nm, (c) 1.0 Nm (d), 0.5 Nm.

The presence of current harmonics make them non-negligible even for the no-load condition. Hence, their values are obtained from the FEA. For this, the current density waveforms at different segments (S_b) of the rotor-bar (as shown in Fig.6.11) are used and, P_{CuR} is determined as:

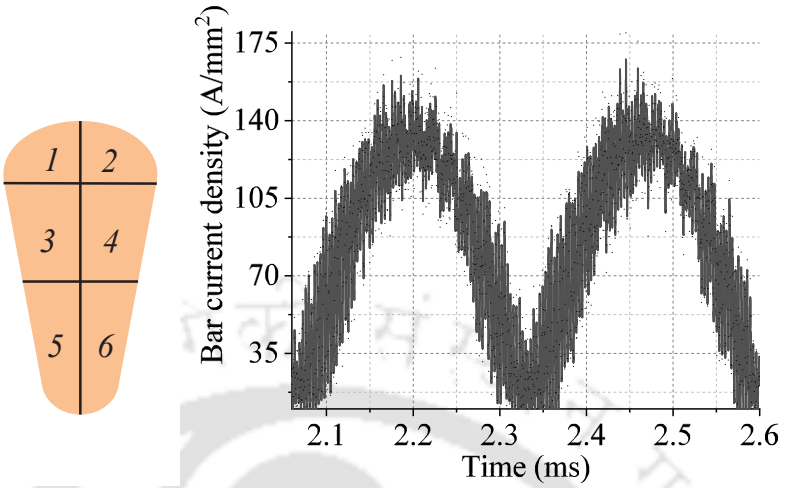

(a) **(b)**

Fig. 6.11: Determination of P_{CuR}: (a) Rotor bar segments (b) Current density magnitude in segment-4 for T_L = 1.5Nm and f_C = 3000Hz.

$$P_{CuR} = N_R \left(\sum_{i=1}^{S_b} \rho_{Cu} J(i)^2 A_b(i) L_{bar} + 2R_{be}(f) \left(\frac{N_R I_{Rb}}{\pi p} \right)^2 \right) \tag{6.36}$$

where, $J(i) \Rightarrow$ rms value of current density, $A_b \Rightarrow$ area of i-th bar-segment, $L_{bar} \Rightarrow$ active bar length, $R_{be} \Rightarrow$ resistance of end-ring segment between the adjacent bars, $I_{Rb} \Rightarrow$ rms value of bar current, $\rho_{Cu} \Rightarrow$ copper-resistivity. The CL is determined using the measured values of the one cycle-averaged input power (P_{In}) and then, applying the input-output power balance as:

$$P_{Core} = P_{In} - P_{CuS} - P_{CuR} - P_{Out} \tag{6.37}$$

where,

$$P_{Out} = P_{Shaft} + P_{Windage} + P_{Bearing} \tag{6.38}$$

and,

$$P_{Shaft} = T_{Shaft} \omega_r \tag{6.39}$$

T_{Shaft} and ω_r are the measured values of shaft torque and rotor speed in rad/s respectively using torque sensor (Kistler 4503B) and CoMo Torque Type 4700 data acquisition system. Other equipments of the test-bench are: a) 2-level, H-bridge three-phase inverter b). 1.5 kW IM motor prototype c). Digital oscilloscope: YOKOGAWA DLM2054 with voltage and current

probes d). Voltage and current transducers: LEM sensors LV25-P and LA 15P f). dSPACE DS1103 for data acquisition f). Photo-tachometer. Fig.6.12 shows the experimental setup.

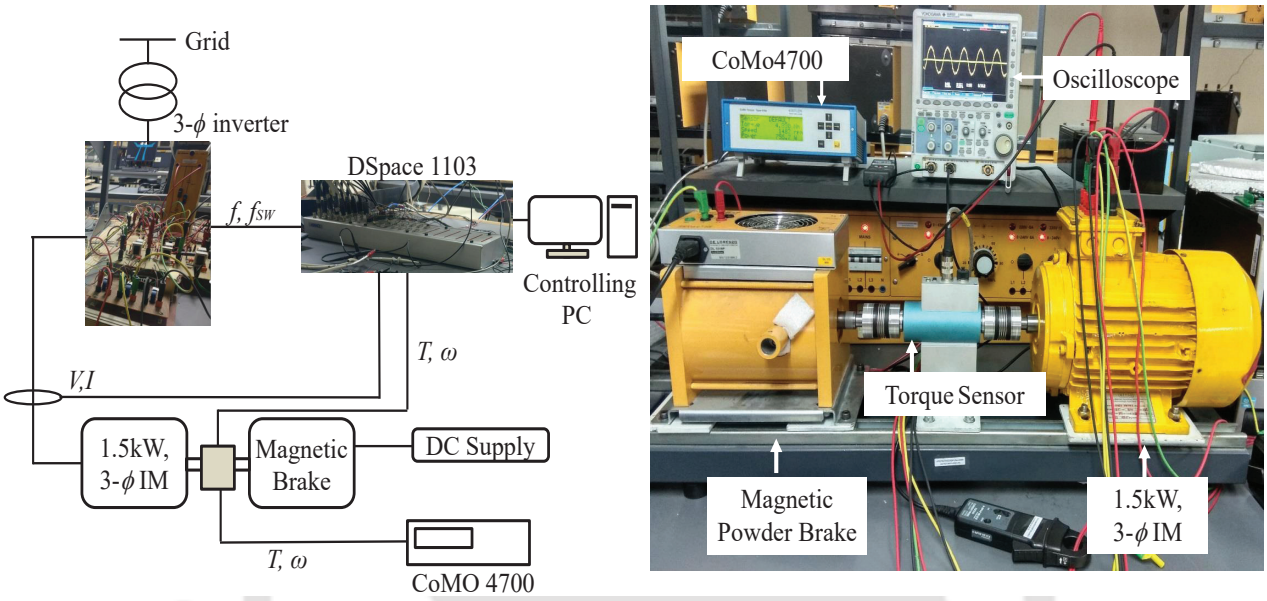

Fig. 6.12: Test-measurement setup: schematic and the physical test-bench

6.7.2 Results and discussions:

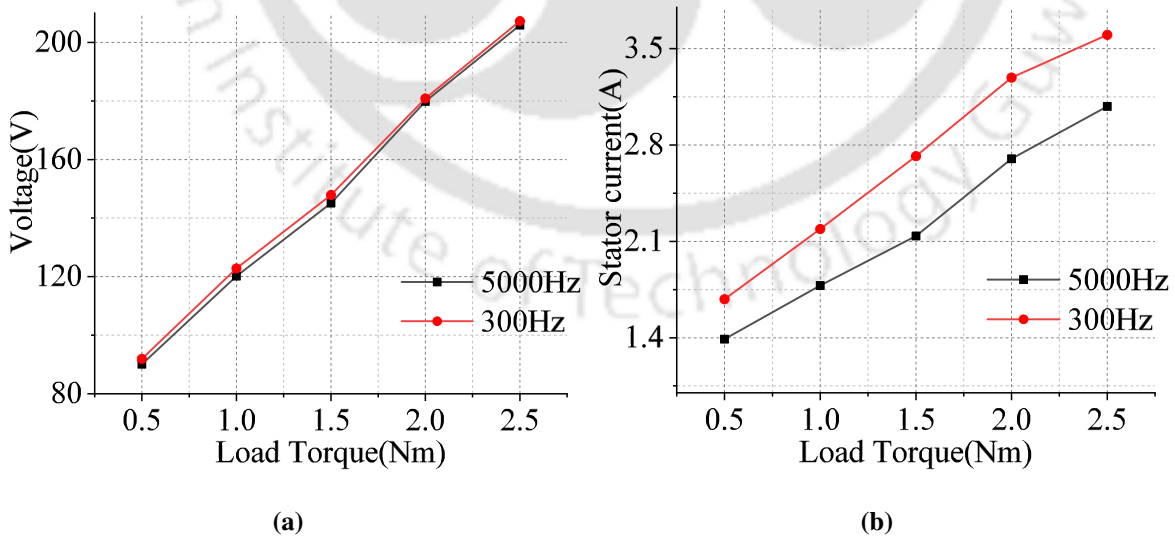

(a) **(b)**

Fig. 6.13: Profile of the motor's: (a) phase voltage and (b) stator current with change in shaft-torque

Following the proposed and other four widely used CL estimation methods described in the literature, the CL values for all the operating points (as given in 6.2) are determined. The four methods of the literature adopted for the comparison are:

Table 6.4: Error Estimates: With proposed and the existing CL methods

Parameter	M-1	M-2	M-3	M-4	Proposed
Max.Error(%)	55.91	37.98	33.24	10.67	13.61
Min. Error(%)	19.44	9.26	6.94	3.85	4.11
σ_{Errors}	10.05	8.11	7.24	2.11	2.35
f_{SW} at E(Max)	300Hz	300Hz	300Hz	300Hz	300Hz
f_{SW} at E(Min)	5Khz	5Khz	5Khz	5Khz	5Khz

- CL estimation as per (6.3) with taking the constant values of loss coefficients K_e and K_h: M-1 (K_e=3.717$W/Kg/Hz^2/T^2$, K_h=0.0449$W/Kg/Hz^{\alpha}/T^{\beta}$).
- CL estimation as per (6.3) with frequency and magnetisation dependant K_e (*i.e.*, $K_e(B_m, f_{eq})$) and constant K_h: M-2.
- CL estimation as per (6.3) with taking both the K_e and K_h, the functions of frequency and magnetisation (*i.e.*, with $K_e(B_m, f_{eq})$;$K_h(B_m, f_{eq})$): M-3.
- CL estimation with using the analytic expression of eddy current loss and, Jiles-Atherton model for the hysteresis loss: M-4.

Figs.6.9-6.10 show the measured and estimated CL values with all the techniques mentioned above. These results draw the following conclusions:

- The presented approach assuresCL estimation accuracy comparable to method M-4. With the proposed method, the values ofminimum and maximum errorsare 4.11% and 13.61%, respectively. These values, while adopting the methodM-4 for CL estimation, are3.85% and 10.67%, respectively. The proposed solution, on the other hand, is significantly more straightforward to execute than M-4.
- Both the suggested technique and M-4 demonstrate consistent error (*i.e.*, the smallest values of the standard deviation of errors (σ_{Errors})) for a given T_L. For instance, for T_L =2Nm, σ_{Errors} for the proposed method and M-4 are 2.35 and 2.11, respectively,indicating that the proposed approach's evaluation of hysteresis loop area is equivalent to that of the JA method. However, there is no direct method for accuratelymeasuring hysteresis loss (and thus HL area) alone.
- At low f_{sw}, method M-2 and M-3 manifesthigher inaccuracy because time harmonics are dominant and B-waveforms have more distortion than at high f_{sw}. At higher f_{sw}, where the current waveforms are close to a sinusoid, the error gets persistent. However, in compared to the proposed approach and M-4, the inaccuracieswith these methods arestill substantial.

- When the motor is lightly loaded where, the supply voltage is small (Fig.6.13). In this situation, the fraction of the magnetisation voltage ($e_{magnetisation} = v_{Supply} - i_S R_S - p' i_S L_{lS}$; $p' = d/dt$) to the input voltage is high. Hence, the no-load CL is higher than the on-load CL due to higher magnetisation voltage at no-load conditionsbecause saturation is not prudent at low voltage, and P_{CuR} and, stray losses are minor. The CL begins to increase as the load (along with the motor's terminal voltage) increases because of : a). local saturation as a result of increased leakage fluxes becomes effective and results in the rise ofcore loss [46]; b). with the higher value of slip, the joule losses of the rotorbecome considerable [31]; c). additional load-dependent losses (*i.e.*, stray load losses), which grow with torque, become significant [9, 80]. Because of a)-c), the CL during on-load is higher than the CL at no-load for the voltage profile shown in Fig.6.13 even $e_{magnetisation}$ in on-load condition remains smaller than the same of no-load condition.

6.8 Conclusion

For inverter-fed motors, a fast and accurate core loss computation approach is proposed in this chapter. The proposed method calculates eddy current loss by considering the fluctuation in material permeability over the period of time-varying magnetisation. In addition, the technique offers an approach for evaluating hysteresis losses that is relatively straightforward to implement. The developed methods accuracy is confirmed by comparing it to existing CL models. An inverter-fed IM is used to do this. The IM is operated for a wide range of switching frequency and load torque. For all of these operating points in this range, the CL of the motor is calculated using the proposed and four other widely used existing CL approaches. The proposed model is shown to have the lowest estimation error. The results of the proposed method are comparable to those of an analytically appended Jiles-Atherton method for hysteresis loss with a maximum and minimum error divergence of 2.94% and 0.26%, respectively.

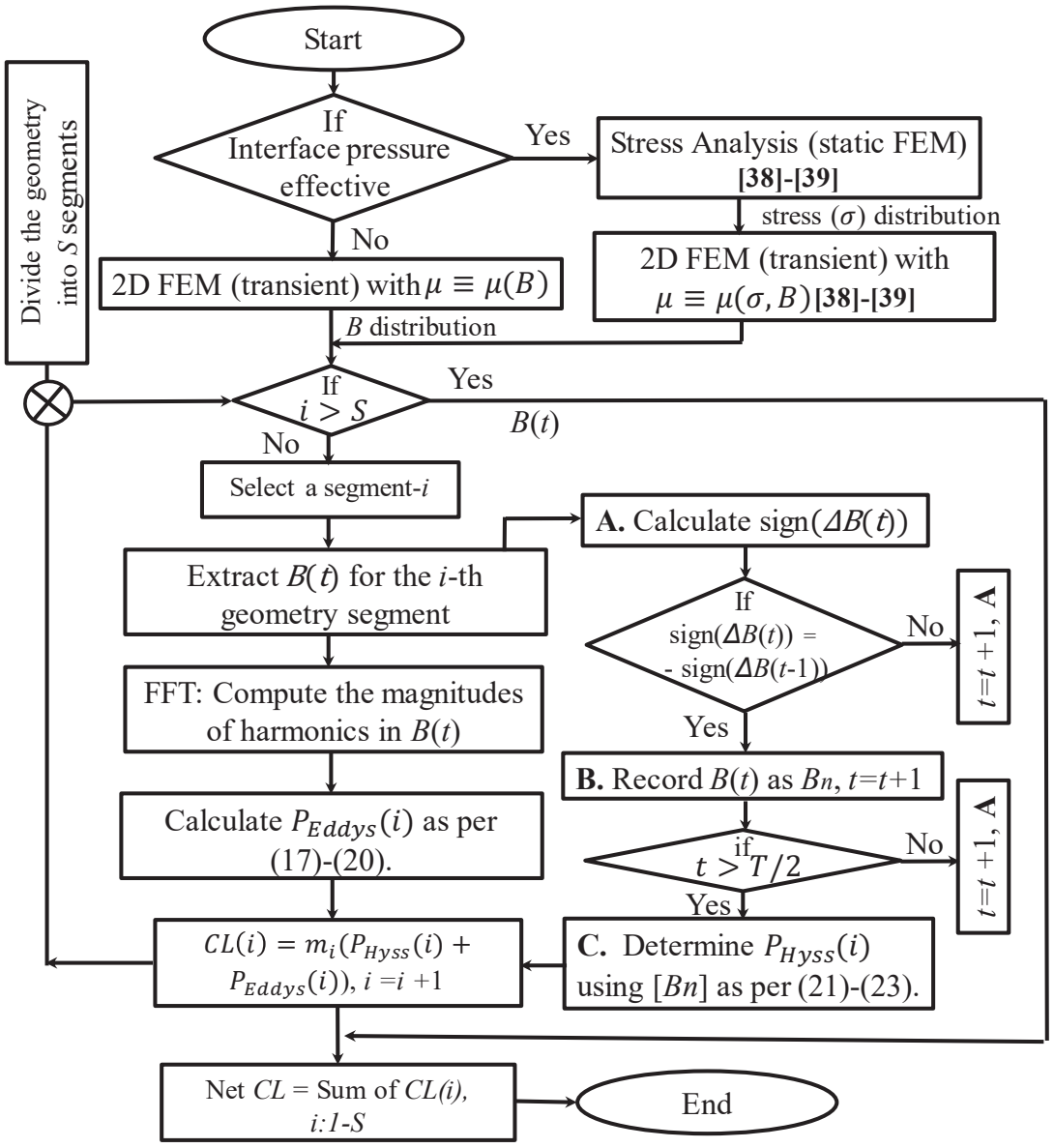

Fig. 6.8: CL estimation process as per the proposed method

7

Conclusions and Future Work

Contents

The thesis is focused on the formulation of the magnetic losses that occurred in a symmetrical three-phase induction motor. The summary of the work and its salient contributions are as described below:

7.1 Conclusions and summary of the work

Modeling of stray loss in an induction motor using the equivalent circuit parameters.

This work presents a model to evaluate the SL in a grid-connected IM. The model used motors' leakage and magnetizing inductances to determine SL. For its accuracy, the proposed model is compared with two such states of the art models proposed in the past and the SL allowance formulated in the prominent standards IEEE-112B and IEC-60034-2-1. The model is found to estimate SL more accurately for the given set of motors.

Design of induction motor for higher efficiency by reducing the stray loss.

In order to demonstrate the suitability of the stray loss model presented (in the previous work) in the design phase, four IMs of similar configuration were designed, prototyped, and tested. The design of the primary motor model then revamped for the reduction of stray loss following the design strategy postulated by the proposed model. SLs for these motor prototypes are calculated with the proposed model and the other models from the literature. The concludes model's capability of predicting the stray losses for motors with the same rating but different geometric configurations. This ascertains model's use in the design.

Impact of inverter power supply on stray loss and its formulation. // The work presents a fast and accurate empirical stray loss model for inverter fed three-phase induction motors (IMs). The model is intended to quantify the SL both at the design stage and, normal operation of the IM. The development of the model considers the variations of frequency, switching frequency and motor's loading. Test data of 128 operating points of two training IMs are used to develop the model. The accuracy and prediction capability of the proposed model is presented with the measured SL values for 128 operating points of another set of two IMs of the same specifications and different geometries.

Core loss estimation for an inverter-fed induction motor with more accurate realisa-

tion of material non-linearity and impact of hysteresis minor loops.

The work presents a fast and accurate core loss evaluation method for inverter-fed induction machines. The proposed method takes into account the influence of time variation of magnetic permeability on the eddy current loss. Furthermore, the proposed method presents an accurate approach to precisely evaluate the hysteresis loss. The results obtained from the proposed method are compared with the existing methods for a 1.5kW inverter-driven induction motor. The method shows sufficiently high accuracy with reduced complexity and implementation-time for a wide range of inverter switching frequency and motor's loading.

7.2 Scope for future work

This thesis describes the methods to accurately evaluate the magnetic losses of an induction machine. The work can further be extended for:

- Modeling of stray losses in other popular variants of the electric motor *i.e*, permanent magnet synchronous motor, synchronous reluctance motor.
- Development of the more accurate representation of stray loss by applying the conformal transformation to more complex shapes of the slots.
- Deployment of the proposed SL model in various motor control techniques and its further improvement.
- Evaluation of core losses with taking into account the magnetic field generated by the eddy current in addition to the proposed approach.
- Developing an inverse Jiles-Athorton model for the iso-parametric approach that can be used to include dynamic losses and to model asymmetric minor loops.

Bibliography

[1] "Annual report 2017," *IEA Technology Collaboration Programme on Energy Efficient End-Use Equipment (4E)*, 2017.

[2] C. U. B. Paul Waide, "Energy-efficiency policy opportunities for electric motor-driven systems," *Energy Efficiency Series by International Energy Agency*, no. 2, pp. 1–132, 2011.

[3] U. E. G. E. Facility, "Accelerating the global adoption of energy-efficient electric motors and motor systems," *U4E POLICY GUIDE SERIES*, 09 2017.

[4] J. G. D. Gilbert A. McCoy, "Premium efficiency motor selection and application guide:a handbook for industry," *U.S. Department of Energy (DOE) Office of Energy Efficiency and Renewable Energy (EERE)*, no. 2, pp. 25–90, 2014.

[5] "http://knowledgeplatform.in/wp-content/uploads/2016/11/iip-motors-ppt.pdf."

[6] A. T. De Almeida, F. J. T. E. Ferreira, and A. Q. Duarte, "Technical and economical considerations on super high-efficiency three-phase motors," *IEEE Trans. Ind. Appl.*, vol. 50, no. 2, pp. 1274–1285, March 2014.

[7] S. Mallik, K. Mallik, A. Barman, D. Maiti, S. K. Biswas, N. K. Deb, and S. Basu, "Efficiency and cost optimized design of an induction motor using genetic algorithm," *IEEE Trans. Ind. Electron.*, vol. 64, no. 12, pp. 9854–9863, Dec 2017.

[8] "Ieee standard test procedure for polyphase induction motors and generators," *IEEE Std 112-2004 (Revision of IEEE Std 112-1996)*, pp. 1–83, Nov 2004.

[9] "Rotating electrical machines - part 2-1:standard methods for determining losses and efficiency from tests (excluding machines for traction vehicles)," *IEC Std 60034-2-1*, Sep. 2007.

[10] "Rotating electrical machines - part 2-1:methods for determining losses and efficiency from tests of single-speed,three-phase,cage-induction mototrs," *JIS C 4034-2-1*, Sep. 2011.

[11] "Rotating electrical machines - part 2-1:methods for determining losses and efficiency from tests of single-speed,three-phase,cage-induction mototrs," *JEC 2110*, 2017.

[12] W. Cao, K. J. Bradley, J. C. Clare, and P. W. Wheeler, "Comparison of stray load and inverter-induced harmonic losses in induction motors using calorimetric and harmonic injection methods," *IEEE Trans. Ind. Appl.*, vol. 46, no. 1, pp. 249–255, Jan 2010.

[13] Y. Gao, T. Sanmaru, G. Urabe, H. Dozono, K. Muramatsu, K. Nagaki, Y. Kizaki, and T. Sakamoto, "Evaluation of stray load losses in cores and secondary conductors of induction motor using magnetic field analysis," *IEEE Trans. Magn.*, vol. 49, no. 5, pp. 1965–1968, May 2013.

[14] J. Cheaytani, A. Benabou, A. Tounzi, and M. Dessoude, "Stray load losses analysis of cage induction motor using 3-d finite-element method with external circuit coupling," *IEEE Trans. Magn.*, vol. 53, no. 6, pp. 1–4, June 2017.

[15] R. Roy, K. K. Prabhakar, and P. Kumar, "Core-loss calculation in different parts of induction motor," *IET Electric Power Appl.*, vol. 11, no. 9, pp. 1664–1674, 2017.

[16] K. Yamazaki, A. Suzuki, M. Ohto, T. Takakura, and S. Nakagawa, "Equivalent circuit modeling of induction motors considering stray load loss and harmonic torques using finite element method," *IEEE Trans. Magn.*, vol. 47, no. 5, pp. 986–989, May 2011.

[17] E. Levi, A. Lamine, and A. Cavagnino, "Impact of stray load losses on vector control accuracy in current-fed induction motor drives," *IEEE Trans. Energy Convers.*, vol. 21, no. 2, pp. 442–450, June 2006.

[18] A. Boglietti, A. Cavagnino, L. Ferraris, and M. Lazzari, "Induction motor equivalent circuit including the stray load losses in the machine power balance," *IEEE Trans. Energy Convers.*, vol. 23, no. 3, pp. 796–803, Sep. 2008.

[19] T. Kataoka, Y. Kandatsu, and T. Akasaka, "Measurement of equivalent circuit parameters of inverter fed induction motors," *IEEE Trans. Magn.*, vol. 23, no. 5, pp. 3014–3016, Sep. 1987.

[20] M. Basic and D. Vukadinovic, "Small size induction machine equivalent circuit including variable stray load and iron losses," *Journal of Electrical Engineering and Technology*, vol. 13, no. 2, pp. 1603–1612, 2018.

[21] M. Basic, D. Vukadinovic, and M. Polic, "Stray load and iron losses in small induction machines under variable operating frequency and flux: A simple estimation method," *IEEE Transactions on Energy Conversion*, vol. 33, no. 2, pp. 869–876, June 2018.

[22] P. Pillay, M. Al-Badri, P. Angers, and C. Desai, "A new stray-load loss formula for small and medium-sized induction motors," *IEEE Trans. Energy Convers.*, vol. 31, no. 3, pp. 1221–1227, Sep. 2016.

[23] E. B. Agamloh, "An evaluation of induction machine stray load loss from collated test results," *IEEE Transactions on Industry Applications*, vol. 46, no. 6, pp. 2311–2318, Nov 2010.

[24] Z. Gmyrek, A. Boglietti, and A. Cavagnino, "Estimation of iron losses in induction motors: Calculation method, results, and analysis," *IEEE Transactions on Industrial Electronics*, vol. 57, no. 1, pp. 161–171, 2010.

[25] H. Domeki, Y. Ishihara, C. Kaido, Y. Kawase, S. Kitamura, T. Shimomura, N. Takahashi, T. Yamada, and K. Yamazaki, "Investigation of benchmark model for estimating iron loss in rotating machine," *IEEE Transactions on Magnetics*, vol. 40, no. 2, pp. 794–797, 2004.

[26] C. P. Steinmetz, "On the law of hysteresis," *Proceedings of the IEEE*, vol. 72, no. 2, pp. 197–221, 1984.

[27] G. Bertotti, "General properties of power losses in soft ferromagnetic materials," *IEEE Transactions on Magnetics*, vol. 24, no. 1, pp. 621–630, 1988.

[28] D. M. Ionel, M. Popescu, S. J. Dellinger, T. J. E. Miller, R. J. Heideman, and M. I. McGilp, "On the variation with flux and frequency of the core loss coefficients in electrical machines," *IEEE Transactions on Industry Applications*, vol. 42, no. 3, pp. 658–667, 2006.

[29] D. M. Ionel, M. Popescu, M. I. McGilp, T. J. E. Miller, S. J. Dellinger, and R. J. Heideman, "Computation of core losses in electrical machines using improved models for laminated steel," *IEEE Transactions on Industry Applications*, vol. 43, no. 6, pp. 1554–1564, 2007.

[30] M. Popescu, D. M. Ionel, A. Boglietti, A. Cavagnino, C. Cossar, and M. I. McGilp, "A general model for estimating the laminated steel losses under pwm voltage supply," *IEEE Transactions on Industry Applications*, vol. 46, no. 4, pp. 1389–1396, 2010.

[31] Z. Haisen, Z. Dongdong, W. Yilong, Z. Yang, and X. Guorui, "Piecewise variable parameter loss model of laminated steel and its application in fine analysis of iron loss of inverter-fed induction motors," *IEEE Transactions on Industry Applications*, vol. 54, no. 1, pp. 832–840, 2018.

[32] W. Tong, S. Li, R. Sun, L. Sun, and R. Tang, "Modified core loss calculation for high-speed pmsms with amorphous metal stator cores," *IEEE Transactions on Energy Conversion*, pp. 1–1, 2020.

[33] W. Li, I. H. Kim, S. M. Jang, and C. S. Koh, "Hysteresis modeling for electrical steel sheets using improved vector jiles-atherton hysteresis model," *IEEE Transactions on Magnetics*, vol. 47, no. 10, pp. 3821–3824, 2011.

[34] K. Hoffmann, J. P. A. Bastos, J. V. Leite, N. Sadowski, and F. Barbosa, "A vector jiles-atherton model for improving the fem convergence," *IEEE Transactions on Magnetics*, vol. 53, no. 6, pp. 1–4, 2017.

[35] D. Zhang, T. Liu, H. Zhao, and T. Wu, "An analytical iron loss calculation model of inverter-fed induction motors considering supply and slot harmonics," *IEEE Transactions on Industrial Electronics*, vol. 66, no. 12, pp. 9194–9204, 2019.

[36] O. de la Barrire, C. Ragusa, C. Appino, and F. Fiorillo, "Prediction of energy losses in soft magnetic materials under arbitrary induction waveforms and dc bias," *IEEE Transactions on Industrial Electronics*, vol. 64, no. 3, pp. 2522–2529, 2017.

[37] V. Basso, G. Bertotti, O. Bottauscio, F. Fiorillo, M. Pasquale, M. Chiampi, and M. Repetto, "Power losses in magnetic laminations with hysteresis: Finite element modeling and experimental validation," *Journal of Applied Physics*, vol. 81, no. 8, pp. 5606–5608, 1997. [Online]. Available: https://doi.org/10.1063/1.364614

[38] A. Boglietti, A. Cavagnino, D. M. Ionel, M. Popescu, D. A. Staton, and S. Vaschetto, "A general model to predict the iron losses in pwm inverter-fed induction motors," *IEEE Transactions on Industry Applications*, vol. 46, no. 5, pp. 1882–1890, 2010.

[39] A. Boglietti, A. Cavagnino, and M. Lazzari, "Fast method for the iron loss prediction in inverter-fed induction motors," *IEEE Transactions on Industry Applications*, vol. 46, no. 2, pp. 806–811, 2010.

[40] H. Zhao, C. Ragusa, O. de la Barrire, M. Khan, C. Appino, and F. Fiorillo, "Magnetic loss versus frequency in non-oriented steel sheets and its prediction: Minor loops, pwm, and the limits of the analytical approach," *IEEE Transactions on Magnetics*, vol. 53, no. 11, pp. 1–4, 2017.

[41] H. Zhao, C. Ragusa, C. Appino, O. de la Barrire, Y. Wang, and F. Fiorillo, "Energy losses in soft magnetic materials under symmetric and asymmetric induction waveforms," *IEEE Transactions on Power Electronics*, vol. 34, no. 3, pp. 2655–2665, 2019.

[42] R. Liu and L. Li, "Analytical prediction model of energy losses in soft magnetic materials over broadband frequency range," *IEEE Transactions on Power Electronics*, vol. 36, no. 2, pp. 2009–2017, 2021.

[43] K. Yamazaki and N. Fukushima, "Torque and loss calculation of rotating machines considering laminated cores using post 1-d analysis," *IEEE Transactions on Magnetics*, vol. 47, no. 5, pp. 994–997, 2011.

[44] W. Guan, D. Zhang, Y. Zhu, Y. Gao, and K. Muramatsu, "Numerical modeling of iron loss considering laminated structure and excess loss," *IEEE Transactions on Magnetics*, vol. 54, no. 11, pp. 1–4, 2018.

[45] K. Yamazaki and Y. Sakamoto, "Electromagnetic field analysis considering reaction field caused by eddy currents and hysteresis phenomenon in laminated cores," *IEEE Transactions on Magnetics*, vol. 54, no. 3, pp. 1–4, 2018.

[46] I. Boldea and S. A. Nasar, "Induction machines design handbook," vol. 31, no. 3, 2010.

[47] I.Boldea and S. Nasar, *New York: Gordon and Beach*, 1970.

[48] A. E. Fitzgerald, C. K. Jr., and S. D. Umans, *Electrical Machinery*. Tata McGraw-Hill, 2010.

[49] B.Heller and V.Hamata, "Harmonic field effects in induction machines," 1977.

[50] S. A. N. Donald W. Novotny, "High frequency losses in induction motors," *NASA Lewis Research Center*, June 1991.

[51] J. Wang, M. Cheng, H. Wen, M. Tong, G. Zhang, Y. Hu, and B. Chen, "Stray load loss calculation for induction motor by combination of general airgap field modulation theory and 2d fea," *IEEE Transactions on Energy Conversion*, pp. 1–1, 2021.

[52] N. Glew, "Stray load losses in induction motors: a challenge to academia," *Power Engineering Journal*, vol. 12, no. 1, pp. 27–32, Feb 1998.

[53] K. P. Burnham and D. R. Anderson, "Multimodel inference: Understanding aic and bic in model selection," *Sociological Methods & Research*, vol. 33, no. 2, pp. 261–304, 2004. [Online]. Available: https://doi.org/10.1177/0049124104268644

[54] R. E. Kass and A. E. Raftery, "Bayes factors," *Journal of the American Statistical Association*, vol. 90, no. 430, pp. 773–795, 1995. [Online]. Available: https://amstat.tandfonline.com/doi/abs/10.1080/01621459.1995.10476572

[55] S. Rahman, "Energy, economics and environmental analysis for chillers in office buildings," *Energy Education Science and Technology Part a-Energy Science and Research*, vol. 25, pp. 1–16, 04 2010.

[56] M. Aoulkadi and A. Binder, "Comparison of different evaluation methods to determine stray load losses in induction machines with eh-star method," in *2007 IEEE Int. Electric Machines Drives Conf.*, vol. 1, May 2007, pp. 519–524.

[57] "Energy management guide for selection and use of fixed frequency medium ac squirrel-cage polyphase induction motors," *NEMA Standards Publication*, no. 10, 2001.

[58] A. Boglietti, A. Cavagnino, M. Cossale, A. Tenconi, and S. Vaschetto, "Efficiency determination of converter-fed induction motors: Waiting for the iec 60034-2-3 standard," in *2013 IEEE Energy Conversion Congress and Exposition*, 2013, pp. 230–237.

[59] A. Bonnett, "Analysis of the impact of pulse-width modulated inverter voltage waveforms on ac induction motors," *IEEE Transactions on Industry Applications*, vol. 32, no. 2, pp. 386–392, 1996.

[60] G. B. Reddy, G. Poddar, K. B. Nagrale, and B. P. Muni, "Synchronous pwm technique based on reference angle for induction motor traction drive application," in *2020 IEEE International Conference on Power Electronics, Drives and Energy Systems (PEDES)*, 2020, pp. 1–6.

[61] C.-Y. Huang, C.-P. Wei, J.-T. Yu, and Y.-J. Hu, "Torque and current control of induction motor drives for inverter switching frequency reduction," *IEEE Transactions on Industrial Electronics*, vol. 52, no. 5, pp. 1364–1371, 2005.

[62] M. Al-Badri, P. Pillay, and P. Angers, "Induction machine rapid performance test," *IEEE Transactions on Industry Applications*, vol. 55, no. 5, pp. 4685–4691, 2019.

[63] Q. Zhu, Q. Wu, W. Li, M.-T. Pham, and L. Zhu, "A general and accurate iron loss calculation method considering harmonics based on loss surface hysteresis model and finite-element method," *IEEE Transactions on Industry Applications*, vol. 57, no. 1, pp. 374–381, 2021.

[64] A. Boglietti, A. Cavagnino, M. Lazzari, and M. Pastorelli, "International standards for the induction motor efficiency evaluation: a critical analysis of the stray-load loss determination," *IEEE Transactions on Industry Applications*, vol. 40, no. 5, pp. 1294–1301, 2004.

[65] R. Kumar, P. Kumar, T. Kanekawa, and K. Oishi, "Stray loss model for induction motors with using equivalent circuit parameters," *IEEE Transactions on Energy Conversion*, vol. 35, no. 2, pp. 1036–1045, 2020.

[66] M. Ibrahim and P. Pillay, "Core loss prediction in electrical machine laminations considering skin effect and minor hysteresis loops," in *2012 IEEE Energy Conversion Congress and Exposition (ECCE)*, 2012, pp. 2681–2687.

[67] X. Zhao, R. Wang, X. Liu, and L. Li, "A dynamic hysteresis model for loss estimation of go silicon steel under dc-biased magnetization," *IEEE Transactions on Industry Applications*, vol. 57, no. 1, pp. 409–416, 2021.

[68] L. R. Dupré, R. V. Keer, and J. A. A. Melkebeek, "On a magnetodynamic model for the iron losses in non-oriented steel laminations," *Journal of Physics D: Applied Physics*, vol. 29, no. 3, pp. 855–861, mar 1996. [Online]. Available: https://doi.org/10.1088/0022-3727/29/3/052

[69] J. Szczyglowski and P. Jablonski, "Computation of core losses in electrical sheets used in electrical machines," *IET Electric Power Applications*, vol. 14, no. 2, pp. 291–296, 2020.

[70] A. M. Takbash and P. Pillay, "A modified analytical method for core losses calculation in magnetic laminations for a wide range of frequency and flux density," in *2015 IEEE International Electric Machines Drives Conference (IEMDC)*, 2015, pp. 1109–1114.

[71] G. Bertotti and I. D. Mayergoyz, in *The Science of Hysteresis:Mathematical Modeling and Applications*, 2006.

[72] S. Xue, J. Feng, S. Guo, Z. Chen, J. Peng, W. Q. Chu, L. R. Huang, and Z. Q. Zhu, "Iron loss model under dc bias flux density considering temperature influence," *IEEE Transactions on Magnetics*, vol. 53, no. 11, pp. 1–4, 2017.

[73] A. Cavagnino and A. Boglietti, "Iron loss prediction with pwm supply: An overview of proposed methods from an engineering application point of view," in *2007 IEEE Industry Applications Annual Meeting*, 2007, pp. 81–88.

[74] A. Balamurali, G. Feng, C. Lai, J. Tjong, and N. C. Kar, "Maximum efficiency control of pmsm drives considering system losses using gradient descent algorithm based on dc power measurement," *IEEE Transactions on Energy Conversion*, vol. 33, no. 4, pp. 2240–2249, 2018.

[75] D. Kowal, P. Sergeant, L. Dupr, and H. Karmaker, "Comparison of frequency and time-domain iron and magnet loss modeling including pwm harmonics in a pmsg for a wind energy application," *IEEE Transactions on Energy Conversion*, vol. 30, no. 2, pp. 476–486, 2015.

[76] B. Tekgun, Y. Sozer, I. Tsukerman, P. Upadhyay, and S. Englebretson, "Core loss estimation in electric machines with flux-controlled core loss tester," *IEEE Transactions on Industry Applications*, vol. 55, no. 2, pp. 1299–1308, 2019.

[77] J. Kitao, J. Aizawa, M. Nakano, M. Yamada, and A. Daikoku, "Development of variable stress applying system for shrink fitting of stator housing in ipm motor." in *2018 IEEE International Magnetics Conference (INTERMAG)*, 2018, pp. 1–1.

[78] K. Yamazaki and Y. Kato, "Iron loss analysis of interior permanent magnet synchronous motors by considering mechanical stress and deformation of stators and rotors," *IEEE Transactions on Magnetics*, vol. 50, no. 2, pp. 909–912, 2014.

[79] K. Yamazaki, Y. Sato, M. Domenjoud, and L. Daniel, "Iron loss analysis of permanent-magnet machines by considering hysteresis loops affected by multi-axial stress," *IEEE Transactions on Magnetics*, vol. 56, no. 1, pp. 1–4, 2020.

[80] R. Kumar, P. Kumar, T. Kanekawa, and K. Oishi, "Stray loss model for induction motors with using equivalent circuit parameters," *IEEE Transactions on Energy Conversion*, vol. 35, no. 2, pp. 1036–1045, 2020.